University of Camerino

PhD Course in Chemical and Pharmaceutical Sciences and Biotechnology Series XXXVII Cycle

Doctoral thesis

Sustainable Energy Storage and Conversion Materials for the Energy Transition

PhD Candidate
Balducci Leonardo

Thesis Supervisor
Nobili Francesco

Academic Year 2024/2025

UNIONE EUROPEA
Fondo Sociale Europeo
Ministero dell'Università e della Ricerca
PON RICERCA E INNOVAZIONE
REACT EU

Table of Contents

Abstract

Addressing the needs of billions of people while fighting climate change requires a fundamental shift in how we approach economic systems and sustainability. The current global challenges demand a rethinking of traditional business practices to prioritize sustainability and resilience. This transformation must be driven by an interdisciplinary approach that integrates socio-technical innovations, effective management strategies, and environmental responsibility across global value chains.

In the realm of energy storage and conversion, technologies such as lithium-ion batteries (LIBs), sodium-ion batteries (NIBs), supercapacitors (SCs) and Fuel Cells (FCs) play a critical role. As these technologies continue to penetrate the market, ensuring their sustainability becomes imperative. Sustainability in this context involves not only improving durability and performance but also minimizing the reliance on critical and scarce raw materials.

With a focus on the principles of the circular economy and the goal of achieving cost-effective and scalable processing, several innovative materials have been synthesized. These include a modified Mg- and Zr-doped LNMO cathode for lithium-ion batteries, a waste-valorized MOF-derived carbonaceous material for sodium-ion batteries and supercapacitors, and a series of doped Fe_2O_3 composites for oxygen reduction reaction (ORR) applications. Each material was developed using low-cost resources and/or synthetic methodologies, demonstrating their potential for sustainable and economical energy solutions.

All the materials were thoroughly investigated at both structural and electrochemical levels, showcasing their potential across various applications. The modified LNMO cathode for lithium-ion batteries demonstrated significant enhancements in stability, achieving outstanding capacity retention. At room temperature and 1C, the material retained 60.7% of its capacity after 1000 cycles, while at 50°C and 2C, it maintained 72.8% capacity retention over the same cycle count. The MOF-derived carbon exhibited exceptional performance as a supercapacitor, sustaining 36,000 cycles with 91% capacity retention and 99.7% coulombic efficiency, and also performed well in symmetric cell configurations. Beyond supercapacitors, the MOF-derived carbon excelled in sodium-ion batteries, delivering good rate performance and effective sodium-ion storage.

Additionally, the doped Fe_2O_3 nanoparticles grafted onto graphene oxide, with 6% magnesium and 6% nickel doping, showed superior peroxide scavenging properties during oxygen reduction reactions. When combined with FePc600 as supporting catalysts, the doped composites achieved a ring current density of 5.75 mA/cm² and reduced peroxide formation to 2.8%, outperforming pure FePc600, which exhibited a ring current density of 4.75 mA/cm² and peroxide

formation of 5.1%. These results highlight the impact of advanced material engineering in enhancing electrochemical performance across diverse energy storage and catalytic systems.

In the framework of the energy transition, a fuel cell test bench with unique features has been developed, designed to perform quality and performance tests on membrane electrode assemblies and fuel cell stacks. The research and development of this bench spanned several years, involving continuous problem identification and resolution. The project culminated in the completion of the test bench in October 2024, followed by its successful final installation.

Chapter 1. Introduction

1.1 The Beginnings: Batteries and Fuel Cells (1800-1900)

Inspired by Luigi Galvani's discovery in the late 18th century of "animal electricity" (which actually was not animal but only deriving by the metals holding the electrical contacts between frog legs), Alessandro Volta embarked on developing an electric storage system that would forever change the future. Volta's goal was to create a system in which electricity could be generated from non-living materials. In 1800, he succeeded with the invention of the first true battery, now known as the Voltaic Pile. This device consisted of alternating layers of zinc and copper separated by cloth soaked in saltwater. This breakthrough was a pivotal moment in science, laying the foundation for electrochemistry and inspiring future advancements[1].

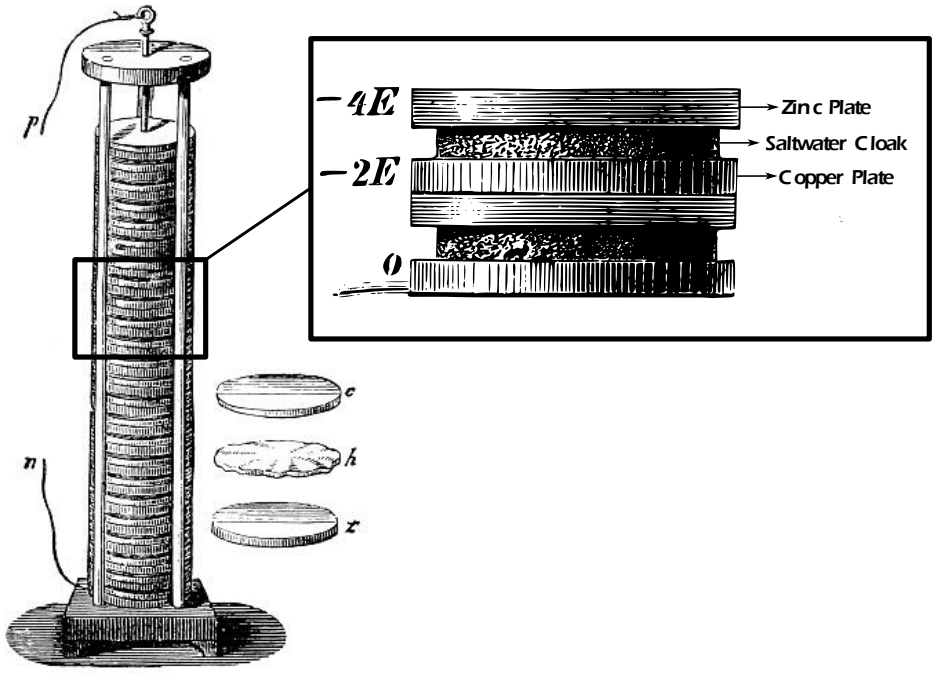

Fig 1.1 Voltaic Pile Illustration

In the early 19th century, new and improved versions of the Voltaic Pile emerged. Its working principle was based on the oxidation of Zn at the zinc plate surface (anode) that allowed the formations of Zn^{+2} ions and $2e^-$. when the zinc ions solvated by the electrolyte 2 H^+ at the copper surface (cathode) accepted the $2e^-$ to be reduced to H_2, as described in the following equations.

1) $$Zn \rightarrow Zn^{2+} + 2e^-$$

2) $$2H^+ + 2e^- \rightarrow H_2$$

In 1802, William Cruikshank developed the Trough Battery, a more practical model consisting of a series of cells connected to increase operating voltage. In 1836, John Daniell introduced the Daniell Cell, an enhanced design that incorporated copper and zinc sulfates and sulfuric acid to address the corrosion issues in Volta's original battery, creating the first practical, applied battery.

Forty-two years after Volta's discovery and inspired by prior studies on water decomposition via electricity by Christian Friedrich Schönbein in 1838, Sir William Grove constructed the first prototype of a fuel cell, which he named the Gas Voltaic Pile[2]. This rudimentary model, made with platinum and/or zinc electrodes immersed in sulfuric acid and bubbled alternatively with hydrogen and oxygen, was based on the hydrogen oxidation reaction at the anode and the oxygen reduction reaction at the cathode, as descirbed by the following equations:

3) $$2H^{+} + 2e^{-} \rightarrow H_2$$

4) $$\frac{1}{2}O_2 + 2H^{+} + 2e^{-} \rightarrow H_2O$$

However, this device had limited practical application due to its low efficiency and high cost.

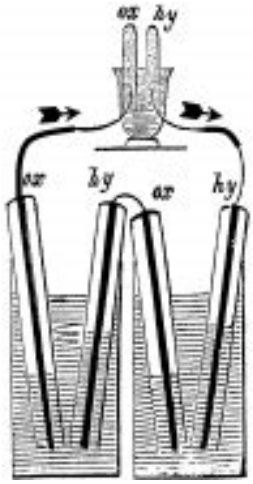

Fig 1.2 Gas Voltaic Pile Illustration

In 1859, Gaston Planté made a groundbreaking advancement with the invention of the lead-acid battery, the first rechargeable battery, constructed from lead and lead dioxide submerged in sulfuric acid. This new battery demonstrated greater reliability, durability, and versatility, making it suitable for a broad range of applications.

1.2 The Progress: The foundation of modern Batteries and Fuel Cells and the rise of Supercapacitors (1900-2000)

In 1901, Thomas Edison sought to improve upon the lead-acid battery by enhancing its lifespan and mechanical resilience[3]. Driven by this ambition, he developed the nickel-iron battery, a rechargeable battery widely used in industrial applications[4]. While Edison's battery was highly durable, it saw limited use outside of industrial settings due to its low energy output.

Around the same period, the carbon-zinc dry battery emerged, a "dry" cell that would later be further enhanced by Lewis Urry in the 1950s into the first alkaline battery, known for its notably longer lifespan and more efficient disposal[5].

As battery technology advanced, interest in fuel cells remained limited, primarily due to lower efficiency. This changed with groundbreaking contributions from German chemist Friedrich Wilhelm Ostwald, who in the early 20th century laid the theoretical groundwork for ionic conduction and catalytic mechanisms. Curiosity and research in fuel cells surged in the 1960s when NASA adopted alkaline fuel cells as the primary power source for its Gemini and Apollo missions. Soon afterward, General Electric pushed toward new development areas discovering the first prototype of the Proton Exchange Membrane (PEM) Fuel Cell and a rudimental first prototype of electrostatic double layer supercapacitors, setting the foundation for what would become two of the most promising electrochemical research fields[6].

The 1970s marked a pivotal era for electrochemical energy storage as environmental concerns and the oil crisis highlighted the need for clean energy sources. These pressures accelerated research into electrochemical devices, leading to efforts to create more sustainable batteries and fuel cells.

Building on over two decades of lithium research, the first commercial lithium-ion battery was introduced in 1991 by Sony and Asahi Kasei Corporation, which consisted in a $LiCoO_2$ cathode and a Graphite anode immersed in an electrolyte composed by Lithium Hexafluorophosphate and organic carbonate as solvent[7]. In contrast to earlier batteries, lithium-ion technology offered high energy density, low weight, and reliable rechargeability, representing a significant leap forward in modern battery technology.

1.3 The development of Batteries, Fuel Cells, Supercapacitors and the nowadays situation (2000-Present Day)

Since 2000, the world energy consumption increased dizzyingly, the overall energy consumption passed from 122686 TWh to 186230 TWh in 2023, with a steady increase between 1 to 2% each year, with the exception of financial crisis of 2009 and the covid-19 pandemic in 2021.

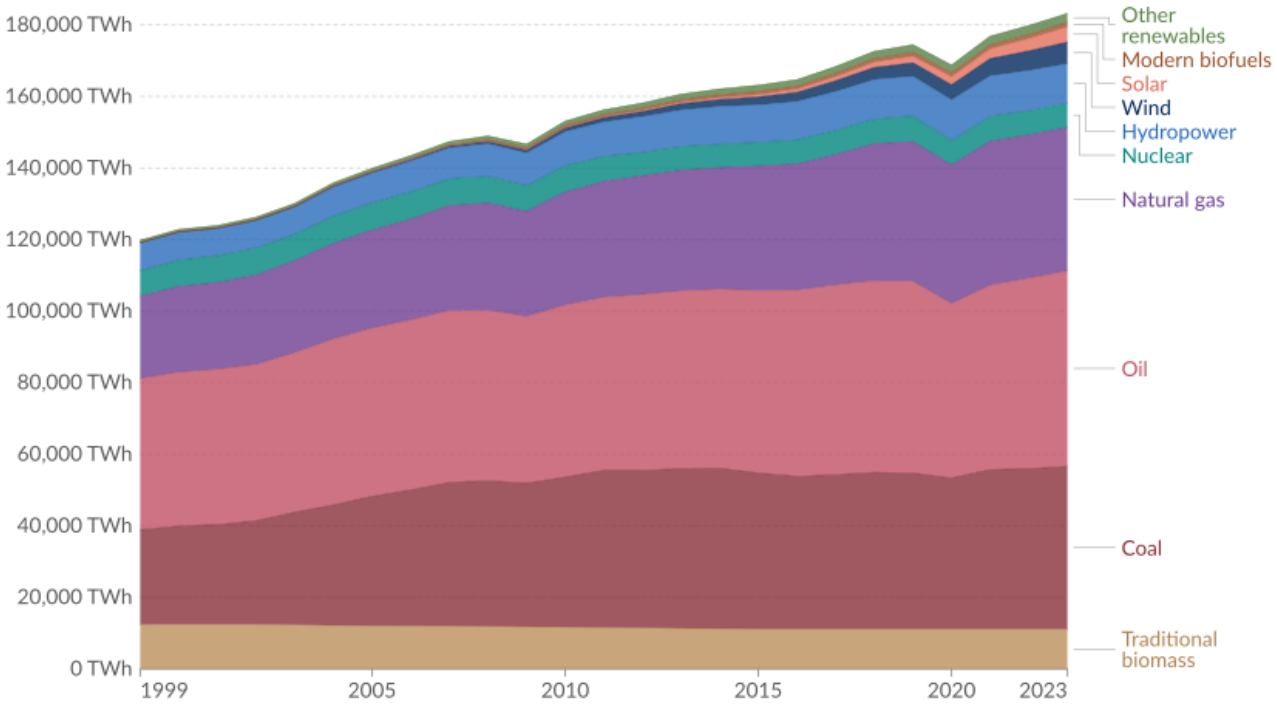

Fig. 1.3 World energy consumption chart

Of the 186,230 TWh of global energy produced, only a small portion currently comes from renewable sources. The energy mix is broken down as follows: Traditional Biomass (6.06%), Coal (24.87%), Oil (29.78%), Natural Gas (21.89%), Nuclear (3.72%), Hydropower (6.01%), Wind (3.30%), Solar (2.33%), Modern Biofuels (0.72%), and Other Renewables (1.33%).

The climate crisis has intensified the urgency to transition from a fossil fuel-dependent energy system to one based on renewable sources. This transition has spurred a surge in demand for electrochemical storage and production technologies capable of delivering high power output at a competitive cost, supporting the shift to a cleaner and more sustainable energy infrastructure.

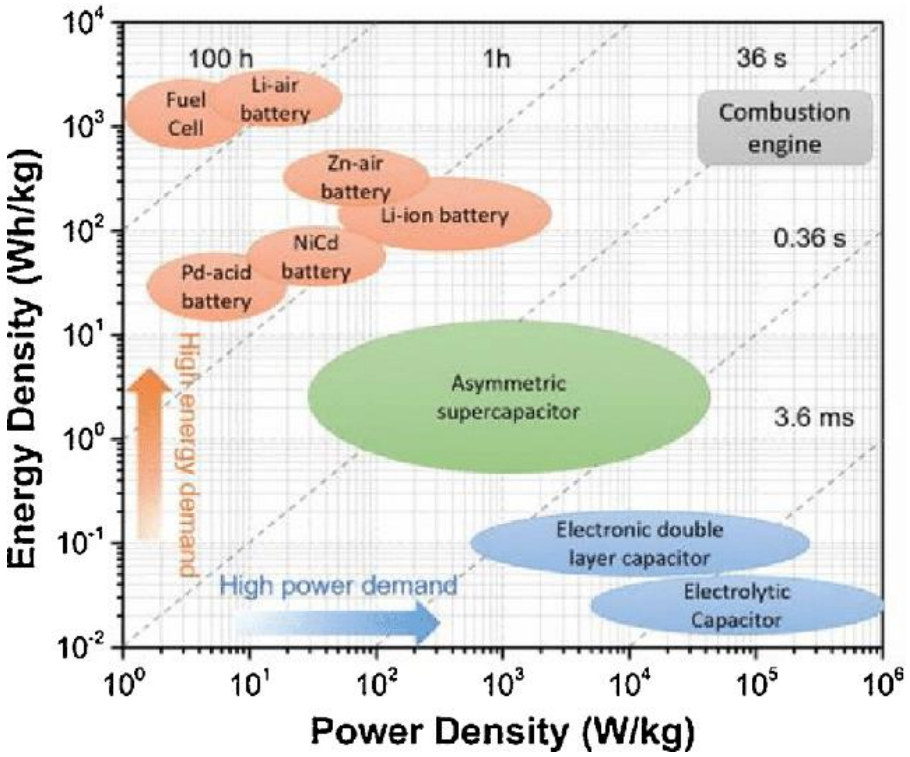

Fig. 1.4 Ragone plot for different electrochemical production and storage devices[8]

Sustainability in electrochemical production and storage devices is a rapidly growing area of research, driven by the increasing global demand for cleaner energy sources and more efficient storage solutions. Electrochemical technologies, such as batteries, supercapacitors, and fuel cells, are at the forefront of sustainable energy systems due to their capacity to store and release energy efficiently. However, to make these devices truly sustainable, it is essential to optimize their entire lifecycle—from raw material extraction to end-of-life disposal or recycling[8]. Key materials, such as lithium, cobalt, and nickel, which are used in lithium-ion batteries, have a substantial environmental footprint, given the energy-intensive processes required for their extraction and the often-limited availability of these resources. As such, researchers are exploring alternative materials, like sodium or magnesium, which are more abundant and environmentally friendly, but still capable of providing the high energy densities needed for applications in electric vehicles and renewable energy storage. Additionally, designing devices with higher recyclability and minimal toxic waste is critical to reducing their environmental impact. Closed-loop recycling systems, in which battery materials are efficiently recovered and reused, help mitigate the depletion of raw resources and lessen the ecological footprint associated with mining. Moreover, advancements in green manufacturing practices, such as using less energy-intensive electrode synthesis methods and eco-friendly electrolytes, further contribute to the sustainability of these devices. By improving the durability, recyclability, and energy efficiency of electrochemical storage systems, we can significantly reduce their environmental impact while fostering a more sustainable energy future.

The electrochemical devices should exhibit either a high energy density, that is the energy stored in each mass or volume, or a high power density, that is the rate of energy transfer in a given mass or volume, or both, as sketched in the Ragone plot (Fig. 1.4)

1.2 Li-Ion Batteries

Lithium-ion (Li-Ion) batteries are rechargeable batteries foundational to everyday electronic devices, electric vehicles (EVs), and various industrial applications, owing to their high power and energy density. LIBs offer additional benefits, including a wide operating temperature range, absence of memory effect, minimal maintenance requirements, high coulombic efficiency, rapid charging capability, and high-rate power discharge. However, Li-ion batteries present still challenges such as capacity fading, high cost, health concern and potential safety risks when overcharged or damaged[9–11].

Today, most cathode materials rely on critical metals that raise sustainability, abundance, and health concerns, with cobalt (Co) standing out as one of the most problematic. A large portion of the world's cobalt supply is mined in the Democratic Republic of Congo (DRC), home to the largest cobalt and copper reserves globally. The sustainability issues associated with cobalt mining are significant, including soil, water, and air pollution, along with the production of toxic waste. Furthermore, cobalt mining in the DRC is fraught with ethical challenges, such as corruption, unsafe working conditions, and pervasive child labour[12–15].

Therefore, developing cobalt-free cathode materials has become a primary focus in current research, with an emphasis on maintaining high capacity and long cycle life.

The generical LIBs system present 2 electrodes (cathode and anode) separated by an electrolyte-soaked separator.

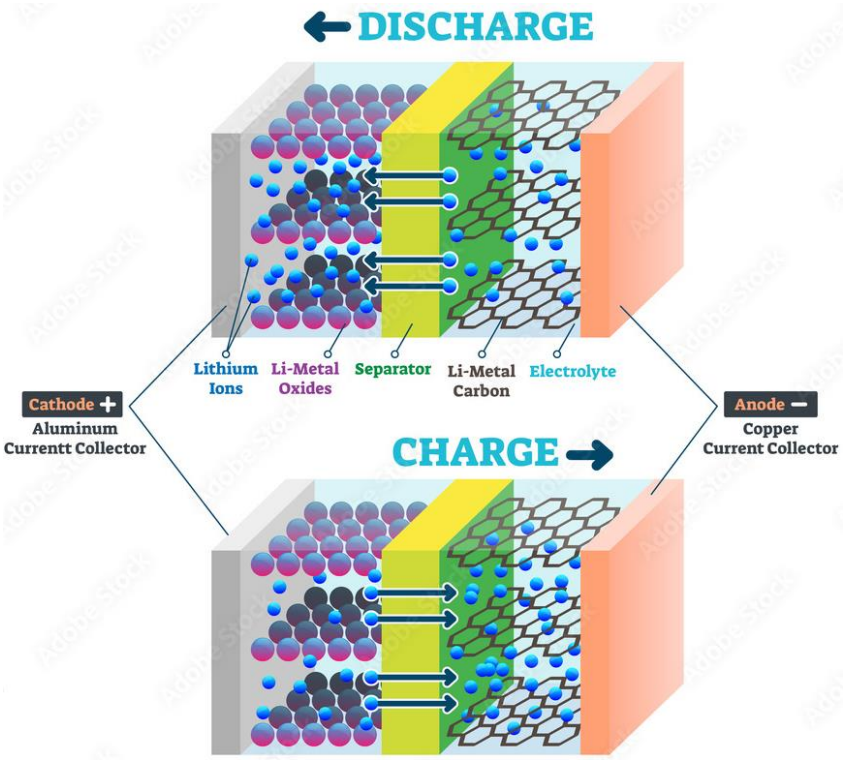

Fig. 1.5 Battery illustration during charge and discharge

The overall electrochemical reaction in a battery during charging involves the oxidation of the cathode through delithiation and the reduction of the anode through lithiation[9,11]. During discharge, this process reverses: the anode undergoes oxidation, while the cathode undergoes reduction. These reactions can be expressed by the following equations:

5) $$LiMO_y \rightarrow Li_{1-x}MO_y + xLi^+ + xe^-$$

6) $$C + xLi^+ + xe^- \rightarrow Li_xC$$

Where the the equations 1) and 2) occurs during charge and M is a one or more transition metals, while during discharge the equation 3) and 4) occurs:

7) $$Li_xC \rightarrow C + xLi^+ + xe^-$$

8) $$Li_{1-x}MO_y + xLi^+ + xe^- \rightarrow LiMO_y$$

The method by which lithium is stored, extracted, and inserted in a battery depends heavily on the structure of the cathode material itself[15].

2.1 Cathode materials in LIBs

Today, major research has been focused on the creation of higher and prolonged performances cathodes. Cathode materials are categorized into three primary structural families:

olivine, layered, and spinel. Olivine cathodes are known for their high safety, stability, and cost-effectiveness, featuring a 1D channel structure that facilitates lithium-ion (Li^+) insertion and extraction[16]. Among olivine-based compounds, Lithium Iron Phosphate ($LiFePO_4$), commonly referred to as LFP, is the most extensively developed and researched. LFP structure contributes to its stability and resilience, making it a widely favoured choice for applications where safety and longevity are prioritized[14].

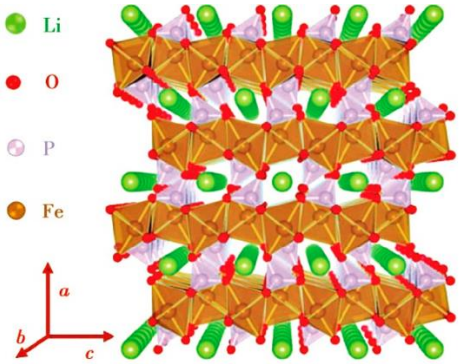

Fig. 1.6 LFP structure

However, when talking about disadvantage olivine cathode material presents a low operating voltage and thus a low energy output. The layered cathode materials are second class of cathodes. They are regarded as the most widely commercialized and applicated cathode materials due to the long-life span, low self-discharge, ease preparation and high theoretical volumetric capacity.[17] Despite these advantages, layered cathodes present a major problem related to the availability of lithium since the extraction of more than half the total lithium present in the structure causes the structure collapse. The standard layered cathode are $LiCoO_2$ (LCO), $LiNi_{1/3}Mn_{1/3}Co_{1/3}O_2$ (NMC) and $LiNi_{0.8}Co_{0.15}Al_{0.05}O_2$ (NCA)[12,13].

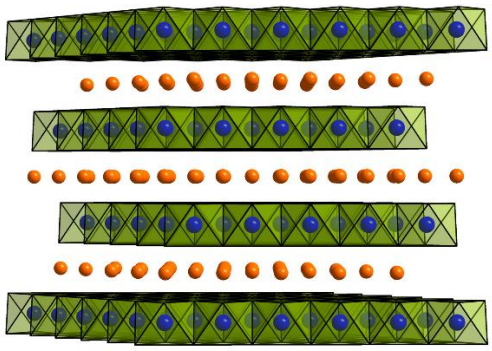

Fig. 1.7 Layered structure

Spinel cathode materials are considered among the highest-performing cathodes due to their high operating voltage, largely attributed to the Ni redox couple, which enables significant

energy output. However, this advantage is counterbalanced by pronounced capacity fading, which, along with electrolyte degradation at high voltages, limits their widespread commercialization. The electrolyte faces stability challenges at elevated voltages due to a slightly narrower electrochemical stability window. Among spinel cathodes, Lithium Nickel Manganese Oxide ($LiNi_{0.5}Mn_{1.5}O_4$) is one of the most promising options not only for the high-power output but also for being Cobalt-free, since its global supply is attracting increasing concern both in economical and ethical way.

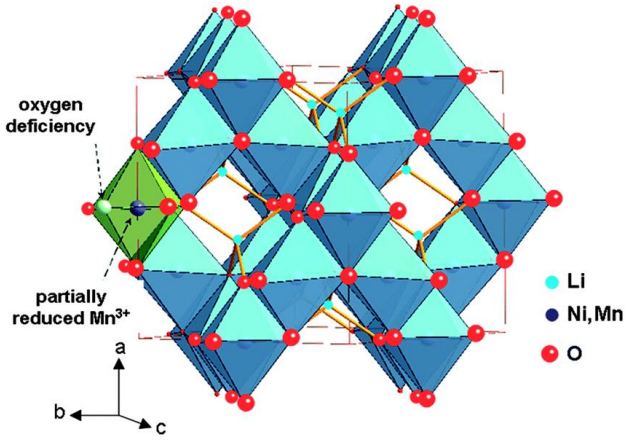

Fig. 1.8 Structure of LNMO disordered and ordered

The following table lists the most common pristine cathode materials which have been previously discussed:

Table 1.1: Comparison of cathode materials for lithium-ion batteries

Acronym	Formula	Structure	Potential vs Li^+/ Li (V)	Specific Capacity (mAh/g)	Specific Energy (Wh/Kg)
LFP	$LiFePO_4$	Olivine	3.45	150-170	518-587
LCO	$LiCoO_2$	Layered	3.9	140	546
NMC	$LiNi_yMn_zCo_{1-y-z}O_2$	Layered	3.8	160-170	610-650
NCA	$LiNi_yCo_zAl_{1-y-z}O_2$	Layered	3.8	180-200	680-760
LNO	$LiNiO_2$	Layered	4.0	160	640
LMO	$LiMnO_2$	Spinel	4.1	100-120	410-492
LNMO	$LiNi_{0.5}Mn_{1.5}O_4$	Spinel	4.7-4.9	147	624

1.2.2 Anode Materials in LIB

The first commercially available LIBs produced by Sony used an anode of graphite, a carbonaceous material with high crystallinity composed by carbon atoms arranged in planes (graphene) stacked by intermolecular forces to create a multi-layer stacked material.

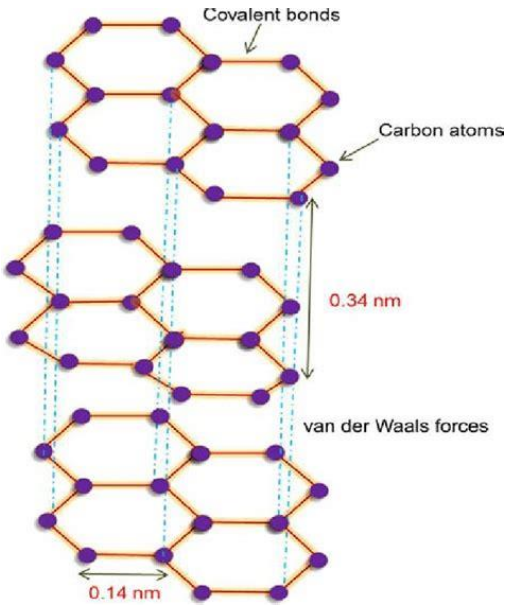

Fig. 1.9 Graphite structures

Graphite materials are capable to store lithium through intercalation between graphene layers, several studies tried to develop a theory about graphite intercalation[18]. Intercalation can be performed by 2 main mechanisms: Rüdorff model in which the intercalant fills all the possible space of a graphene-graphene intercalation site until each of them are full and the Daemus-Hérold model where each intercalant fills the intercalation site with the lower energy of activation and repulsion, as explained by the following figure:

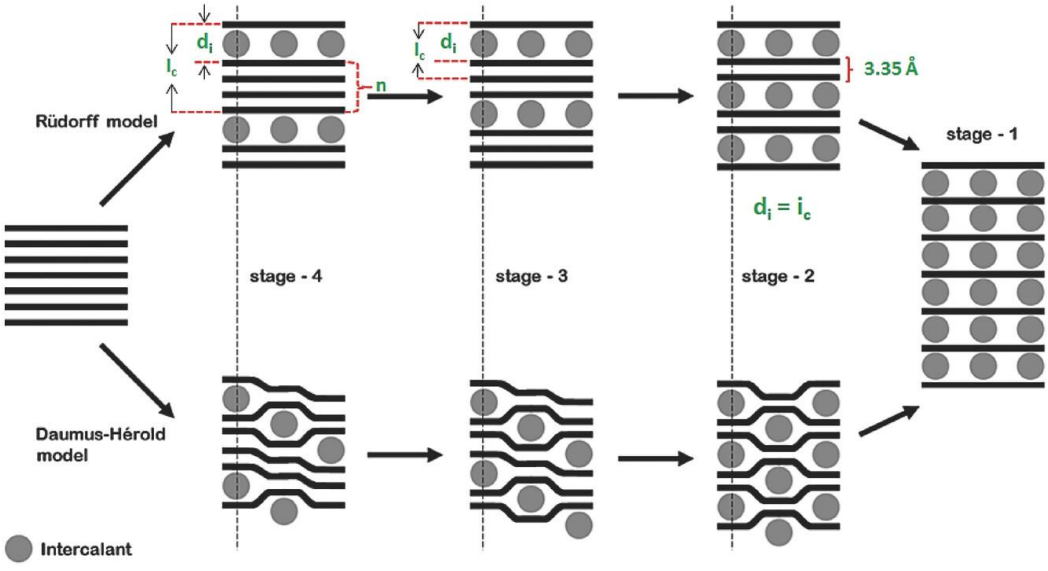

Fig. 1.10 Intercalation models in graphite materials

Today, graphite is no longer the sole anode material used in lithium-ion batteries (LIBs). Anode materials are broadly categorized into three main groups: alloying materials, conversion materials, and intercalation/absorption materials. Alloying materials, as their name suggests, form alloys with lithium during cycling[19]. These materials provide exceptional capacity, making them

ideal for high-power applications[20].

However, they face significant challenges, particularly capacity fading caused by volume expansion, which leads to electrode cracking and reduced longevity. Current research is focusing on strategies to address these issues, such as surface coatings and defect engineering, to mitigate expansion and improve electrode durability. Among alloying materials, silicon (Si) and tin (Sn) are considered the most promising for industrial applications due to their high potential and ongoing advancements in their development[21].

The second class of anode materials is conversion materials. These materials store lithium through conversion reactions, where a metal oxide (or sulfides, nitrides, etc.) reacts with lithium to form reduced metal nanoparticles embedded in a Li_2O matrix. This process can be summarized by the following equation:

10) $$MO_x + 2xLi^+ + 2xe^- \rightarrow M + xLi_2O$$

Conversion materials offer higher theoretical capacities compared to traditional graphite anodes and are attractive for high-energy applications. However, challenges such as poor reversibility, structural degradation, and sluggish kinetics hinder their practical implementation. Ongoing research is focused on improving these aspects through nanostructuring, compositional optimization, and advanced electrode design[18].

The final class of anode materials includes intercalation/absorption materials, where the previously introduced graphite is categorized[18]. In addition to graphite there are other 2 class of materials that are included in this category: soft carbon, and hard carbon. These materials can be broadly classified based on their degree of structural ordering and the rearrangements that occur during thermal treatment. Each type exhibits distinct properties and advantages, which will be explored in detail in the following paragraphs.

Table 1.2: Comparison of anode materials for lithium-ion batteries

Material	Group	Voltage vs Li/Li+ (V)	Specific Capacity (mAh/g)	Specific Power (Wh/Kg)
Si	Alloying	0.2	3760	752
Sn	Alloying	0.6-0.1	993	297
Fe_2O_3	Conversion	1.0-1.5	1000	225-500
Co_3O_4	Conversion	1.3-1.5	890	300-600
Graphite	Intercalation	0.01-0.2	370	100-300

1.3 Na-ion Batteries

In recent decades, concerns have risen regarding the continuous usage and industrial applications of lithium-ion batteries (LIBs), likely due to the intensive lithium extraction processes that require substantial water usage. Additionally, major lithium deposits are often located in politically unstable regions, leading to high price volatility in the lithium market. This uncertainty drives researchers to explore alternative charge carriers, with sodium emerging as a promising candidate. As the next alkali metal after lithium, sodium is abundant and inexpensive, making it an attractive substitute. However, substantial challenges remain before sodium-ion batteries (NIBs) can match LIB performance, particularly in developing compatible anode and cathode materials. When we take in consideration the anode, the graphite commonly used in LIBs is unsuitable for NIBs, as the larger ionic radius of sodium prevents efficient intercalation into graphite's interplanar spaces, in addition the larger Na^+ ion remarkable change in the volumetric capacity. Consequently, developing a stable, efficient, and cost-effective anode is crucial for the large-scale commercialization of NIBs[22].

1.3.1 Insertion-adsorption materials for NIBs anodes

Among carbon-based materials, disordered carbons have shown substantial promise as anode materials for sodium-ion batteries (NIBs) due to their high specific capacities and large surface areas. Disordered carbon structures consist of sp^2-hybridized carbon atoms arranged in a 2D hexagonal lattice, held together by van der Waals forces. Disordered carbons are generally classified as either soft or hard carbon, with their primary differences lying in the degree of structural disorder. Soft carbon, which has a lower level of disorder, can be graphitized at temperatures above 1000°C. In contrast, hard carbon is highly disordered and resists graphitization, ultimately transforming into glassy carbon only after heat treatment at 3000°C[18,22].

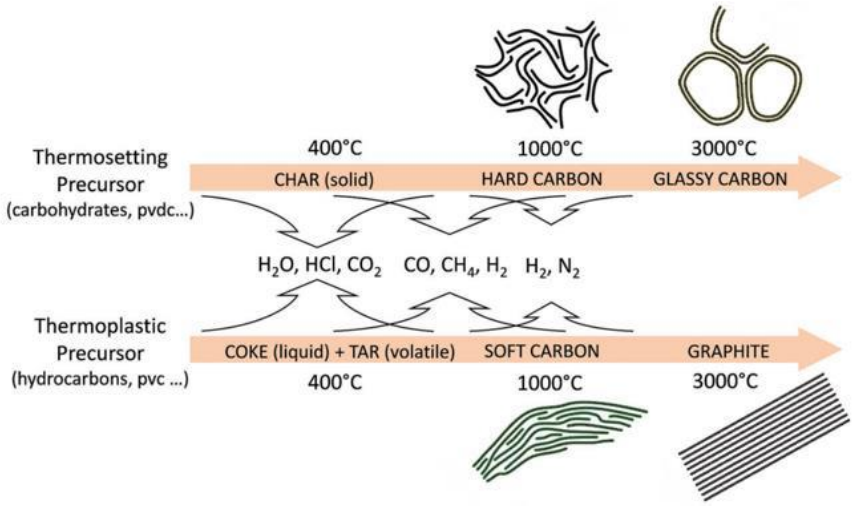

Fig. 1.11 Carbonaceous material type and thermal driven transformations

Additionally, soft carbons exhibit a sloping voltage profile without the distinct low-voltage plateau typical of hard carbons. Although the storage mechanisms in these materials are still under investigation, the prevailing hypothesis suggests that they store sodium through a combination of insertion and adsorption and pore filling processes[17].

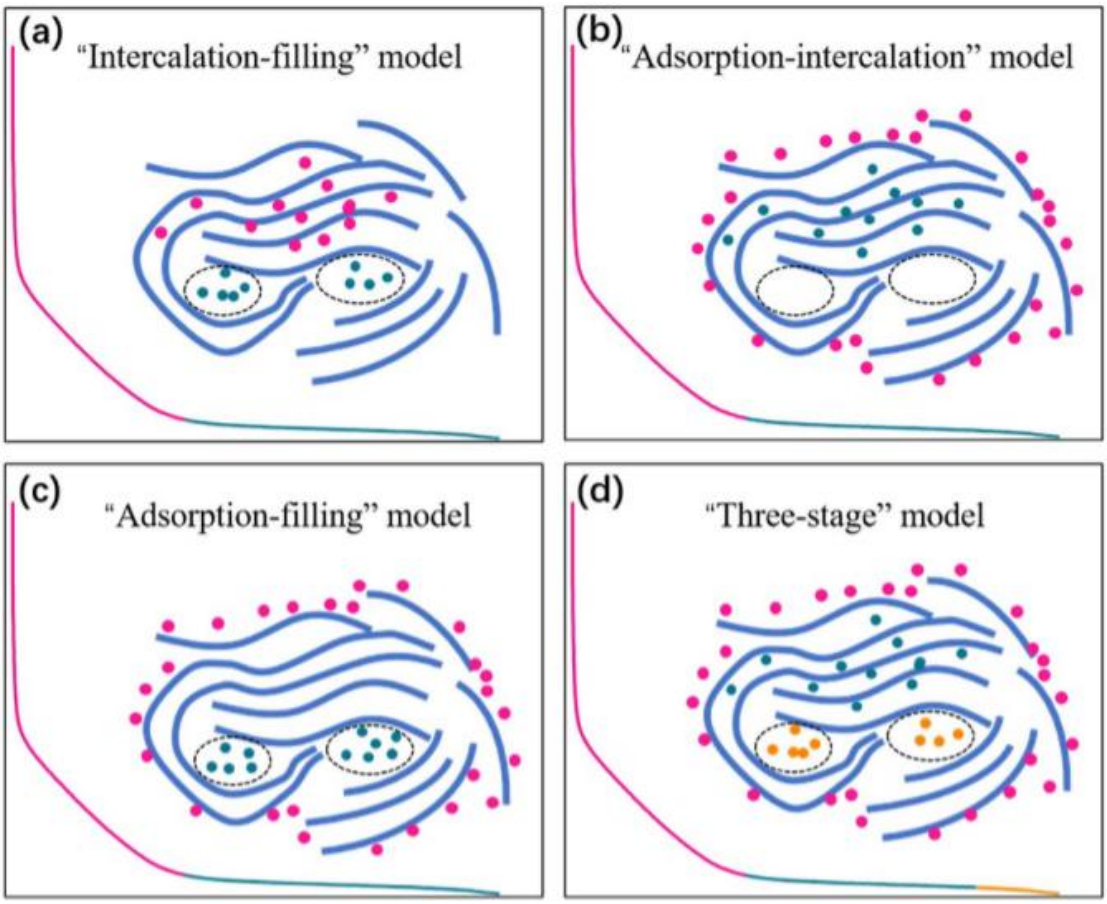

Fig. 1.12 Voltage profile difference for each kind of carbon

1.4 Electrostatic Double Layer Capacitors

As expressed previously in the subchapter 1.1 General Electric was the first company to propose the concept of Electrostatic Double Layer Capacitors (EDLCs). Nowadays, the field of Supercapacitors is divided into 3 main categories depending on the charge storage mechanisms, namely EDLCs, Pseudo-Capacitors (PCs) and Hybrid Capacitors (HCs)[23–25].

EDLCs

In EDLCs electrical energy is stored by ion absorption without Faradaic charge transfer, resulting in high power density, fast cycling processes and higher long-term performances.

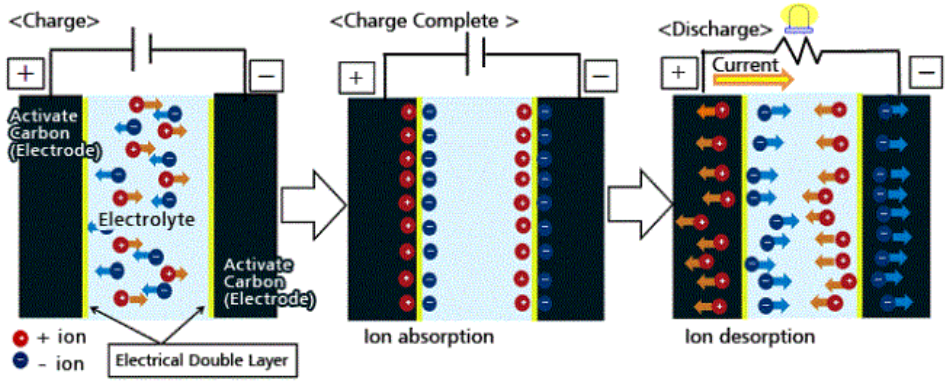

Fig. 1.13 EDLCs working principles

Fig. 1.13 EDLCs working principles

By expressing the electrodes surface as Es1 and Es2 (electrode/electrolyte interface as //) and anion and cation as A- and C+, respectively. The electrochemical equation related to the cycling processes can be expressed as follow:

Charging:

$$E_{s1} + A^- \longrightarrow E_{s1}^+//A^- + e^-$$

$$E_{s2} + C^+ + e^- \longrightarrow E_{s2}^-//C^+$$

Discharge:

$$E_{s1}^+// A^- + e^- \longrightarrow E_{s1}^+ + A^-$$

$$E_{s2}^-//C^+ \longrightarrow E_{s2} + C^+ + e^-$$

An example of EDLC's are carbonaceous materials with high surface area higher than 500/600 m^2/g.

Pseudo-Capacitors

In pseudo-capacitors, charge is stored through faradaic reactions occurring at the interface between the electrode and the electrolyte. Unlike typical batteries and electrochemical double-layer capacitors (EDLCs), pseudo capacitors utilize electrode materials capable of rapid charge transfer

during redox reactions, such as manganese dioxide (MnO_2) and ruthenium dioxide (RuO_2). This fast charge transfer allows for high power density and quick charge/discharge cycles, setting pseudo-capacitors apart from other energy storage devices[24,25].

Hybrid Capacitors

Hybrid capacitors combine the characteristics of electrochemical double-layer capacitors (EDLCs) and pseudo-capacitors (PCs) by using one electrode of each type. In these devices, one electrode operates through faradaic reactions (typical of pseudo-capacitors) while the other stores energy through electrostatic charge separation (characteristic of EDLCs). This combination enables hybrid capacitors to achieve a balance between high energy density, typical of pseudo-capacitors, and high-power density, typical of EDLCs[24,25].

Table 1.3 Comparison of different supercapacitors0

Comparison parameters	EDLC	Pseudo-capacitors	Hybrid capacitors
Electrode Materials	Carbon	Metal Oxide (MnO_2, RuO_2…)	A combination of EDLCs and PCs
Charge Storage Mechanisms	Electrochemical double layer (non-faradaic reactions)	Redox reactions	Both
Electrical Proprieties	Low E_d Good Rate Capability Good Cyclic Stability Low C_p	High C_p High E_d High P_d Low Rate Capability	High E_d High P_d Good Cycle Stability

1.5 Fuel Cells

Since NASA's renewed interest in fuel cells as the primary power source for Apollo missions, the field of fuel cell technology has seen consistent growth, reaching new peaks in recent years. Fuel cells are now recognized as one of the most promising energy solutions for long-range transportation applications such as trains, trucks, and airplanes. They are categorized based on their operating temperature and the state of the electrolyte, which determines their power output and specific range of applications[26,27].

Fuel cells are generally divided into two main temperature categories:

1. Low-Temperature Fuel Cells: This category includes Proton Exchange Membrane Fuel Cells (PEMFCs), Direct Methanol Fuel Cells (DMFCs), and Alkaline Fuel Cells (AFCs), each of which operates at relatively low temperatures.

2. High-Temperature Fuel Cells: This group includes Phosphoric Acid Fuel Cells (PAFCs), Molten Carbonate Fuel Cells (MCFCs), and Solid Oxide Fuel Cells (SOFCs), which operate at

higher temperatures.

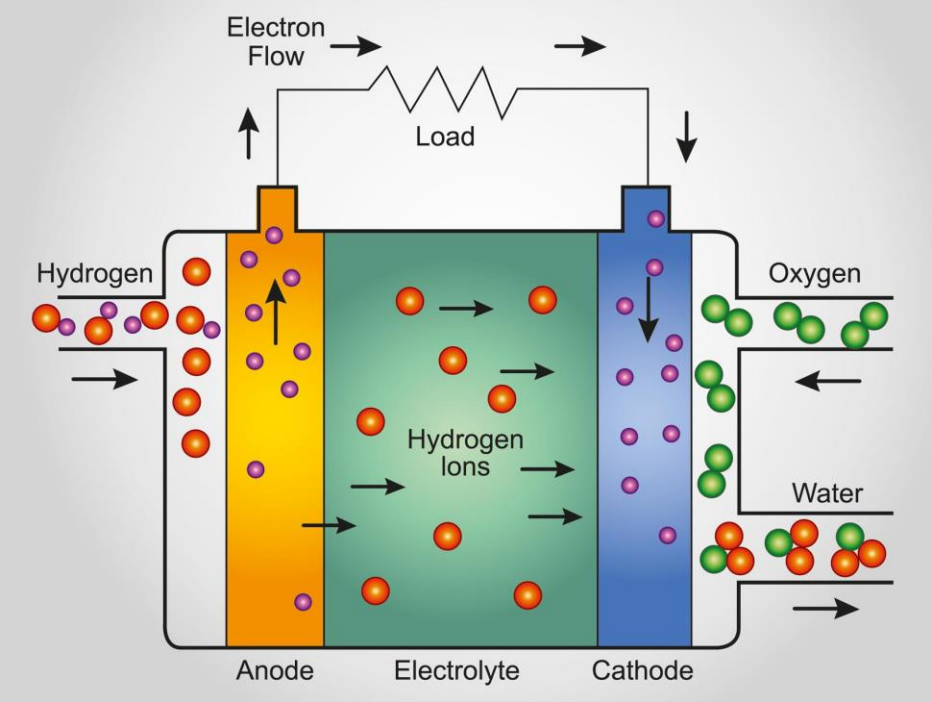

Fig. 1.14 PEMFCs schematic diagram

Each type of fuel cell offers distinct advantages in terms of power output and application, making fuel cell technology adaptable to a range of energy needs across various industries.

In detail, the operating temperature is reported in the following table:

Table 1.4 Fuel cell operating temperatures

Fuel Cells	Operating Temperature (°C)
PEMFCs	70-100
DMFCs	20-90
AFCs	50-150
PAFCs	200
MCFCs	650
SOFCs	500-1000

1.5.1 Catalyst Materials

The working mechanisms change depending on the kind of the fuel cell; however, it can be generically expressed as:

$$2\ H_2(g) + O_2(g) \rightarrow 2H_2O(l) + \text{Energy}$$

Among these, low-temperature fuel cells have gained increased attention for their potential in everyday transportation applications. Despite some current limitations, Proton Exchange Membrane Fuel Cells (PEMFCs) and Alkaline Fuel Cells (AFCs) stand out as particularly

promising energy production devices, thanks to their moderate operating temperatures and efficient energy output.

The reaction pathways in low-temperature fuel cells (FCs) primarily follow two mechanisms based on the electron transfer number: the favourable 4- electron pathway and the less desirable 2+2 electron pathway. The 4-electron process directly reduces oxygen to water, ensuring efficient energy conversion and minimal byproduct formation. In contrast, the 2+2 electron pathway involves the partial reduction of oxygen, resulting in the formation of hydrogen peroxide (H_2O_2) as an intermediate. This peroxide species is highly reactive and can severely damage the membrane by radical reactions, compromising the durability and performance of the fuel cell.

The overall oxygen reduction reaction (ORR) mechanism in fuel cells depends significantly on the electrolyte's pH, leading to different intermediate steps in acidic and alkaline environments. The mechanisms are expressed as follows:

$4e^-$ Pathway

$$O_2 + 4H^+ + 4e^- \rightleftharpoons 2H_2O$$

$2e^- + 2e^-$ Pathway

$$O_2 + 2H^+ + 2e^- \rightleftharpoons H_2O_2$$

$$H_2O_2 + 2H^+ + 2e^- \rightleftharpoons 2\,H_2O$$

→ Acidic pH

$4e^-$ Pathway

$$O_2 + H_2O + 4e^- \rightleftharpoons 4\,HO^-$$

$2e^- + 2e^-$ Pathway

$$O_2 + {}^* + H_2O + 2e^- \rightleftharpoons HOO^{-\,*} + HO^-$$

$$HOO^- + H_2O + 2e^- \rightleftharpoons 3\,HO^-$$

→ Alkaline pH

The standard catalyst material is Pt/C which is composed by a dispersion of Pt nanoparticles supported on highly surface area Carbon material. Much of today's research is focused on developing more efficient, cost-effective catalysts to replace platinum, the long-standing high-performance standard.

Scientists are increasingly exploring Platinum Group Metal-Free (PGM-free) catalysts, with iron-nitrogen-carbon (FeNC) compounds emerging as highly promising alternatives. FeNC's structure comprises single iron atoms embedded within a carbon matrix and coordinated by four nitrogen atoms bonded directly to the iron. This configuration can deliver high performance,

occasionally rivaling the traditional Pt/C benchmark. However, FeNC faces challenges in stability, including capacity degradation due to iron leaching in acidic environments, combined with relatively high synthesis costs that limit its commercial viability. This points to the need for new, more affordable materials that can be synthesized rapidly and economically. Iron oxide, for instance, is a promising candidate due to its simple, fast, and low-cost synthesis, potentially paving the way for wider industrial applications. Despite this, these materials are not deeply investigated due to their lower catalytic activity compared to FeNC and their lower pathway selection between 4e- and 2+2e[27–29].

1.5.2 Fuel Cells: An engineering problem?

The commercialization of fuel cells (FCs) is significantly more complex than that of battery technologies due to the lack of infrastructure and production standardization for FC systems. Starting from a much lower Technology Readiness Level (TRL), the fuel cell field faces numerous engineering challenges compared to the battery field. While the push for hydrogen technologies has gained traction only in recent years, battery technologies have long been integrated into daily life. Moreover, fuel cells require meticulous control of multiple parameters, such as gas humidification, flow rates, and temperature regulation. These challenges are further compounded by the intricate design and optimization of fuel cell components, including flow-field geometries and membrane electrode assembly (MEA) formulations[29–31].

At the microscopic scale, extensive research has been conducted on catalysts, membranes, and catalyst layer formulations. The standard catalyst, Pt/C, has been rigorously studied to optimize various factors, including platinum loading, Pt-to-Nafion ratios, Pt-to-carbon ratios, and dispersion quality. Additionally, parameters such as isopropanol-to-water ratios, ink preparation methods (e.g., stirring and sonication times and frequencies), significantly influence the final MEA performance. Despite these efforts, the high cost and limited availability of platinum have driven research into alternative catalysts. Among these, iron-based catalysts have emerged as a promising low-cost substitute, demonstrating the potential to achieve performance comparable to Pt/C.

At the macroscopic scale, industries are focused on optimizing flow-field shapes and bipolar plate designs. Parameters such as gas channel flow density and direction, channel dimensions and shapes, and the material composition of bipolar plates play a crucial role in determining fuel cell performance. These designs impact internal gas turbulence, gas adsorption on catalyst surfaces, and the protection and conduction properties of the MEA, highlighting the interplay between microscopic and macroscopic considerations in advancing fuel cell technologies[29–31].

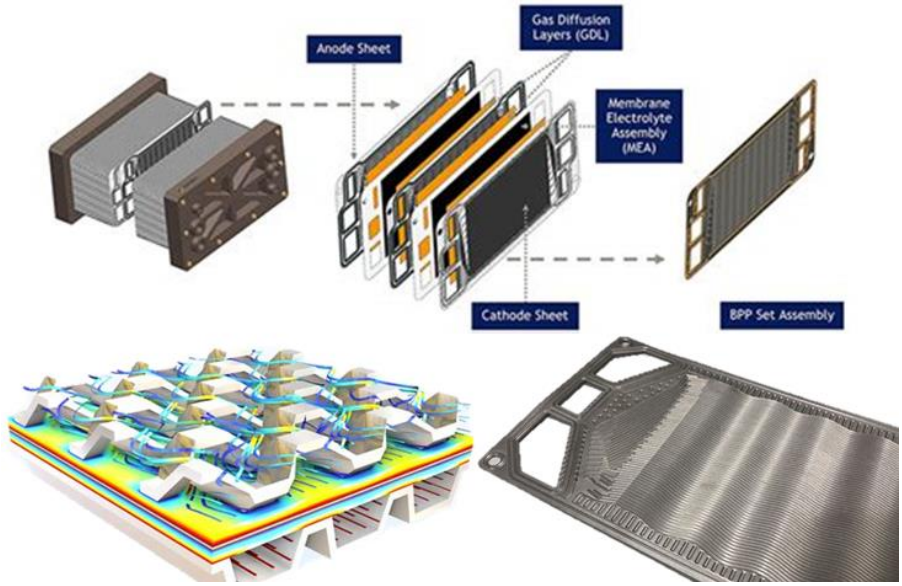

Fig. 1.15 Fuel Cell component design

Further zooming out, when a practical application is taken into consideration, many parameters play a synergistic role to deploy the best performance. In this regards gas flow, humidification type, humidification line dimension and type, operating temperature, temperature insulation and cooling, stack design, wastewater management system and hydrogen storage. Due to the number of parameters and the sluggish kinetics with the respect of oxygen reduction reaction of the cathode, the application of Fuel Cell for daily transportation are still far from the practical application. Despite this, their potential lies in the possible application as long-range transportations such as trains, trucks and planes.

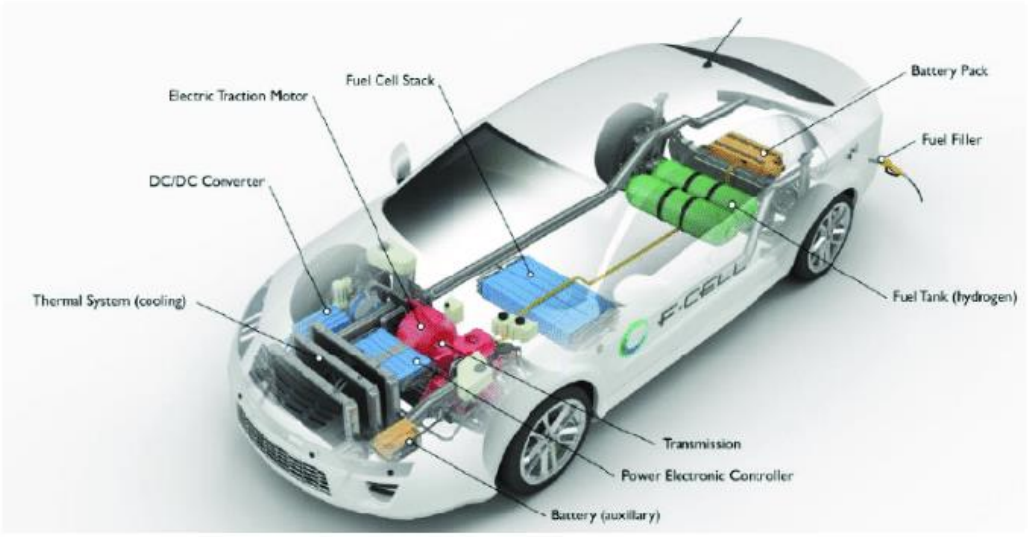

Fig. 1.17 A fuel cell powered car scheme

Nowadays, several examples of fuel cell-powered transportation are being developed, with two of the most prominent examples being the Toyota Mirai and hydrogen-powered trains. These

advancements highlight the potential of hydrogen as a clean and sustainable energy vector for the energy transition. Hydrogen offers a promising solution for storing energy, which can later be utilized in fuel cells to generate electricity with minimal environmental impact[26,29–31].

However, the widespread adoption of hydrogen faces significant challenges. One of the primary obstacles is the lack of infrastructure for hydrogen refueling and transportation. Additionally, the absence of standardized quality assessment instruments for industrial-scale MEA production further hinders its integration into the energy market. Addressing these issues will be crucial for accelerating the adoption of hydrogen technologies and realizing their full potential in decarbonizing the transport sector and beyond.

References

1. Sudduth, W. The Voltaic pile and the electrochemical theory. *AMBIX* vol. 27 (1980).
2. Clarke, T. B., Glasscott, M. W. & Dick, J. E. The Role of Oxygen in the Voltaic Pile. *J Chem Educ* **98**, 2927–2936 (2021).
3. Kurzweil, P. Gaston Planté and his invention of the lead-acid battery-The genesis of the first practical rechargeable battery. *J Power Sources* **195**, 4424–4434 (2010).
4. Ieee, . *2011 IEEE 33rd International Telecommunications Energy Conference*. (IEEE, 2011).
5. *Encyclopedia of Applied Electrochemistry*. *Encyclopedia of Applied Electrochemistry* (Springer New York, 2014). doi:10.1007/978-1-4419-6996-5.
6. Burke, K. A. *Small Portable PEM Fuel Cell Systems for NASA Exploration Missions https://ntrs.nasa.gov/citations/20060008648*.
7. Ramadass, P., Haran, B., White, R. & Popov, B. N. *Performance Study of Commercial LiCoO 2 and Spinel-Based Li-Ion Cells*. **DOI** 10.1149/1.1634273
8. Schlemmer, W., Selinger, J., Hobisch, M. A. & Spirk, S. Polysaccharides for sustainable energy storage – A review. *Carbohydr Polym* **265**, (2021).
9. 35035045.
10. Scrosati, B., Hassoun, J. & Sun, Y. K. Lithium-ion batteries. A look into the future. *Energy and Environmental Science* vol. 4 3287–3295 Preprint at https://doi.org/10.1039/c1ee01388b (2011).
11. Van Schalkwijk, W. & Scrosati, B. *Advances in Lithium Ion Batteries Introduction*. Springer New York, NY, https://doi.org/10.1007/b113788
12. Li, L. *et al.* Recent Progress on Layered Cathode Materials for Nonaqueous Rechargeable Magnesium Batteries. *Small* vol. 17 Preprint at https://doi.org/10.1002/smll.201902767 (2021).

13. Xu, B., Qian, D., Wang, Z. & Meng, Y. S. Recent progress in cathode materials research for advanced lithium ion batteries. *Materials Science and Engineering R: Reports* vol. 73 51–65 Preprint at https://doi.org/10.1016/j.mser.2012.05.003 (2012).
14. Zaghib, K. *et al.* Review and analysis of nanostructured olivine-based lithium recheargeable batteries: Status and trends. *Journal of Power Sources* vol. 232 357–369 Preprint at https://doi.org/10.1016/j.jpowsour.2012.12.095 (2013).
15. Fergus, J. W. Recent developments in cathode materials for lithium ion batteries. *Journal of Power Sources* vol. 195 939–954 Preprint at https://doi.org/10.1016/j.jpowsour.2009.08.089 (2010).
16. Nytén, A., Abouimrane, A., Armand, M., Gustafsson, T. & Thomas, J. O. Electrochemical performance of Li2FeSiO4 as a new Li-battery cathode material. *Electrochem commun* **7**, 156–160 (2005).
17. PbSO, P., Koh, N., -, -e, Li Si, V. & LiX, S. *PbO 2 H 2 O H 2 SO 4 /H 2 O H + PbSO 4 SO 4 2-+-e-2.0 V Lead-Acid Li 1-x CoO 2 LiPF 6 EC-DMC LiPF 6 EC-DMC Lithium Ion Future Batteries? Lithium Ion Based on Nanomaterials Ionic Liquids Lithium Metal Lithium-Air Lithium-Based Electrolytes*. (1859).
18. Nzereogu, P. U., Omah, A. D., Ezema, F. I., Iwuoha, E. I. & Nwanya, A. C. Anode materials for lithium-ion batteries: A review. *Applied Surface Science Advances* vol. 9 Preprint at https://doi.org/10.1016/j.apsadv.2022.100233 (2022).
19. Zhang, W. J. A review of the electrochemical performance of alloy anodes for lithium-ion batteries. *Journal of Power Sources* vol. 196 13–24 https://doi.org/10.1016/j.jpowsour.2010.07.020 (2011).
20. ReviewonCarbonandSiliconBasedMaterialsasAnodeMaterials.
21. Hueso, K. B., Armand, M. & Rojo, T. High temperature sodium batteries: Status, challenges and future trends. *Energy and Environmental Science* vol. 6 734–749 Preprint at https://doi.org/10.1039/c3ee24086j (2013).
22. Perveen, T. *et al.* Prospects in anode materials for sodium ion batteries - A review. *Renewable and Sustainable Energy Reviews* vol. 119 Preprint at https://doi.org/10.1016/j.rser.2019.109549 (2020).
23. Iro, Z. S., Subramani, C. & Dash, S. S. A brief review on electrode materials for supercapacitor. *International Journal of Electrochemical Science* vol. 11 10628–10643 Preprint at https://doi.org/10.20964/2016.12.50 (2016).
24. Iro, Z. S., Subramani, C. & Dash, S. S. A brief review on electrode materials for supercapacitor. *International Journal of Electrochemical Science* vol. 11 10628–10643 Preprint at https://doi.org/10.20964/2016.12.50 (2016).
25. Zhang, L., Hu, X., Wang, Z., Sun, F. & Dorrell, D. G. A review of supercapacitor modeling, estimation, and applications: A control/management perspective. *Renewable and Sustainable*

Energy Reviews vol. 81 1868–1878 Preprint at https://doi.org/10.1016/j.rser.2017.05.283 (2018).

26. Stambouli, A. B. & Traversa, E. *Fuel Cells, an Alternative to Standard Sources of Energy*. *Renewable and Sustainable Energy Reviews* vol. 6 www.elsevier.com/locate/rser (2002).
27. Abdelkareem, M. A. *et al.* Environmental aspects of fuel cells: A review. *Science of the Total Environment* **752**, (2021).
28. Stambouli, A. B. & Traversa, E. *Fuel Cells, an Alternative to Standard Sources of Energy*. *Renewable and Sustainable Energy Reviews* vol. 6 www.elsevier.com/locate/rser (2002).
29. Wang, C. Y. Fundamental models for fuel cell engineering. *Chem Rev* **104**, 4727–4765 (2004).
30. Sundmacher, K. Fuel cell engineering: Toward the design of efficient electrochemical power plants. in *Industrial and Engineering Chemistry Research* vol. 49 10159–10182 (2010).
31. Bhagat, S., Sapkal, V. S. & Gadge Baba, S. *A Review on the Fuel Cells Development*. www.sadgurupublications.com (2011).

Chapter 2. Techniques

2.1 Structural Characterization techniques

2.1.1X-ray Diffraction

X-ray Diffraction, or XRD, is a powerful analytical technique widely used to determine the crystalline structure of materials, with applications across chemistry, materials science, geology, and physics. The method involves directing X-rays onto a crystalline sample, where they scatter upon encountering the atoms in the material. This scattering produces a unique diffraction pattern that reveals detailed information about the crystal's internal arrangement.

The underlying principle of XRD is based on Bragg's Law, which describes the relationship between the wavelength of the X-rays, the angle at which they are scattered, and the distance between planes of atoms in the crystal. Bragg's Law is mathematically expressed as (Eq. 2.1):

$$n\lambda = 2dsin\theta \tag{2.1}$$

Where n is an integer representing the order of reflection, λ is the wavelength of the X-rays, d is the distance between the atomic planes, and θ is the angle of incidence. When the conditions of Bragg's law are met, constructive interference (where scattered waves add up coherently) occurs, producing distinct peaks in the diffraction pattern that correspond to the interplanar spacings within the crystal.

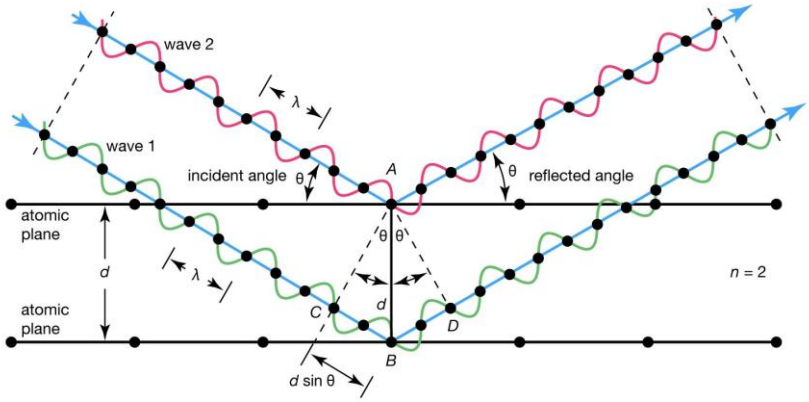

Fig. 2.1 Bragg's Law schematic

By analysing this pattern, scientists can deduce the lattice parameters and the overall crystal structure, allowing the identification of specific phases within the sample. XRD can also measure particle sizes, quantify phases in mixed samples, and assess internal strain. Because of its precision in revealing atomic-scale details, XRD is a crucial tool in the development of new materials, quality control in production, and understanding the fundamental properties of crystalline

substances.

In addition, from XRD the crystallite site can be found out using Scherrer's formula (Eq. 2.2):

$$D = \frac{k\lambda}{\beta cos\vartheta} \tag{2.2}$$

Where: D is crystallite site, k is the shape factor, λ is the wavelength, β is the FWHM and υ is the diffraction angle[1].

2.1.2 Rietveld Refinement

Rietveld refinement is a powerful analytical technique used in crystallography to extract detailed structural information from X-ray or neutron powder diffraction data. Developed by Hugo Rietveld in 1969, the method involves fitting a calculated diffraction pattern to the observed data by adjusting various structural parameters, such as lattice constants, atomic positions, thermal vibrations, and site occupancies. This iterative process minimizes the difference between the experimental and theoretical patterns using a least-squares approach. Rietveld refinement is especially valuable for characterizing complex or multiphase materials, allowing researchers to determine precise crystallographic structures, quantify phase compositions, and analyze microstructural features like crystallite size and strain.

2.1.3 Raman spectroscopy

Raman analysis is a powerful technique based on the principle of inelastic scattering, also known as Raman scattering, where light interacts with a molecule in a way that changes its energy. When monochromatic light—typically from a laser—strikes a sample, most photons scatter elastically, meaning they retain their original energy. This primary type of scattering, called Rayleigh scattering, does not provide information about the molecular structure. However, a small fraction of photons scatters inelastically, gaining or losing energy by interacting with the molecular vibrations of the sample. This energy shift is characteristic of the vibrational modes of the molecules, making Raman scattering a valuable tool for identifying chemical composition, molecular bonds, and structural details.

The fundamental equation that describes the energy shift observed in Raman scattering is the Raman shift, expressed as (Eq. 2.3):

$$\Delta\nu = \nu_0 - \nu_s \tag{2.3}$$

Where ν_0 is the frequency of the incident light and ν_s is the frequency of the scattered light. The difference, $\Delta\nu$, represents the vibrational energy levels of the molecule, providing a molecular "fingerprint." This shift can be positive or negative, corresponding to Stokes or anti-Stokes scattering, respectively. In Stokes scattering, the scattered photon loses energy to the molecule,

resulting in a lower energy photon; in anti-Stokes scattering, the molecule transfers energy to the photon, resulting in a higher energy photon.

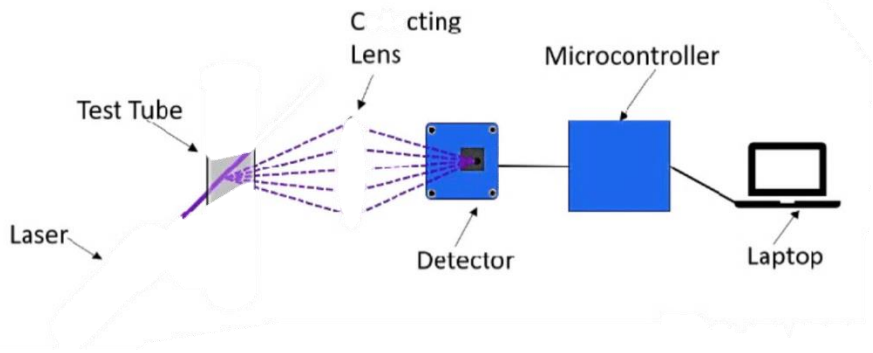

Fig. 2.2 Raman Spectroscopy Instrumental set up

An important principle in Raman analysis is the selection rule: only vibrational modes that change the polarizability of the molecule are Raman active, meaning they can be detected in a Raman spectrum. The intensity of the Raman scattered light, I, is influenced by the polarizability of the molecule, described by (Eq. 2.4):

$$I \propto (\alpha)^2 \tag{2.4}$$

Where α is the rate of change of polarizability with respect to the vibrational coordinate. A strong signal typically indicates a large change in polarizability, which is common for certain types of molecular bonds and structures. Raman analysis is highly specific, making it an excellent tool for identifying chemical compounds and studying molecular interactions in various fields, from chemistry to materials science and biology[2].

2.1.4 Scanning Electrode Microscopy

Scanning Electron Microscopy (SEM) is a technique that allows for detailed imaging of a sample's surface at high magnification and resolution. SEM works by focusing a beam of high-energy electrons onto the sample's surface. As these electrons interact with the atoms in the sample, they generate secondary electrons, backscattered electrons, and characteristic X-rays, each carrying specific information about the surface composition, texture, and topography.

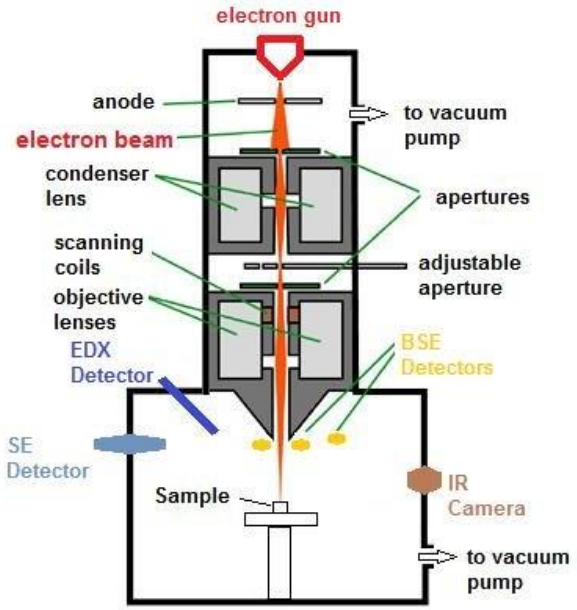

Fig. 2.3 Scanning Electron Microscopy Instrumental set up

The electron beam in SEM is typically accelerated to high voltages, commonly ranging from 1 to 50 kV. When it strikes the sample, various signals are generated. Secondary electrons, produced close to the sample surface, are primarily responsible for creating high-resolution images. Because they escape from the upper few nanometers of the surface, they provide fine details of the sample topography and are commonly used to map surface features.

Backscattered electrons, on the other hand, are reflected from deeper within the sample and are more sensitive to atomic number differences within the material. This makes backscattered electron imaging useful for distinguishing regions with different elemental compositions, as higher atomic number elements scatter more electrons, producing a brighter contrast in the image.

Characteristic X-rays emitted during electron-sample interactions can be analyzed using Energy-Dispersive X-ray Spectroscopy (EDS or EDX). EDS is an important adjunct to SEM that provides elemental composition data. Each element in the sample emits X-rays with a unique energy signature, allowing precise qualitative and quantitative analysis of the sample's composition.

The SEM resolution depends on the electron spot size and the interaction volume, with modern SEMs achieving resolutions down to few nanometers, providing clear insights into microstructures[3].

2.1.5 Transmission Electron Microscopy

Transmission Electron Microscopy (TEM) is an imaging technique that offers extremely high resolution, enabling visualization of sample structures at the atomic or near-atomic level. Unlike Scanning Electron Microscopy (SEM), which scans the surface of a sample, TEM passes a

beam of electrons *through* an ultrathin specimen. This allows TEM to capture fine details of the sample internal structure, providing insight into its morphology, crystallography, and chemical composition.

In TEM, electrons are accelerated to very high energies, often in the range of 60 to 300 kV, and directed toward a very thin sample, typically less than 100 nanometers thick. When the high-energy electron beam interacts with the sample, various effects occur, including electron scattering, which can be either elastic (without energy loss) or inelastic (with energy loss). These scattered electrons are then detected and used to form images or gather diffraction patterns.

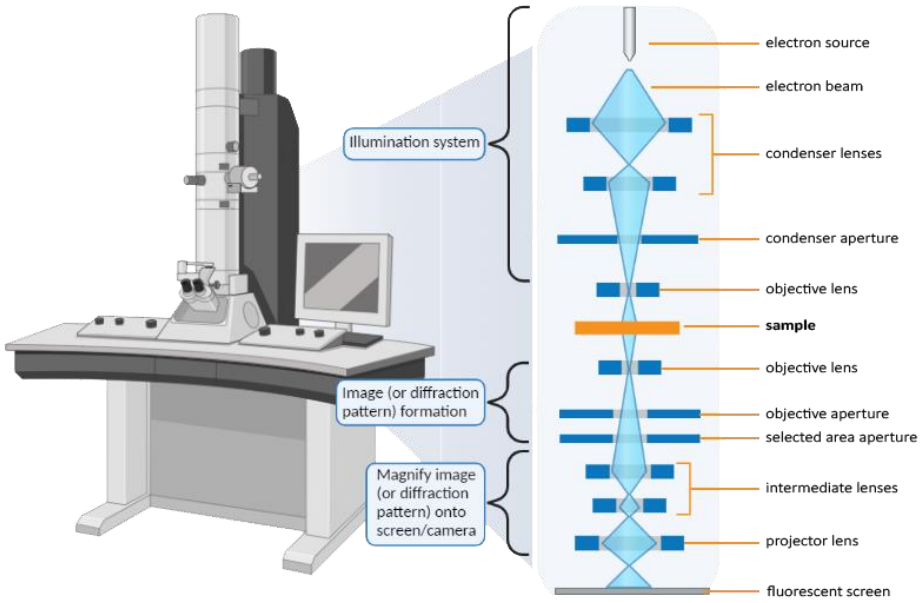

Fig. 2.4 Trasmission Electron Microscopy Instrumental set up

The most common imaging mode in TEM is bright-field imaging, where only the directly transmitted (non-scattered) electrons are used to form the image, resulting in a contrast where higher-atomic-number or crystalline areas appear darker because they scatter more electrons out of the beam path. Dark-field imaging can also be employed, where only the scattered electrons contribute to the image, enhancing contrast in regions with certain crystal orientations or densities.

TEM also offers powerful techniques like selected area electron diffraction (SAED), which allows researchers to analyse the crystalline structure of specific sample regions. The diffraction patterns generated by SAED reveal the atomic arrangement and can be used to determine phase, crystallinity, and orientation.

High-Resolution TEM (HRTEM) enables direct visualization of electron density, making individual atomic columns in crystalline materials visible. This resolution is achieved through advanced electron optics and is enhanced by aberration-correction technologies, allowing images with sub-angstrom clarity.

In addition to imaging, TEMs can be equipped with Energy-Dispersive X-ray Spectroscopy (EDS) and Electron Energy Loss Spectroscopy (EELS) detectors. EDS, like in SEM, provides information on the sample elemental composition by detecting characteristic X-rays emitted by atoms in the sample. EELS, however, measures the energy lost by electrons as they pass through the sample, offering information on chemical bonding, valence states, and even atomic structure at very high resolution.

Due to its ability to reveal both structural and compositional information at an atomic scale, TEM is an invaluable tool in materials science, nanotechnology, biology, and solid-state physics. However, sample preparation for TEM can be challenging and time-intensive, as it requires the specimen to be extremely thin and stable under electron bombardment[4].

2.1.6 X-ray Photoelectron spectroscopy

X-ray Photoelectron Spectroscopy (XPS), also known as Electron Spectroscopy for Chemical Analysis (ESCA), is a surface-sensitive analytical technique used to determine the elemental composition, chemical state, and electronic structure of materials. XPS relies on the photoelectric effect, where X-rays directed to the sample cause the emission of core-level electrons. By measuring the kinetic energy of these emitted electrons, XPS can provide valuable information about the atoms within a few nanometers of the material surface.

When X-rays (commonly Al Kα or Mg Kα) irradiate a sample, they impart energy to core electrons in the atoms. If the energy is sufficient to overcome the electron's binding energy, the electron is ejected from the atom as a photoelectron. The kinetic energy (E_k) of this photoelectron is measured by an electron analyzer. Using the Eq. 2.5:

$$E_k = h\nu - E_b - \phi \tag{2.5}$$

Where:

- Ek is the kinetic energy of the photoelectron,
- $h\nu$ is the photon energy of the incident X-ray,
- E_b is the binding energy of the electron in the atom,
- ϕ is the work function of the spectrometer.

By rearranging the equation to solve for E_b, the binding energy of each electron can be determined. The binding energy is unique to specific elements and their chemical environments, making XPS highly effective for elemental identification and analysis of chemical states.

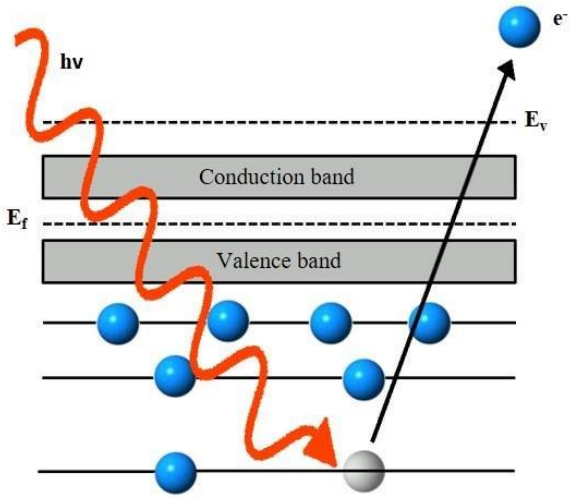

Fig. 2.5 X-ray Photoelectron Spectroscopy principles

XPS spectra display peaks corresponding to the different core electrons of atoms present in the sample. The position of these peaks reveals the element and, often, the chemical state of the atom, since slight shifts in binding energy (chemical shifts) occur due to variations in oxidation states or bonding environments. For example, carbon in different oxidation states (C-C, C=O, C-OH) will exhibit peaks at distinct binding energies, allowing for detailed chemical analysis of the surface.

The technique surface sensitivity arises because only electrons emitted from the top few nanometers escape without energy loss, making XPS ideal for studying surface composition and thin films. XPS can also provide depth profiling by gradually sputtering the surface with ions to remove layers and analyze successive depths, enabling a detailed compositional profile through the sample.

Additionally, the analysis of the intensity of peaks in an XPS spectrum allows for semi-quantitative analysis, providing information on the relative abundances of elements[5].

2.2 Electrochemical Characterization Techniques

2.2.1 Chronopotentiometry

Chronopotentiometry is an electrochemical technique used to evaluate the performance of energy storage devices like batteries and supercapacitors. It involves cycling a cell by applying a constant current during the charging and discharging phases and monitoring the resulting voltage, which allows researchers to control and analyze the electrochemical reactions occurring within the device.

In a typical experiment in GCPL mode (Galvanostatic Cycling with Potential Limitation), the cell is charged with a constant current until it reaches a predetermined upper potential limit, preventing overcharging. Once this limit is reached, the current is stopped and the charge may be completed by applying a constant voltage. The same process occurs during discharging, where the cell discharges at a constant current until it hits a specified lower potential limit.

The resulting voltage vs. charge profiles provide critical information about the device charge and discharge capacities, efficiency, and energy losses. By analyzing these profiles, researchers can gain insights into the electrochemical performance of different electrode materials and electrolytes, helping to optimize energy storage technologies and improve their efficiency and stability over time.

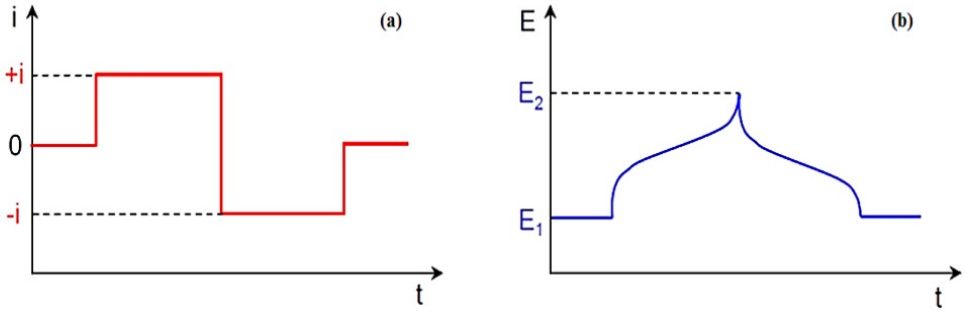

Fig. 2.6 GCPL scheme

2.2.2 Cyclic Voltammetry (CV) and Linear Sweep Voltammetry (LSV)

Cyclic Voltammetry (CV) and Linear Sweep Voltammetry (LSV) are electrochemical techniques widely used to study the redox behavior of electroactive species, assess reaction kinetics, and analyze the electrochemical properties of materials.

Cyclic Voltammetry involves cycling the potential of an electrode linearly over time, allowing for both oxidation and reduction reactions to occur. The resulting current is measured as a function of the applied potential, generating a voltammogram that displays distinct peaks corresponding to the oxidation and reduction processes. CV is particularly useful for investigating reaction mechanisms, determining the formal potentials of redox couples, and studying the stability and reversibility of electrochemical reactions[6].

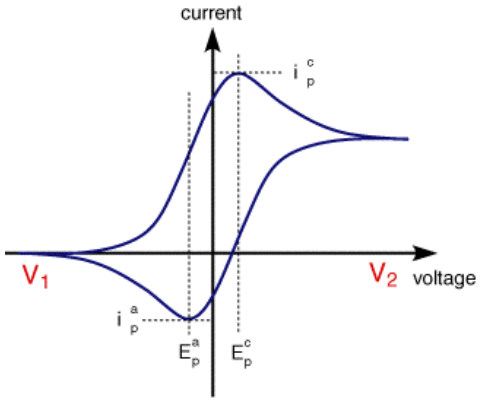

Fig. 2.7 Cyclic Voltammetry scheme

In contrast, Linear Sweep Voltammetry applies a continuous linear change in potential to the working electrode, measuring the current response as the potential sweeps in one direction until a specified limit is reached. LSV is often employed for determining the electrochemical characteristics of materials, such as their activity, onset potentials for reactions, and overall kinetics.

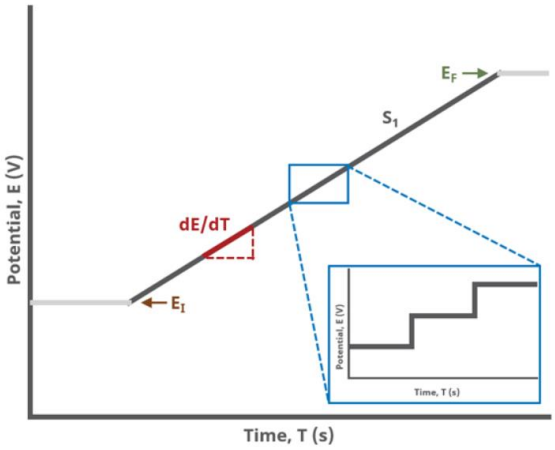

Fig. 2.8 LSV scheme

Both techniques provide valuable insights into the electrochemical behaviour of materials and are essential tools in fields such as battery research, corrosion studies, and sensor development. By analyzing the resulting voltammograms, researchers can gain a deeper understanding of electron transfer processes, reaction mechanisms, and the stability of electroactive species under different conditions.

2.2.3 Electrochemical Impedance Spectroscopy (EIS)

Electrochemical Impedance Spectroscopy (EIS) is an advanced technique used to analyse the electrochemical properties of materials and interfaces. By applying an alternating current (AC) signal over a range of frequencies (either in current- or potential-controlled mode), EIS measures the impedance, or opposition to current flow, of an electrochemical system. This frequency-dependent impedance data provides a detailed view of the system resistive and capacitive behavior,

offering insights into reaction kinetics, charge transfer processes, and mass transport limitations.

In an EIS experiment, the response of the system to the AC signal is recorded, typically across frequencies from a few millihertz to several kilohertz. At high frequencies, EIS data reflect processes occurring at the electrode-electrolyte interface, often highlighting charge transfer resistance and double-layer capacitance. At low frequencies, the data capture slower processes, such as diffusion of ions within the electrolyte, which are essential for studying processes in batteries, fuel cells, and corrosion systems.

EIS data are usually represented in Nyquist or Bode plots, which visualize the complex impedance in ways that allow for interpretation of different electrochemical parameters. By fitting EIS data to an equivalent electrical circuit model, researchers can identify specific resistances, capacitances, and diffusion-related impedances in the system, facilitating a deeper understanding of the material performance and limitations. This makes EIS invaluable for optimizing electrochemical devices, diagnosing degradation, and improving designs for energy storage and conversion technologies[7].

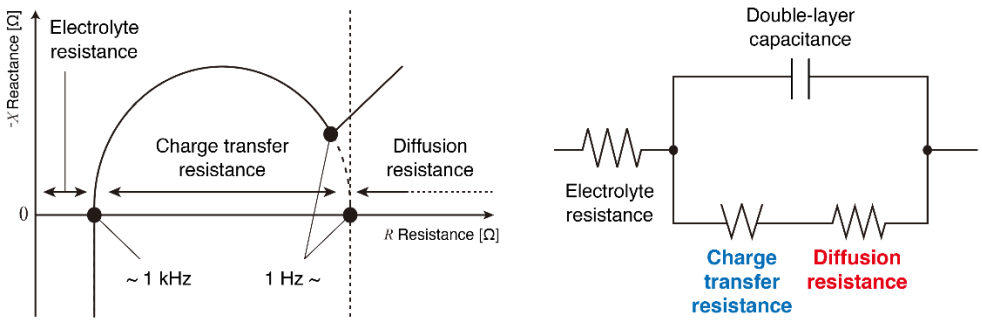

Fig. 2.9 EIS scheme

Reference

1. Epp, J. X-Ray Diffraction (XRD) Techniques for Materials Characterization. in *Materials Characterization Using Nondestructive Evaluation (NDE) Methods* 81–124 (Elsevier Inc., 2016). doi:10.1016/B978-0-08-100040-3.00004-3.
2. Cialla-May, D., Schmitt, M. & Popp, J. Theoretical principles of Raman spectroscopy. *Physical Sciences Reviews* vol. 4 Preprint at https://doi.org/10.1515/psr-2017-0040 (2019).
3. Akhtar, K., Khan, S. A., Khan, S. B. & Asiri, A. M. Scanning electron microscopy: Principle and applications in nanomaterials characterization. in *Handbook of Materials Characterization* 113–145 (Springer International Publishing, 2018). doi:10.1007/978-3-319-92955-2_4.
4. Kannan, M. *Transmission Electron Microscope-Principle, Components and Applications Illumination System (Electron Gun and Condenser Lenses) Electron Gun*.
5. Schultze, J. W. & Bressel, A. *Principles of Electrochemical Micro-and Nano-System Technologies*. *Electrochimica Acta* vol. 47 www.elsevier.com/locate/electacta (2001).
6. Marken, F., Neudeck, A. & Bond, A. M. Cyclic voltammetry. in *Electroanalytical Methods: Guide to Experiments and Applications* 57–106 (Springer Berlin Heidelberg, 2010). doi:10.1007/978-3-642-02915-8_4.
7. Magar, H. S., Hassan, R. Y. A. & Mulchandani, A. Electrochemical impedance spectroscopy (Eis): Principles, construction, and biosensing applications. *Sensors* vol. 21 Preprint at https://doi.org/10.3390/s21196578 (2021).

Chapter 3.

3.1 Investigation of the doping effect of a Mg/Zr-Modified $LiNi_{0.5}Mn_{1.5}O_4$ Cathode on the charge transfer and transportation proprieties

$LiNi_{0.5}Mn_{1.5}O_4$ (LNMO) is a promising candidate, providing a high-voltage Co-free cathode option with an operating voltage around 4.7 V (vs. Li^+/Li) and a theoretical specific capacity of ~147 mAh/g. However, LNMO suffers from capacity decay during extended charge-discharge cycles, especially under higher stressing conditions such as temperatures or at elevated C-rates, which limits its potential for large-scale commercialization. This limitation is partially linked to phase transitions during charge-discharge, as well as structural instability at high voltage[29–31].

Improving the electrochemical performance of LNMO requires a deeper understanding of its reaction mechanisms and the kinetics of solid-state phase transformations. During charge, Li^+ extraction induces "multiple cubic phase transitions" in LNMO, which significantly alter lattice parameters, introduce mechanical strain, and degrade energy density, power output, and cycling stability[29,30,32,33]. Additionally, under high operating potential, the arrangement of cations becomes unstable in the highly delithiated phase. This instability is mainly due to Ni migration from the spinel structure, forming a rock salt-like phase, which increases impedance, slows electrochemical kinetics, and contributes to capacity loss with cycling. At elevated voltages, cell degradation is also exacerbated by increased parasitic side reactions at high temperatures. Structural instability can further arise from Mn^{2+} dissolution due to the Jahn–Teller effect, particularly at high temperatures[34,35].

To address these challenges and enhance the structural stability of LNMO spinel cathodes, strategies such as element doping, surface coating, and morphological modifications have proven effective in mitigating these issues[36–41]. Several studies have examined the effects of Mg^{2+} substitution in the LNMO crystal lattice, demonstrating that Mg^{2+} doping enhances the electrical conductivity of the spinel and stabilizes its structure during cycling[42,43]. Additionally, the introduction of Zr^{4+} has been shown to suppress the formation of nickel oxide-like impurities linked to the presence of Mn^{3+}, thereby supporting structural stability and extending cycle life[44,45]. Building on prior research on Mg/Zr modifications in layered cathodes, a novel Mg/Zr co-doping strategy is proposed to improve LNMO structural and mechanical stability and mitigate its typical

capacity loss. The charge/discharge performance of cathodes based on both unmodified and co-doped LNMO samples are evaluated. Furthermore, the charge transfer and transportation kinetics of each cathode are analyzed through electrochemical impedance spectroscopy at different states of charge during lithiation and delithiation (SPEIS).

3.1 Experimental

3.1.1 Synthetic methodology

The unmodified (b-LNMO) and modified (m-LNMO) cathodes have been synthesized by a common synthetic route, a sol-gel synthesis already reported in literature[46,47]. In detail, lithium acetate [$Li(CH_3COO)\cdot 2H_2O$], nickel acetate [$Ni(CH_3COO)_2\cdot 4H_2O$], manganese acetate [$Mn(CH_3COO)_2\cdot 4H_2O$], with the addition of magnesium acetate tetrahydrate [$Mg(CH_3COO)_2\cdot 4H_2O$] and zirconium (IV) acetate hydroxide [$Zr(OH)_y\cdot(CH_3COO)_x$, $x + y \sim 4$] for the modified powder, were dissolved in distilled water in stoichiometric amounts corresponding to an expected composition "$LiNi_{0.5}Mn_{1.47}Mg_{0.025}Zr_{0.025}O_4$". A slight excess of total cations (Ni + Mn + dopants) over stoichiometry was introduced, to possibly foster the formation of a Zr oxide coating phase, as previously observed for layered cathodes [48,49]. Citric acid (CA) was then added to the solution as chelating agent, with a molar ratio CA:total metal cations of 1:1 (all materials from Sigma–Aldrich, purity ≥ 99%). After complete solubilization of the reactants, the solution was mixed by continuous stirring at room temperature for a day. The obtained solution was then heated slowly to 100 °C under continuous stirring until a viscous gel was formed. The gel was dried at 100 °C overnight in vacuum oven and the residue was ground to a fine powder. A two-step calcination under air atmosphere was then applied to obtain the final spinel phase. In the first step, the precursor was calcined for 4 h at 480 °C after a heating ramp rate of 2 °C/min. The second step was carried out for 16 h at 800 °C after a hating ramp rate of 3.7 °C/min. The modified cathode was labelled as m-LNMO. The same procedure was adopted for the preparation of b-LNMO, without the addition of Mg and Zr salts.

3.1.2 Chemical, structural, and morphological characterization

The structural properties of the obtained compounds synthetized by sol gel synthesis were investigated by Raman spectroscopy (Horiba IHR 320, wavelength 532 nm) and X-ray diffraction (XRD) (Bragg–Brentano geometry, Cu-Kα, λ = 1.54059Å). The XRD patterns were analyzed with the FullProf program by profile matching. The particle morphology and elemental composition of the synthesized materials were studied using field emission Scanning Electron Microscopy (SEM)

and Energy Dispersive X-Ray elemental analysis (EDX) using FE-SEM Cambridge Stereoscan 360 electron microscope. To get further insight into the morphological features, crystallographic characteristics, and elemental concentrations of both samples, FEI Tecnai G2 Transmission Electron Microscopy (TEM) instrument, equipped with a 200 kV field emission gun and EDX, was utilized. High-Resolution TEM (HRTEM) and selected area electron diffraction (SAED) modes at TEM were carried out for studying and comparing the microstructure of each cathode. The surface chemical composition of LNMO powders was investigated by means of X-ray photoelectron spectroscopy (XPS) using a non-monochromatic twin anode source with Mg Kα (*hv* = 1253.6 eV) operated at 100 W and Al Kα (hv = 1486.6 eV) at 150 W. A Phoibos 150 XPS spectrometer with micro-channel plate and Delay Line Detector (SPECS Surface Nano Analysis), installed in a UHV chamber with a base pressure of $5x10^{-10}$ mbar, was used for photoelectrons collection. The scans were acquired in Fixed Analyzer Transmission mode with 30 eV pass energy and 0.1 eV energy step. The binding energy scale was calibrated by setting the aliphatic C-C bond at 284.8 eV. A Shirley function was employed to simulate the inelastically scattered photoelectrons background, and a Voigt profile (30% Gaussian, 70% Lorentzian) was used as line shape for the photoelectron peaks.

3.1.3 Electrode preparation and electrochemical characterization

The electrodes were prepared using the sample powders (80 wt.%), super P conductive carbon (10 wt.%), Polyvinylidene fluoride (PVDF) (10 wt.%) and appropriate amount of N- methyl pyrrolidone (NMP) as solvent. The slurry was then cast onto Al foil collector by using a doctor blade set at 150 μm thickness, then dried at 80 °C for 3 h. After drying, 9 mm circular electrodes were cut, pressed at 2 tons/cm^2 for 30 s, and vacuum dried at 120°C (Buchi Glass Oven) for 12 hours. The cathodes were assembled in an Ar-filled glove box (H_2O and O_2 values below 0.1 ppm) for electrochemical measurements using CR2032 coin cells and Swagelok T-type cells. 1M $LiPF_6$ in ethylene carbonate (EC)/dimethyl carbonate (DMC) (1:1 in volume) (Solvionic, 99.9%) was used as electrolyte and glass fiber (Whatman GF/A) was utilized as separator. Charge/discharge cycles were carried out using a Bio-Logic VMP3 electrochemical workstation in the potential range between 3.5 and 5 V *vs.* Li^+/Li at different current rates (1C=147 mA g^{-1} assuming for both electrodes a theoretical capacity of 147 mAh g^{-1}). Cyclic Voltammetry (CV) was carried out at a scanning rate of 0.05 mV/s. EIS measurements have been performed on three-electrode Swagelok T-cells, as a function of the state of charge, in potentiostatic mode, by superimposing an AC perturbation of 10 mV, in the frequency range 10 mHz-100 kHz, upon the selected bias potentials. Prior of any measurement, 2 h of potentiostatic pre-conditioning at measurement potential have

been applied to ensure equilibration of the electrodes.

3.2 Results and Discussion

3.2.1 Structural Characterizations

The LNMO spinel exists in two crystal structures: disordered (space group $Fd\bar{3}m$) and ordered (space group $P4_332$). To analyze phase ordering in bare (b-LNMO) and modified (m-LNMO) samples, Raman spectroscopy was employed due to its sensitivity to crystal symmetry. Raman spectra (Fig. 3.1) show disordered spinel features in both samples, with absence of peaks at 218 and 237 cm^{-1}, characteristic of the $P4_332$ structure with ordered Ni^{2+} and Mn^{4+}. The peak at 630 cm^{-1} corresponds to Mn-O stretching in MnO_6 octahedra (A_1g mode), while the 591 cm^{-1} peak ($F2g_1$) relates to Ni-O bonding. Additional peaks at 496 cm^{-1} ($F2g_2$) and 399 cm^{-1} (Eg) are assigned to Ni^{2+}-O stretching. A greater A_1g peak intensity in m-LNMO suggests shorter Li-O_1 distances, indicating an increased Mn^{4+} content. Conversely, the lower Eg intensity in m-LNMO may reflect increased Ni-O bond lengths[32,34,38].

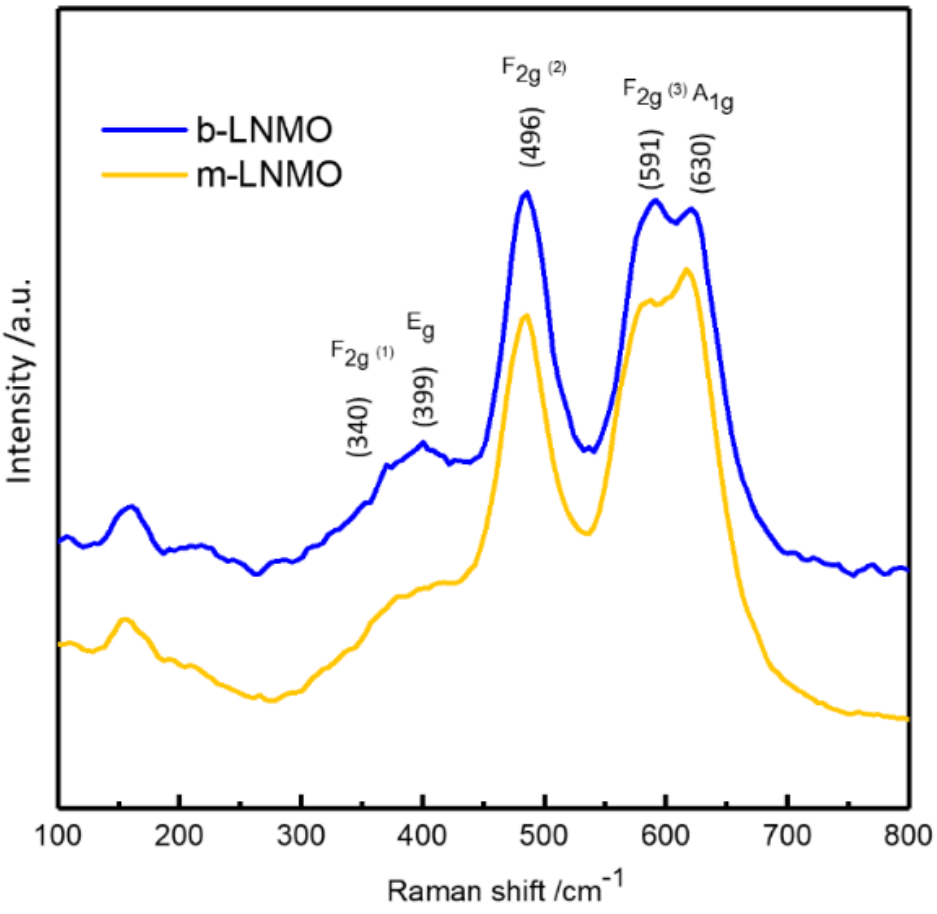

Fig. 3.1 Raman spectroscopy for b-LNMO and m-LNMO

XRD patterns for b-LNMO and m-LNMO powders (Fig. 3.2) confirm $Fd\bar{3}m$ space group for both, indicating that Mg^{2+} and Zr^{4+} doping does not disrupt the inherent cubic spinel structure. Weak reflections at 2θ ~37°, 43°, and 64° in b-LNMO, attributed to $Li_xNi_{1-x}O$ impurity from oxygen loss during high-temperature synthesis which is common for this class of materials and one of the cause of capacity fading. This additional phase was absent in m-LNMO, suggesting Mg/Zr ions may suppress this impurity formation. However, another phase was observed in m-LNMO, Li_2MnO_3 , which was not expected to not impact performance[50–53].

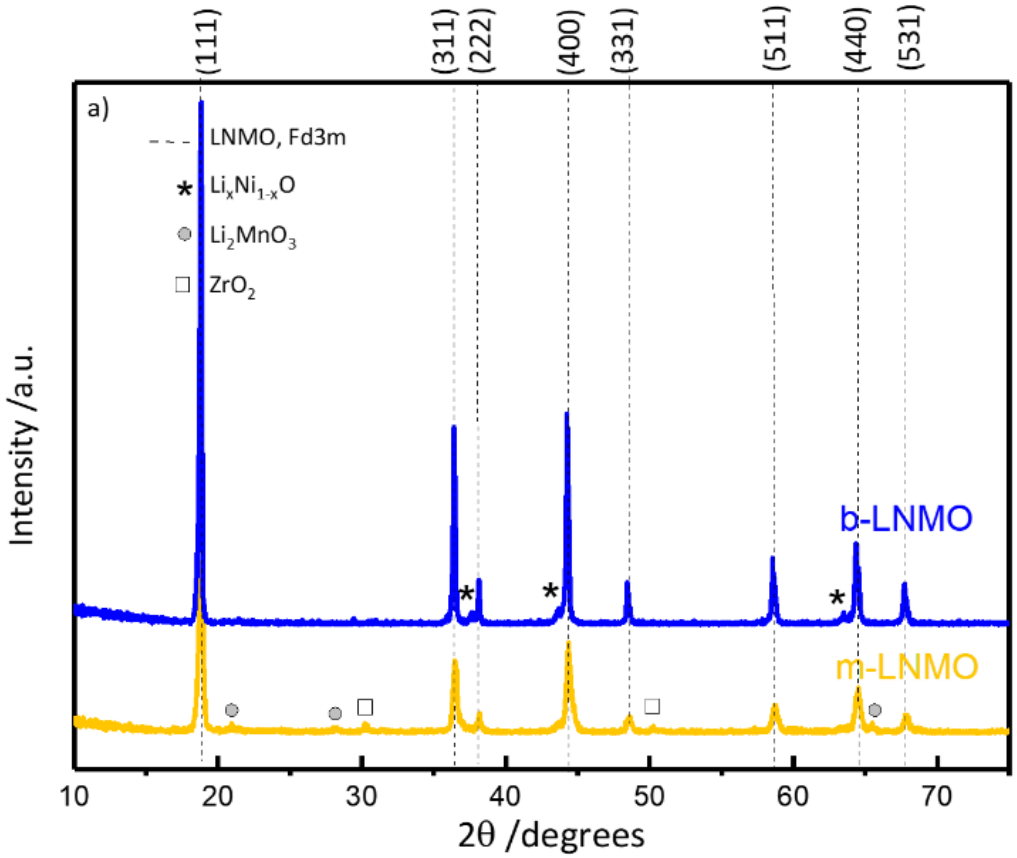

Fig. 3.2 XRD pattern for b-LNMO and m-LNMO

Rietveld refinement (Table 1, Fig. 3.3) reveals a smaller lattice parameter for m-LNMO (8.182 Å) than b-LNMO (8.170 Å), possibly due to reduced Mn^{3+} content and increased cation ordering, which is expected to enhance structural stability and cycle performance[52,53].

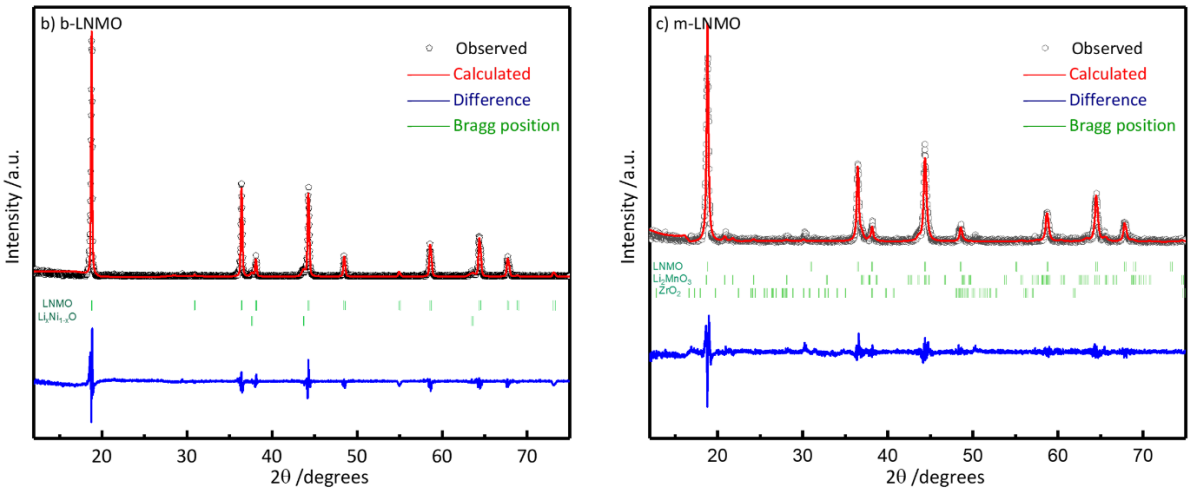

Fig. 3.3 Rietveld refinement graphs for bare LNMO and modified LNMO.

Table 1 Rietveld refinement results for bare LNMO and modified LNMO.

Sample	Lattice parameter (a) (Å)	Cell volume (Å^3)	Rw (%)
b-LNMO	8.182	547.78	3.3
m-LNMO	8.170	543.48	3.1

SEM and HRTEM images (Fig. 3.4) show b-LNMO in micron-sized particles, while m-LNMO comprises nanometer-scale aggregates, with ~5-10 nm particle size (Fig. 3.4h). Smaller particles may increase specific capacity and energy density by shortening the Li^+ diffusion pathway. Selected area electron diffraction (SAED) analysis (Fig. 3.4i-j) aligns with LNMO's $Fd\bar{3}m$ spinel structure. Notably, ZrO_2 reflections in m-LNMO's SAED (Fig. 3k) suggest surface decoration on active material grains, absent in b-LNMO.

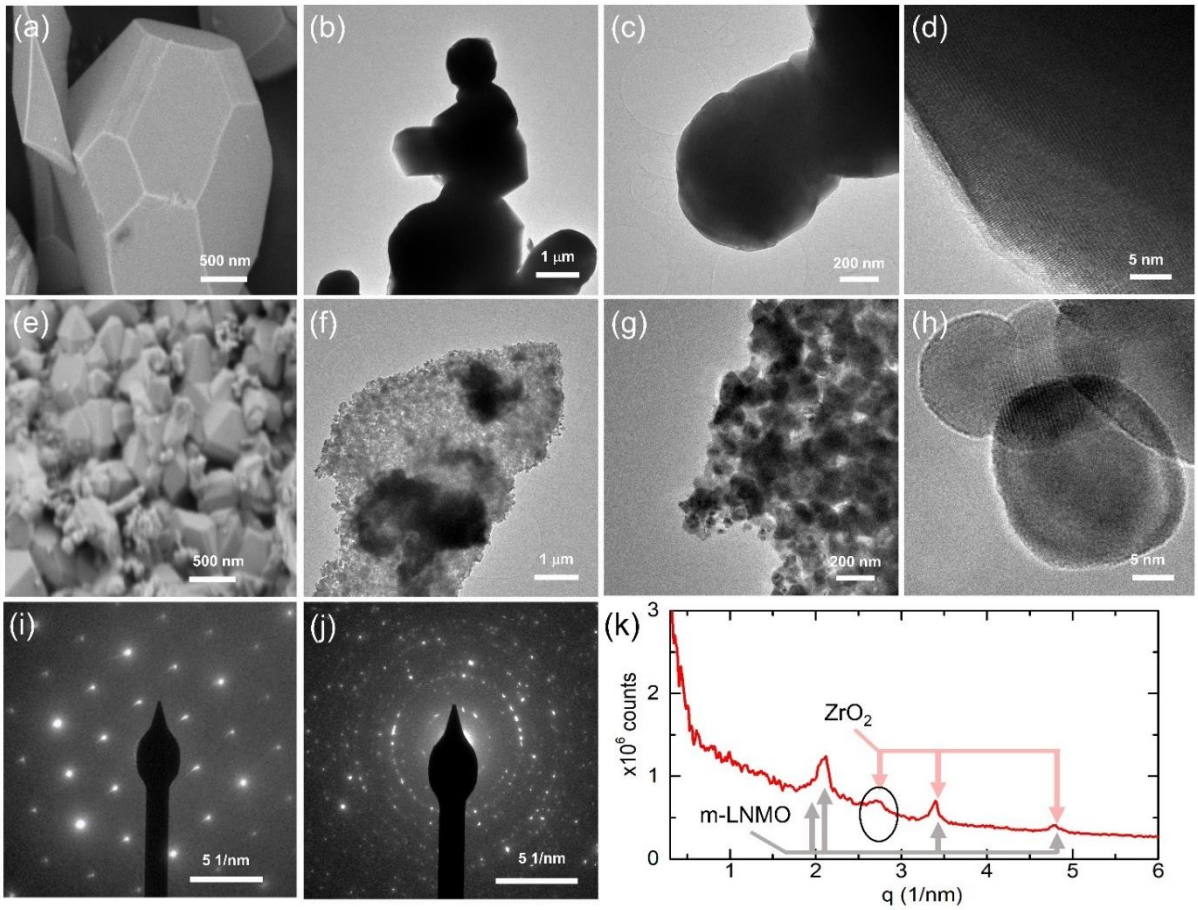

Fig. 3.4 HRTEM for b-LNMO and m-LNMO

EDS (Fig. 3.5a-f) confirms atomic percentage alignment with stoichiometry, detecting Zr and Mg in m-LNMO. Mn determination exhibits a larger error in the modified sample.

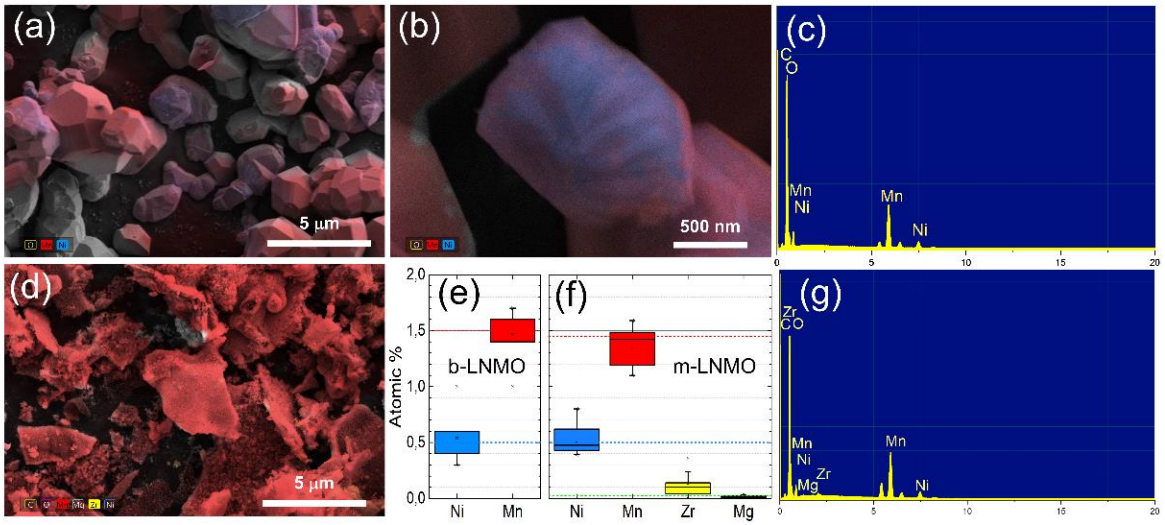

Fig.3.5 SEM, EDX and Mapping for b-LNMO and m-LNMO

XPS analysis (Fig. 5a-d) of Ni 2p, Mn 3s, O 1s, and Zr 3d levels shows minor differences between samples. Ni 2p spectra imply no significant change in Ni chemical state, though b-LNMO

may contain slight Ni^{3+} presence, while m-LNMO favors Ni^{2+}. Mn 3s splitting decreases in m-LNMO (4.35 eV) relative to b-LNMO (4.55 eV), supporting a lower Mn^{3+} concentration in m-LNMO, closer to Mn^{4+}, consistent with XRD results. O 1s spectra displays a main lattice oxygen peak at 529.6 eV, with additional peaks for surface species. Zr 3d spectra in m-LNMO suggest two Zr environments: minor ZrO_2 ($3d_{5/2}$ at 183.0 eV) and a primary peak at 181.8 eV, indicating Zr within the LNMO lattice. In line with the preferential substitution of Mn, the Mn/Ni ratio shifts from 3.4 in b-LNMO to 2.0 in m-LNMO, while the Zr ratio is 0.25 in m-LNMO, confirming Zr incorporation. Mg is also detected but not quantifiable due to peak overlap with Mn[54–56].

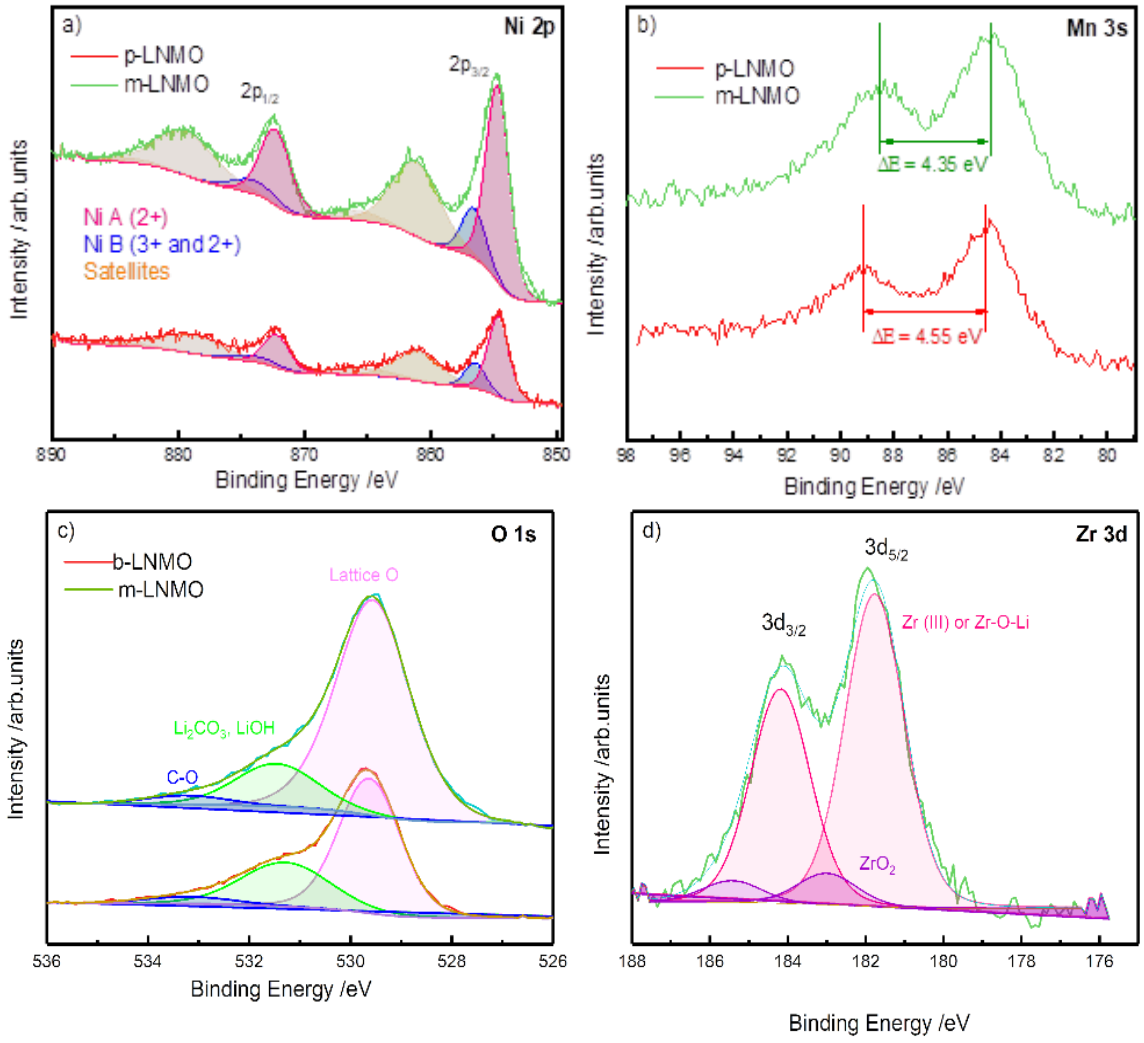

Fig. 3.6 XPS comparison for b-LNMO and m-LNMO

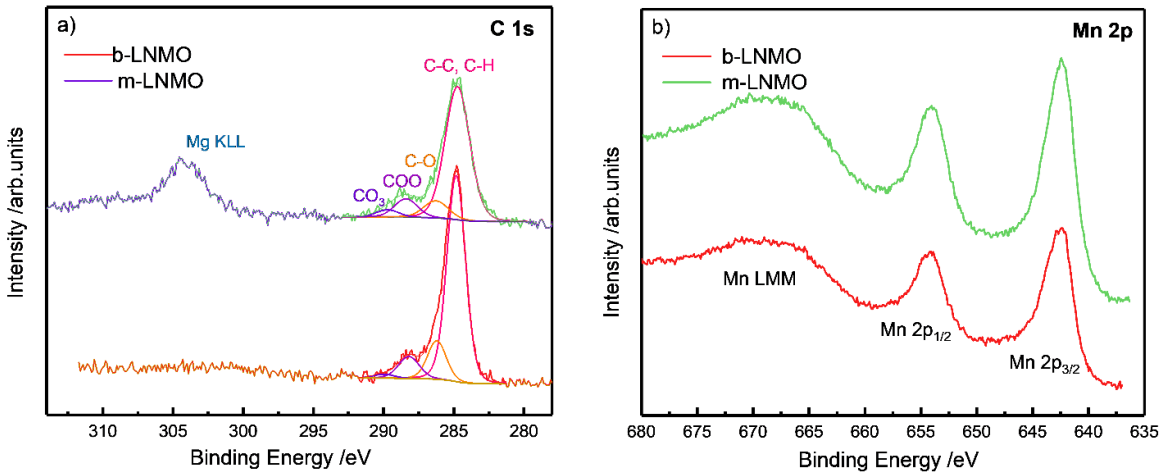

Fig. 3.7 XPS spectra of Carbon and Manganese

3.2.2 Electrochemical Characterizations

To investigate the electrochemical processes occurring on both cathodes during charge and discharge, cyclic voltammetry (CV) was conducted at a scan rate of 0.05 mV s^{-1} within the range of 3.5 to 5 V vs. Li^+/Li at 25°C, as illustrated in Fig. 3.8a, b. Both cathodes display two oxidation peaks at approximately 4.69 V and 4.75 V, with corresponding reduction peaks around 4.64 V and 4.69 V. These redox peaks represent the Ni^{3+}/Ni^{2+} and Ni^{4+}/Ni^{3+} reactions, which are primary electrochemical reactions in LNMO materials. Notably, the voltammetric peaks of m-LNMO are sharper than those of b-LNMO, indicating a lower bulk resistance for the modified material, likely due to doping effects. The reversible plateau near 4.0 V corresponds to the Mn^{4+} /Mn^{3+} redox couple, highlighting the presence of Mn^{3+} and structural disorder in both LNMO samples. However, this feature is less pronounced in m-LNMO compared to b-LNMO, suggesting a higher average Mn oxidation state (thus lower Mn^{3+} content) in the modified sample. Additionally, a peak at ~4.6 V vs. Li^+/Li during the cathodic scan in m-LNMO corresponds to the oxidation of the Li_2MnO_3 phase observed in XRD analysis. This peak disappears after the first oxidation, suggesting irreversible electrochemical activity for Li_2MnO_3[43,57,58].

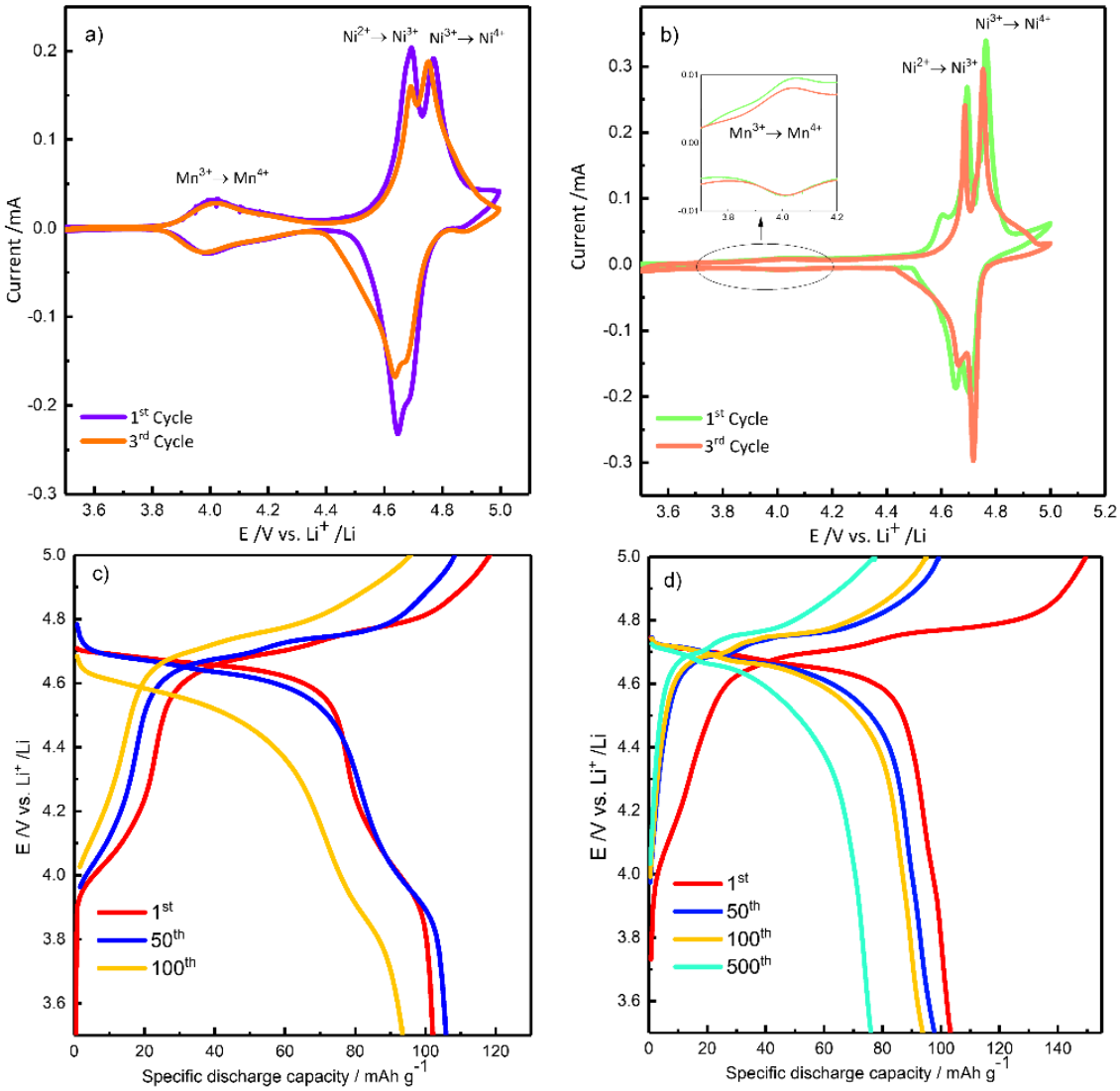

Fig. 3.8 CV and voltage profiles for bare LNMO (a and c) and modified LNMO (b and d).

To assess the impact of the modifications of the material toward cycling performance, two-electrode cells were tested at a 1C charge/discharge rate, with a voltage range from 3.5 to 5.0 V vs. Li^+/Li at 25°C. The E vs. Q profiles for b-LNMO (Fig. 3.8c) and m-LNMO (Fig. 3.8d) exhibit a potential plateau around 4.7 V and a second plateau at 4.0 V, consistent with the CV peaks for Ni^{4+}/Ni^{2+} and Mn^{4+}/Mn^{3+} redox processes, respectively. The LNMO modification significantly suppresses the redox process at ~4.0 V due to reduced Mn^{3+} content.

As shown in Fig. 3.9, the first-cycle discharge capacities for b-LNMO and m-LNMO are 102.4 and 102.8 mAh g^{-1}, respectively, at 1C, with initial coulombic efficiencies (CE) of 86.2% and 68.7%. The lower initial CE of m-LNMO could result from two irreversible processes: (i) Mn^{3+} irreversible oxidation in the Li_2MnO_3 phase, and (ii) more extensive cathode electrolyte interphase (CEI) formation due to a larger interfacial area associated with smaller particle size.

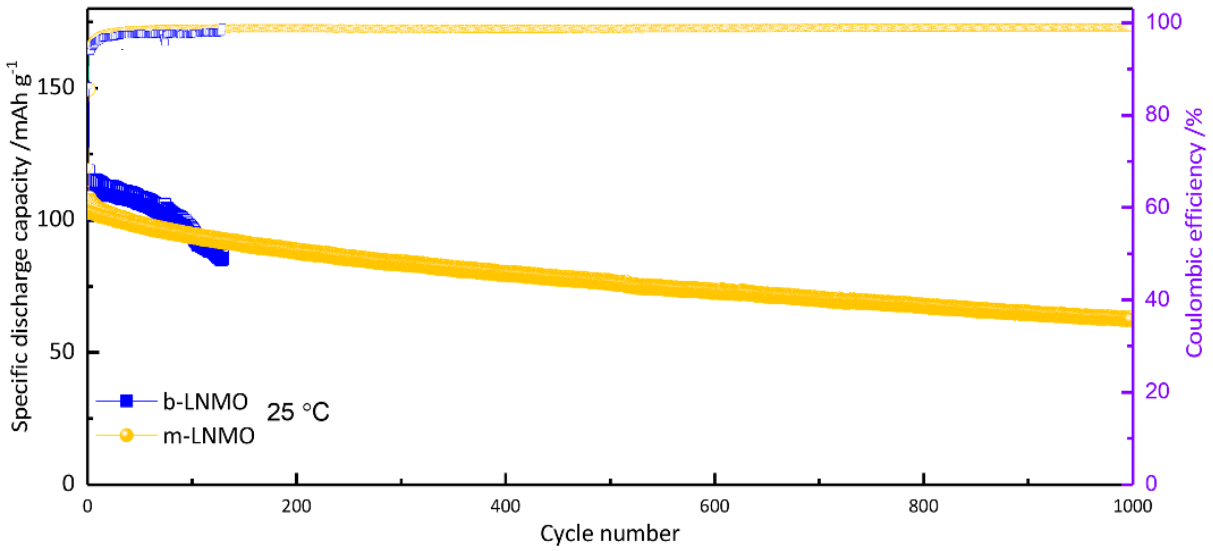

Fig. 3.9 Cycling performance comparison for bare LNMO and modified LNMO

In terms of long-term cycling, b-LNMO and m-LNMO show similar performance for the first 100 cycles, after which b-LNMO undergoes rapid capacity decay, resulting in cell failure after approximately 130 cycles. In contrast, m-LNMO retains 80% capacity after 400 cycles and 60.7% after 1000 cycles, with CE values consistently above 99.0% up to the 1000th cycle, compared to 97.8% for b-LNMO until cell failure. For a deeper evaluation, m-LNMO was tested under demanding conditions at 50°C and a 2C charge/discharge rate (3.5V ≤ E ≤ 5V). As shown in Fig. 3.10, the initial discharge capacity of m-LNMO was 119.4 mAh g^{-1}, stabilizing at 100.5 mAh g^{-1} with a CE of 97.5% and ~72.8% cycling stability after 1000 cycles. The improved capacity retention, particularly under elevated temperature and C-rate, is likely due to the Mg- and Zr-modification, which contributes to: (i) suppression of the rock-salt-type $Li_xNi_{1-x}O$ impurity phase via Ni^{2+} substitution by Mg^{2+} or Zr^{4+} ions ; (ii) reduction in Mn^{3+} content through partial dopant substitution (potentially Zr^{3+}, as indicated by XPS), minimizing Jahn–Teller distortions and interfacial side reactions, thus stabilizing the structure; (iii) smaller grain size, which shortens Li diffusion pathways in the solid;

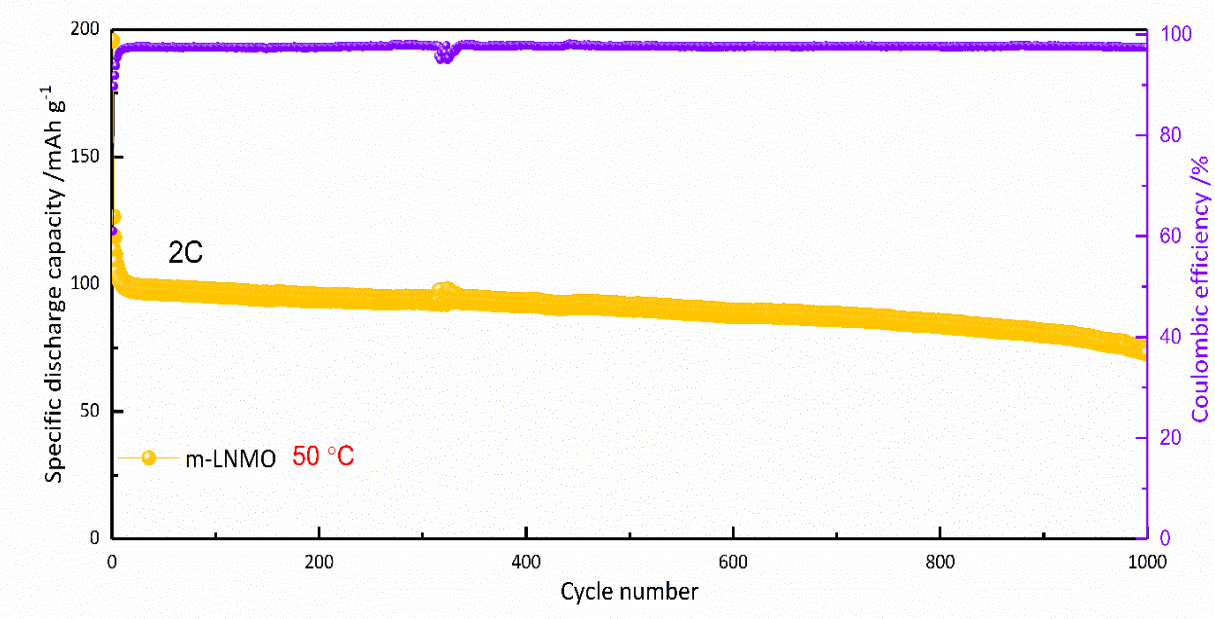

Fig. 3.10 Cycling performance for bare LNMO and modified LNMO at 50°C and 2C.

Electrochemical impedance spectroscopy (EIS) was performed during the initial charge/discharge cycle of both b-LNMO and m-LNMO to examine the impact of structural transitions on charge/discharge kinetics. Using staircase potentiostatic electrochemical impedance spectroscopy (SPEIS) in the 3.5-5 V range with 25 mV steps, the Nyquist plots for b-LNMO and m-LNMO (Fig. 3.11a-h) highlight distinct impedance characteristics based on the state of charge and sample investigated. EIS analysis reveals multiple impedance contributions across frequencies, including, from high to low frequencies: an offset from the Y-axis indicating the electrolyte resistance, a first semicircle indicating the Li^+ migration at the cathode electrolyte interface (CEI), a second semicircle representing the charge-transfer resistance, a third semicircle indicating the bulk electronic resistance, finally a straight line representing the resistance to diffusion through the blocking electrode (Fig. 3.11).

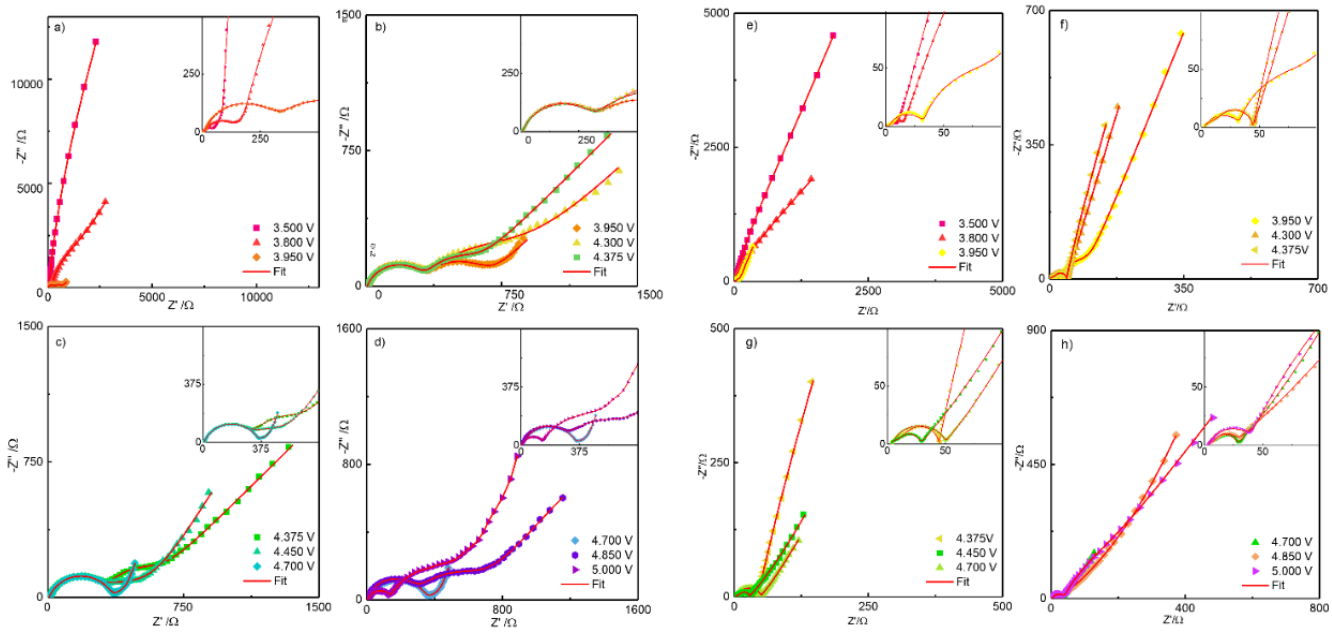

Fig 3.11 Comparison of first oxidation Nyquist plots for b-LNMO (a-d) and m-LNMO (e-h)

Detailing b-LNMO (Fig. 3.12) behavior, a notable trend in the low-frequency semicircle diameter corresponds to structural transitions between insulating and conducting phases. In detail, an alternating trend of overall resistance can be observed.

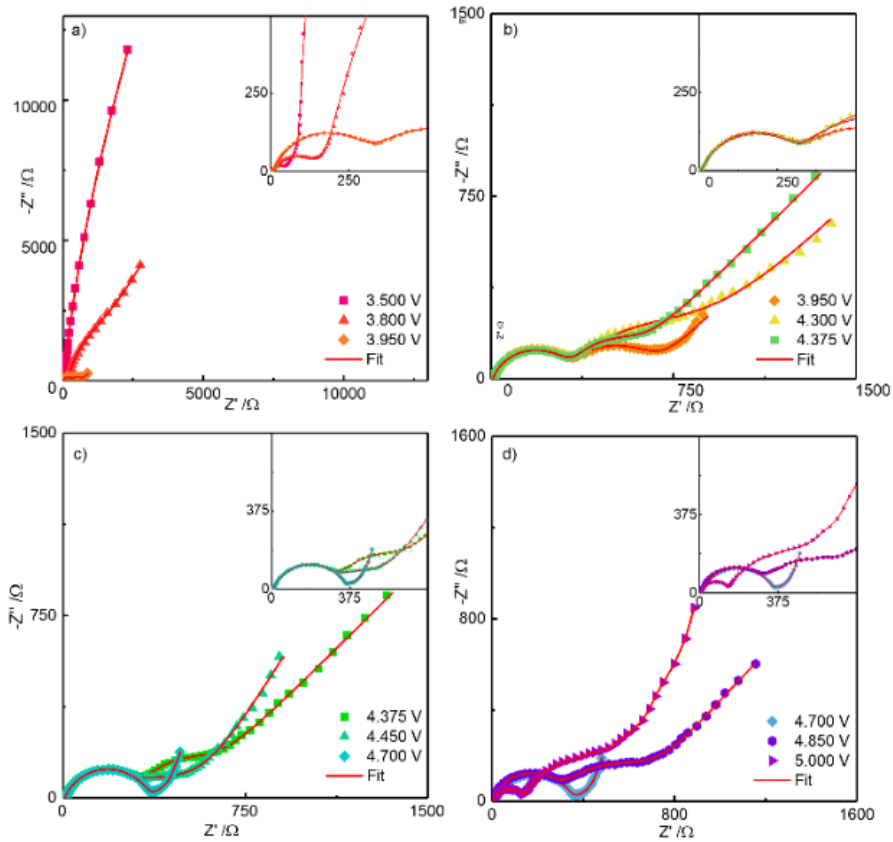

Fig 3.12 First oxidation Nyquist plots for b-LNMO

In contrast, m-LNMO shows a more continuous contraction of the low-frequency arc during charge, suggesting fewer structural rearrangements due to Mg- and Zr-modification.

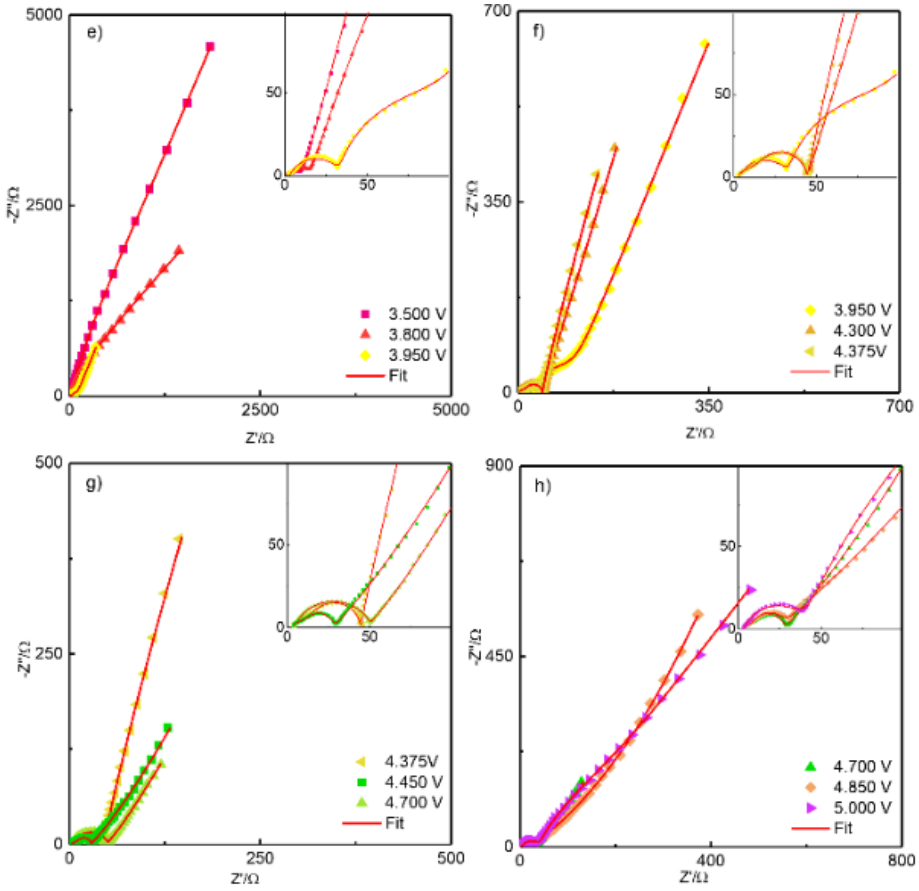

Fig. 3.13 First oxidation Nyquist plots for m-LNMO

When the first reduction is taken into account, for both electrodes an inverse trend in the overall resistance can be observed, indicating the reversibility of the processes.

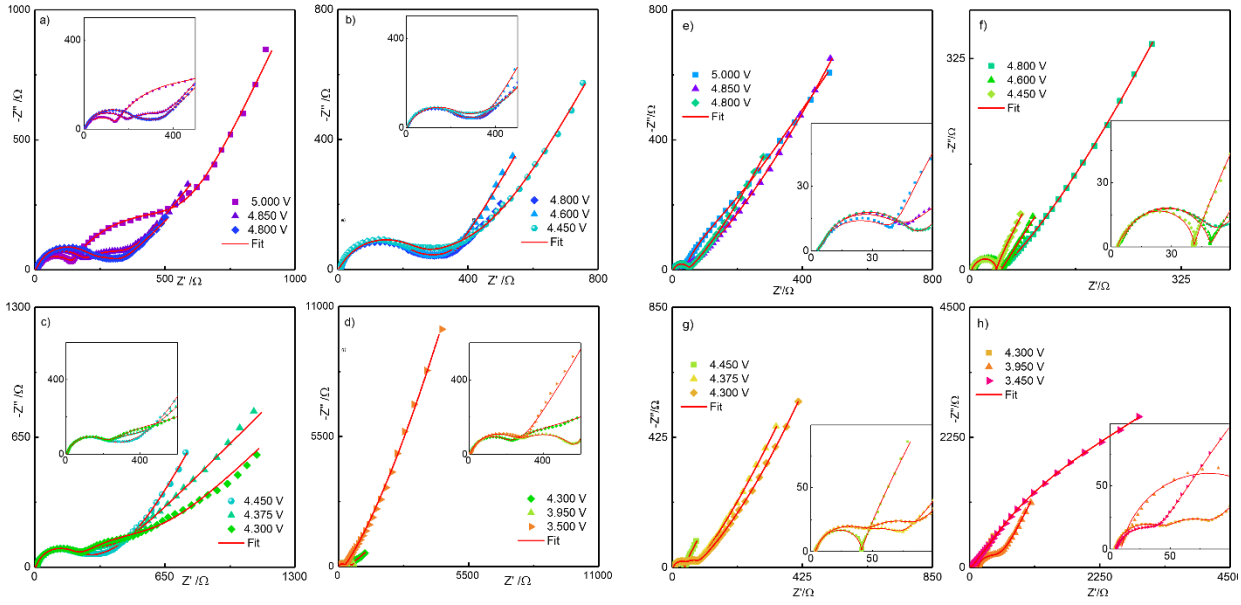

Fig 3.14 Comparison of the first reduction Nyquist plot for b-LNMO and m-LNMO

The equivalent circuit model was applied to analyze the values of the resistances and capacitances (Rsol, R_{CEI} and C_{CEI}, Rct and C_{dl}, R_{elec} and C_{elec}) across the 3.5-5 V range (Fig. 3.15) upon first oxidation and reduction, providing a quantitative view of the evolution of ionic/electronic transport properties during the first charge and discharge. The equivalent circuit was designed taking into account all the processes previously identified in the Nyquist plots, and was designed in the following way: a costant phase element indicating the resistance of the electrolyte (R_{sol}), a first parallel resistance and capacitance elements indicating the resistnace of the CEI (R_{CEI}), a second parallel resistance and capacitance elements representing the Resistance of the Charge transfer processes (R_{Ct}), a third parallel resistance and capacitance elements indicating the electronic conduction resistance of the bulk electrode (R_{elec}) and a final constant warburg element representing the diffusion resistance thourgh the blocking electrolyte (W) and a differential intercalation capacitance (C_i).

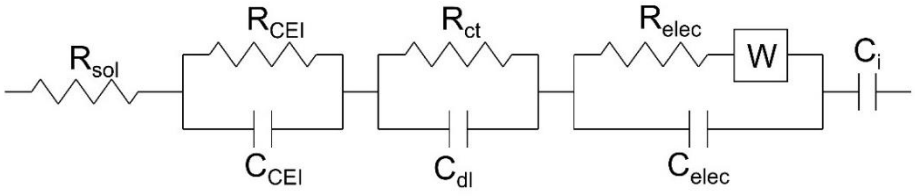

Fig. 3.15 Equivalent circuit applied on the EIS data for both materials

For b-LNMO, Relec exhibits a pattern of contraction and expansion across specific voltage intervals, influenced by the concurrent evolution of electronic conductivity and of structural rearrangement phenomena. In the mid region of potentials, (from 4 V to 4.6 V), the b-LNMO suffers of multicubic phase transition which is one of the reasons of the capacity fading. In addition, at the potential near to the end of charge, from 4.6 V to 5 V the electronic resistance rises again. This is due to the formation of the rock salt phase typical of LNMO materials in which the Nickel atoms migrate into the Lithium interstitial sites blocking the Lithium diffusion through the electrode. m-LNMO, however, shows a consistent decrease in Relec upon charge, indicating that the evolution of electronic conductivity is primarily controlled by Li^+ extraction (as for [ref. Croce et al., Electrochemical Communications 1999][59]), with minimal phase change-induced conductivity fluctuations as is possible to observe by the Relec trends the m-LNMO shows the suppression of the multicubic phase transition in the mid region of potentials. In the final potential range, the m-LNMO shows a limited rock-salt formation represented by a lower resistance value compared to the b-LNMO. In addition, R_{Ct} and R_{CEI} of the m-LNMO electrode display resistance values one order of magnitude lower than the b-LNMO[29,60–62].

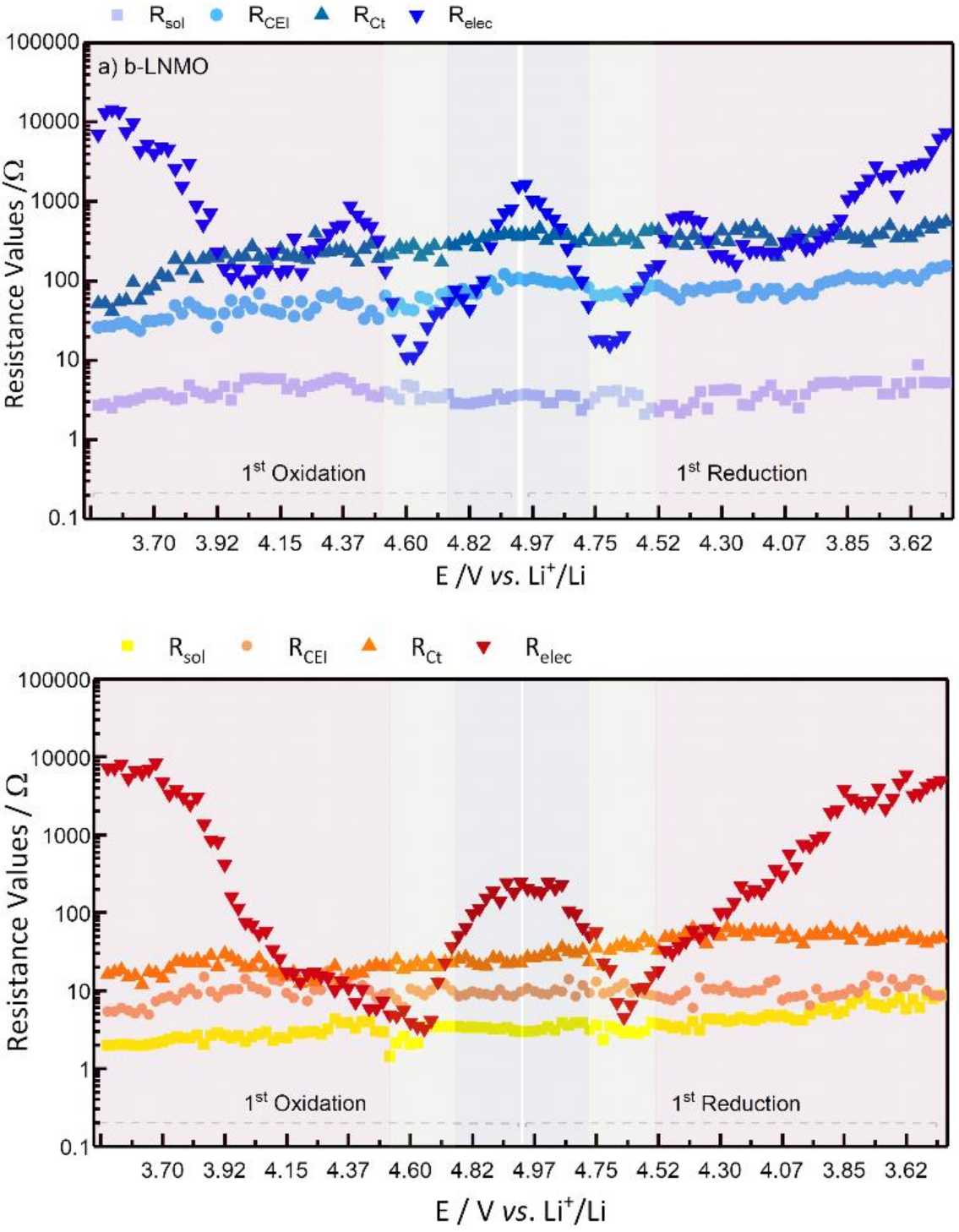

Fig. 3.16 Comparison of fitted parameters for b-LNMO (blue) and m-LNMO (red)

3.3 Conclusions

Summarizing, this study highlights the combined effect of Mg and Zr as an effective and functional modification strategy for enhancing the cycle life of spinel cathode materials, demonstrating significant improvements in capacity retention. Additionally, the suppression or

limitation of harmful phase transitions emerges as a promising approach for achieving excellent high-rate performance in LNMO cathodes.

References

1. Liu, J. & Manthiram, A. Kinetics Study of the 5 V Spinel Cathode LiMn[sub 1.5]Ni[sub 0.5]O[sub 4] Before and After Surface Modifications. *J Electrochem Soc* 156, A833 (2009).
2. Xu, X. L., Deng, S. X., Wang, H., Liu, J. B. & Yan, H. Research progress in improving the cycling stability of high-voltage LiNi0.5Mn1.5O4 cathode in lithium-ion battery. *Nanomicro Lett* 9, (2017).
3. Zhou, S. & Mei, T. materials rate performance for lithium-ion batteries. *J Mater Sci* (2018) doi:10.1007/s10853-018-2272-x.
4. Amdouni, N., Zaghib, K., Gendron, F., Mauger, A. & Julien, C. M. Structure and insertion properties of disordered and ordered LiNi 0.5Mn1.5O4 spinels prepared by wet chemistry. *Ionics (Kiel)* 12, 117–126 (2006).
5. Hu, M., Pang, X. & Zhou, Z. Review Recent progress in high-voltage lithium ion batteries. *J Power Sources* 237, 229–242 (2013).
6. Zhu, X. *et al.* High-Voltage Spinel Cathode Materials: Navigating the Structural Evolution for Lithium-Ion Batteries. *Advanced Materials* vol. 36 Preprint at https://doi.org/10.1002/adma.202403482 (2024).
7. Asres, N. E. *et al.* Investigating structural properties and reaction mechanism of non-stoichiometric spinel LNMO via solid state NMR. *J Mater Chem A Mater* 11, 25612–25625 (2023).
8. Sun, P., Ma, Y., Zhai, T. & Li, H. High performance LiNi0.5Mn1.5O4 cathode by Al-coating and Al3+-doping through a physical vapor deposition method. *Electrochimica Acta* vol. 191 237–246 Preprint at https://doi.org/10.1016/j.electacta.2016.01.087 (2016).
9. Schroeder, M. *et al.* Post-doping via spray-drying: A novel sol-gel process for the batch synthesis of doped LiNi0.5Mn1.5O4 spinel material. *J Mater Sci* 48, 3404–3414 (2013).
10. Deng, Y. F., Zhao, S. X., Xu, Y. H., Gao, K. & Nan, C. W. Impact of P-Doped in Spinel LiNi0.5Mn1.5O4 on Degree of Disorder, Grain Morphology, and Electrochemical Performance. *Chemistry of Materials* 27, 7734–7742 (2015).
11. Ji, Y. *et al.* Improved capacity retention and ultralong cycle performance of Ni-Fe co-doped LiMn2O4 cathode material at high current densities. *Colloids Surf A Physicochem Eng Asp* 648, (2022).
12. Liu, J. & Manthiram, A. Understanding the improvement in the electrochemical properties of surface modified 5 V LiMn 1.42Ni 0.42Co 0.16O 4 spinel cathodes in lithium-ion cells. *Chemistry of Materials* 21, 1695–1707 (2009).

13. Kosova, N. V., Bobrikov, I. A., Podgornova, O. A., Balagurov, A. M. & Gutakovskii, A. K. Peculiarities of structure, morphology, and electrochemistry of the doped 5-V spinel cathode materials LiNi0.5-xMn1.5-yMx+yO4 (M = Co, Cr, Ti; x+y = 0.05) prepared by mechanochemical way. *Journal of Solid State Electrochemistry* 20, 235–246 (2016).
14. Wang, Y. *et al.* Mg/Fe site-specific dual-doping to boost the performance of cobalt-free nickle-rich layered oxide cathode for high-energy lithium-ion batteries. *Journal of Energy Chemistry* 91, 670–679 (2024).
15. Liu, M. H., Huang, H. T., Lin, C. M., Chen, J. M. & Liao, S. C. Mg gradient-doped LiNi0.5Mn1.5O4 as the cathode material for Li-ion batteries. *Electrochim Acta* 120, 133–139 (2014).
16. Yoon, J., Jeong, M., Bae, I. T., Nam, K. W. & Yoon, W. S. Zr-doping effect on the capacity retention of LiNi0.5Mn1.5O4–Δ cycled between 5.0 and 1.0 V: In situ synchrotron X-Ray diffraction study. *J Power Sources* 368, 1–10 (2017).
17. Zhai, Y. *et al.* The Synergic Effects of Zr Doping and Li 2 TiO 3 Coating on the Crystal Structure and Electrochemical Performances of Li-Rich Li 1.2 Ni 0.2 Mn 0.6 O 2 . *J Electrochem Soc* 166, A1323–A1329 (2019).
18. Wei, A. *et al.* Effect of Mg2+/F− co-doping on electrochemical performance of LiNi0.5Mn1.5O4 for 5 V lithium-ion batteries. *Electrochim Acta* 323, (2019).
19. Xiao, Z. H., Cui, Q. Q., Li, X. L., Wang, H. L. & Zhou, Q. Ionothermal synthesis for Mg-doped LiMn1.5Ni0.5O4 spinel with structural stability and high-rate performance. *Ionics (Kiel)* 21, 1261–1267 (2015).
20. Kim, W. K. *et al.* Effects of Cl doping on the structural and electrochemical properties of high voltage LiMn1.5Ni0.5O4 cathode materials for Li-ion batteries. *J Alloys Compd* 592, 48–52 (2014).
21. Liu, J. *et al.* Improving the electrochemical performance of single crystal LiNi0.5Mn1.5O4 cathode materials by Y–Ti doping and unannealing process. *Ceram Int* 48, 36490–36499 (2022).
22. Yi, T. F., Mei, J. & Zhu, Y. R. Key strategies for enhancing the cycling stability and rate capacity of LiNi0.5Mn1.5O4 as high-voltage cathode materials for high power lithium-ion batteries. *J Power Sources* 316, 85–105 (2016).
23. Liu, D. *et al.* Spinel materials for high-voltage cathodes in Li-ion batteries. *RSC Advances* vol. 4 154–167 Preprint at https://doi.org/10.1039/c3ra45706k (2014).
24. He, Y. *et al.* An improved solid-state method for synthesizing LiNi0.5Mn1.5O4 cathode material for lithium ion batteries. *Journal of Alloys and Compounds* vol. 715 304–310 Preprint at https://doi.org/10.1016/j.jallcom.2017.04.293 (2017).
25. Ulu Okudur, F. *et al.* LiNi0.5Mn1.5O4-δ (LNMO) as Co-free cathode for lithium ion batteries via

solution-gel synthesis: Particle size and morphology investigation. *J Alloys Compd* 892, (2022).

26. Nelson, A. J., Reynolds, J. G. & Roos, J. W. Core-level satellites and outer core-level multiplet splitting in Mn model compounds. *Journal of Vacuum Science & Technology A: Vacuum, Surfaces, and Films* 18, 1072–1076 (2000).
27. Fu, Z., Hu, J., Hu, W., Yang, S. & Luo, Y. Quantitative analysis of Ni 2+ /Ni 3+ in Li[Ni x Mn y Co z]O 2 cathode materials: Non-linear least-squares fitting of XPS spectra. *Appl Surf Sci* 441, 1048–1056 (2018).
28. Deng, Y. F., Zhao, S. X., Xu, Y. H. & Nan, C. W. Effect of temperature of Li2O-Al2O3-TiO2-P2O5 solid-state electrolyte coating process on the performance of LiNi0.5Mn1.5O4 cathode materials. *J Power Sources* 296, 261–267 (2015).
29. Wang, L., Li, H., Huang, X. & Baudrin, E. A comparative study of Fd-3m and P4332 'liNi 0.5Mn1.5O4'. *Solid State Ion* 193, 32–38 (2011).
30. Hwang, B. J., Wu, Y. W., Venkateswarlu, M., Cheng, M. Y. & Santhanam, R. Influence of synthesis conditions on electrochemical properties of high-voltage Li1.02Ni0.5Mn1.5O4 spinel cathode material. *J Power Sources* 193, 828–833 (2009).
31. 1-s2.0-S138824819900123X-main.
32. Seyyedhosseinzadeh, H., Mahboubi, F. & Azadmehr, A. Electrochimica Acta Diffusion mechanism of lithium ions in LiNi 0 . 5 Mn 1 . 5 O 4. 108, 867–875 (2013).
33. Ganas, G. *et al.* Synthesis and characterization of LNMO cathode materials for lithium-ion batteries. *Mater Today Proc* 5, 27416–27424 (2018).
34. Jung, R., Metzger, M., Maglia, F., Stinner, C. & Gasteiger, H. A. Oxygen Release and Its Effect on the Cycling Stability of LiNi x Mn y Co z O 2 (NMC) Cathode Materials for Li-Ion Batteries . *J Electrochem Soc* 164, A1361–A1377 (2017).

Chapter 4

4.1 Al-waste recycled MOF as sacrificial template for designing a carbonaceous material for supercapacitors and Na-ion batteries.

The overconsumption of fossil fuels has led to undeniable environmental changes, making the ecological transition an urgent necessity rather than a choice. Consequently, recent years have witnessed a surging demand for cost-effective, high-performance, and environmentally friendly energy storage systems. Among the promising candidates for these systems, carbonaceous materials have emerged as significant materials for Electrostatic Double Layer Capacitors (EDLCs)[63,64]. In EDLCs the storage of electrical energy occurs by electrostatic interaction at the electrode-electrolyte interace, without any faradaic reaction. This prominence is attributed to their exceptional properties, including a large specific surface area that enables efficient effective charge storage. Additionally, carbon-based materials exhibit outstanding chemical and thermal stability, ensuring long-term durability and performance in battery applications.

However, achieving precise control over the 3D architecture of these materials remains a considerable challenge. Direct pyrolysis techniques without further treatment often result in reduced porosity and poor particle size control, ultimately hindering electrochemical performance. To address these challenges, Metal-Organic Frameworks (MOFs) have garnered significant attention. MOFs are highly porous coordination materials composed of transition metal (TM) nodes and organic bridging linkers. Depending on their composition, MOFs can form a wide range of morphologies—including polyhedral, tubular, and rod-like structures—with sizes ranging from the nanoscale to the microscale. Their customizable structures, tunable pore sizes, and adaptable compositions make MOFs ideal precursors for energy storage applications[65–67].

Moreover, utilizing waste materials for MOF synthesis offers a sustainable and cost-effective alternative to traditional production methods[68]. This approach aligns with waste valorization strategies, promoting the beneficial reuse of industrial by-products and reducing environmental impact. Researchers have explored various waste-derived MOF components, both organic and inorganic. For instance, Vellingiri et al[69]. successfully recycled rare earth elements from spent alkaline batteries to synthesize Zn-MOFs with comparable properties to those produced using commercial zinc sources. This study demonstrated that recycling not only reduces costs but also mitigates environmental pollution associated with producing new metal precursors.

Nevertheless, beyond morphology, the formation of a stable and thin solid-electrolyte

interphase (SEI) is critical for the effective operation of Na-ion batteries. The electrolyte plays a vital role in forming an SEI with high ionic conductivity and long-term stability. Therefore, optimizing both the material's structure and the electrolyte composition is essential to achieving durable and high-performance batteries[70].

In this chapter. a sustainable synthesis of a green and porous Al-MOF using waste alumina derived from fly ash is reported. This material was further transformed into a MOF-derived carbonaceous material (c-MOF) exhibiting high adaptability and efficiency in supercapacitors and Na-ion battery applications (see Fig. 4.1). Additionally, the impact of various electrolytes on interfacial properties, including charge transfer, ionic conductivity, and stability has been explored. To gain deeper insights into these properties, Electrochemical Impedance Spectroscopy (EIS) was employed and thoroughly analyzed, providing a comprehensive understanding of the material's electrochemical behavior.

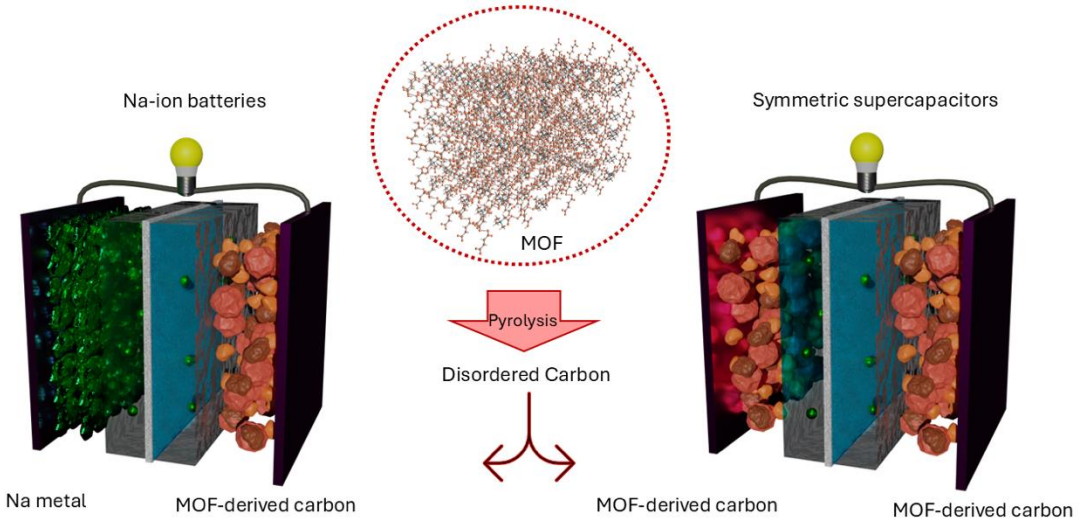

Fig. 4.1 Schematic representation of using MOF derived carbon for symmetric supercapacitors and NIBs.

4.1 Experimental

4.1.1 Synthetic methodology

Hydrothermal conversion of Coal Flying Ashes (CFA) on a semi-technical scale for zeolite synthesis into post-reaction solution

The waste material used to synthetize Al-MOF precursors was fly ashes (FA) retrieved from Kozienice Power Plant, Kozienice, Poland. Briefly, 100 mg of FA was leached by mechanical ball-milling approach and merged with 200 mL of 98% H_2SO_4. The mixture was mechanically blended and heated at 230 ◦C with stirring for 72 hours. To get rid of H_2SO_4, the evaporation step

was applied. The evaporated mixture was mixed and stirred with distilled water (1FA: 6 H_2O) w/vol followed by filtration treatment. Afterwards, 6.45 g of organic linker in the form of fumaric acid and 4.75 g of solid sodium hydroxide were merged with 95.5 mL of deionized water, following the hydrothermal conversion approach which lasted 48 h at a temperature of 60 °C in a Teflon stainless steel reaction tank. To get carbon from Al-MOF precursors (c-MOF), the Al-MOF was annealed at 700 °C for 1 h in argon atmosphere with a heating rate of 5 °C min-1, respectively. In order to remove Al element, the carbonization product was thoroughly immersed in HCl (10%) via a hydrothermal reaction at 80 °C for 2 days, followed by further rinsing procedure with deionised water until the filtrate became neutral.

4.1.2 Chemical, structural, and morphological characterization

The graphitization degree of carbon materials has been investigated by Raman spectroscopy (Horiba IHR 320, wavelength 532 nm) and X-ray diffraction (XRD) (Bragg–Brentano geometry, Cu-Kα, λ = 1.54059Å). The structural morphology and the elemental composition of the carbon material was studied by Field Emission Scanning Electron Microscopy (FE-SEM) and Energy Dispersive X-Ray Analysis (EDX). The study of the pore structure has been completed by nitrogen adsorption-desorption isotherm with a Micrometrics ASAP 2020 analyser on a sample preliminarily outgassed for 12h at 200 °C. The determination of the surface area was accomplished by the linear plot in the relative pressure scale.

4.1.3 Electrode preparation and electrochemical characterization

The electrode was prepared by a standardized process composed by the mixing of the c-MOF with carbon SuperC-65 and Polyvinylidene fluoride (PVDF) (Sigma Aldrich) as binder in the ratio of 80:10:10, in N-Methyl Pyrrolidone. After homogeneous dispersion was reached, the slurry was coated on Al foil for NIBs using a doctor blade. Subsequently, the layer has been dried at room temperature (r.t.) overnight, the electrodes were cut and pressed followed by vacuum drying process in a BUCHI Glass Oven Drying at 120°C for 4h. The c-MOF-based electrodes were investigated in T-shape polypropylene Swagelok-type 3 cells configuration using Na metal chips as counter and reference electrodes. The cells preparation has been completed in an argon-filled glove box (Jacomex GP-campus, oxygen, and moisture content less than 0.8 ppm). 2 electrolytes have been used. In detail 1M $NaPF_6$ in 1:1 EC/PC and 1M $NaPF_6$ + FEC in 1:1 EC/PC for sodium, respectively. In both cases Whatman GF/A glass fiber separator has been used. The electrochemical tests have been carried out by a VMP-3 multichannel electrochemical workstation (Bio-Logic, France). The rate performance of the electrodes have been investigated at different current density from 0.1 to 10 A/g range (6 cycle at every current density), and the recovery of the battery has been assessed at 0.1 A/g. To complete the electrochemical characterization, Potentiostatic

Electrochemical Impedance Spectroscopy (PEIS) was performed each 10^{th} cycle at E=0.5V bias potential, with 10mV of AC amplitude, in the 10mHZ<f<100kHz frequency scale.

To prepare the slurry for the fabrication of EDLCs electrodes, Polyvinylidene fluoride (PVDF) binder was dissolved in N-methyl pyrrolidone (NMP), both sourced from Sigma-Aldrich, to form a uniform slurry. This mixture was evenly coated onto a nickel foam current collector and subsequently heated at 70 °C for 2 hours, followed by drying at room temperature. Once dried, the electrode was compressed using a rolling press to enhance contact and structural integrity.

The electrochemical performance of the electrode was evaluated using a standard three-electrode system in a 6.0 M KOH aqueous solution with a SP-240 electrochemical workstation (Bio-Logic, France). A platinum foil served as the counter electrode, while an Ag/AgCl electrode was used as the reference. Cyclic voltammetry (CV) was conducted in the potential range of –1.2 V to 0 V vs. SCE at various scan rates (2, 5, 25, 50, 100 and 200 mV/s). Galvanostatic charge/discharge tests were performed across different current densities within the same potential window to assess charge storage behavior. Long-term cycling stability was examined at a current density of 10 A/g for over 36,000 cycles. Additionally, electrochemical impedance spectroscopy (EIS) was carried out in the frequency range of 10 mHz to 100 kHz with an AC amplitude of 10 mV under open-circuit voltage (OCV) conditions to analyse charge transfer and ionic diffusion properties. In addition, 2 electrodes made of c-MOF were tested in symmetric cell configuration to evaluate the practical application, the electrochemical test were conducted with the same procedure described above.

4.2 Result and discussion

4.2.1 Structural characterization

Morphological and structural characterization was carried out for both the c-MOF and its precursor. Scanning Electron Microscopy (SEM) was utilized to reveal the superficial features of the materials. SEM images (Fig. 4.2d) provide an insight on the c-MOF material, showcasing micrometric agglomerations of nanoparticles in the range up to 50 nm.

Energy Dispersive X-ray (EDX) spectroscopy images were used to examine the elemental distribution. The EDX analysis confirmed the successful removal of all metal impurities from the precursor, ensuring a cleaner composition in the final material.

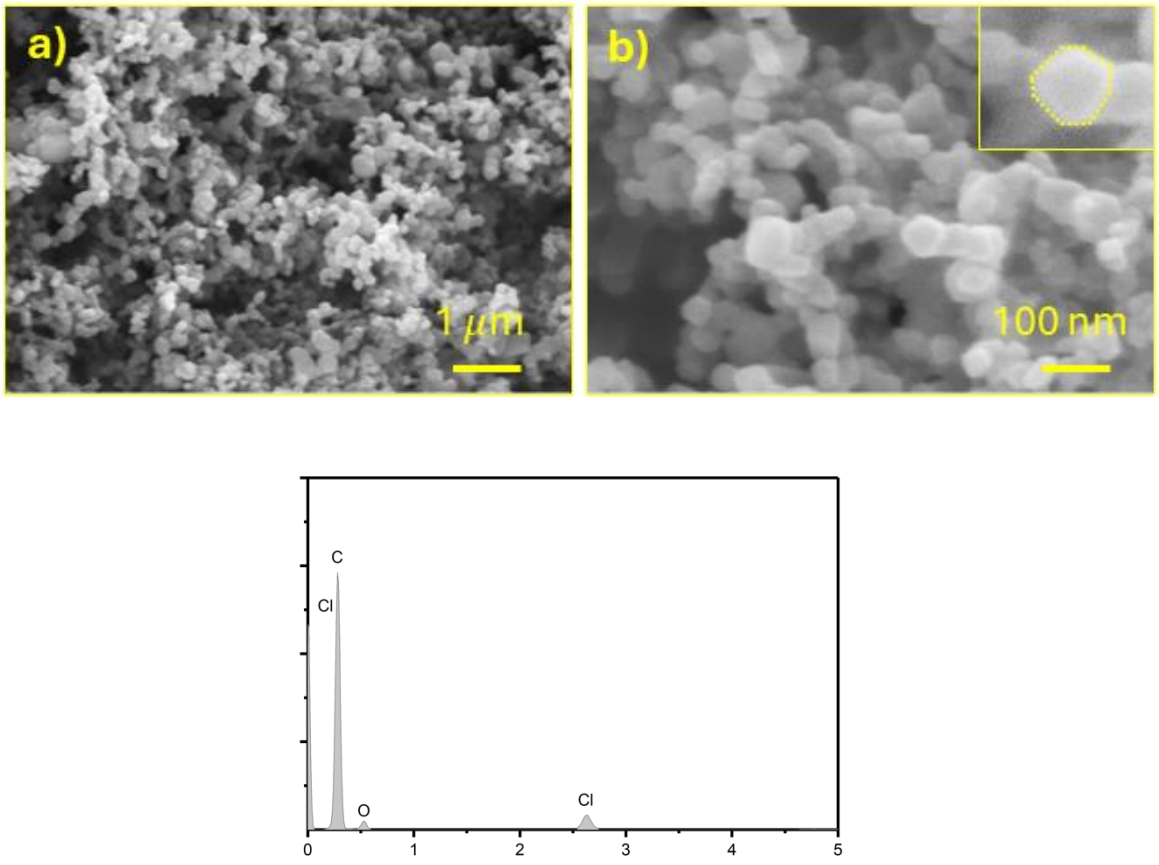

Fig. 4.2 SEM c-MOF after acid leaching with relative EDX

To investigate structural crystallinity and possible impurities, X-ray Diffraction (XRD) analysis was performed. The XRD pattern (Fig. 4.3a) reveals a broad peak and a sharp peak. The broad peak corresponds to the amorphous structure of the carbon material[71,72].

Raman spectroscopy was employed for assessing crystalline ordering and defect density. The Raman spectra (Fig. 4.3b) reveal several characteristic bands: the D band, attributed to breathing modes of sp^2 carbons and structural defects; the G band, associated with the stretching vibrations of sp^2 carbons; the D* band, related to sp^2-sp^3 transitions; and the D** and D' bands, linked to resonance feedback from heteroatomic moieties and graphene structure vibrations, respectively. The D band is observed at 1314.39 cm^{-1}, and the G band at 1578.56 cm^{-1}, with an I_D/I_G ratio of approximately 1.52. This high ratio indicates the amorphous nature of the carbon and a high defect density, which is advantageous for electrochemical storage system[72–75]s.

To further evaluate the structural properties, Brunauer-Emmett-Teller (BET) and Barrett-Joyner-Halenda (BJH) analyses were conducted to estimate the surface area and pore diameter. The BET results (Fig. 4.3c) reveal a type IV nitrogen adsorption-desorption isotherm with a hysteresis loop between 0.4 and 1 P/P_0, indicating the presence of micro- and mesoporosity. The material exhibits a high surface area of 992.74 m^2/g. Additionally, the BJH analysis (Fig. 4.2f) determines

an average pore diameter of 3.5 nm, which is advantageous for electrochemical storage applications[74,76].

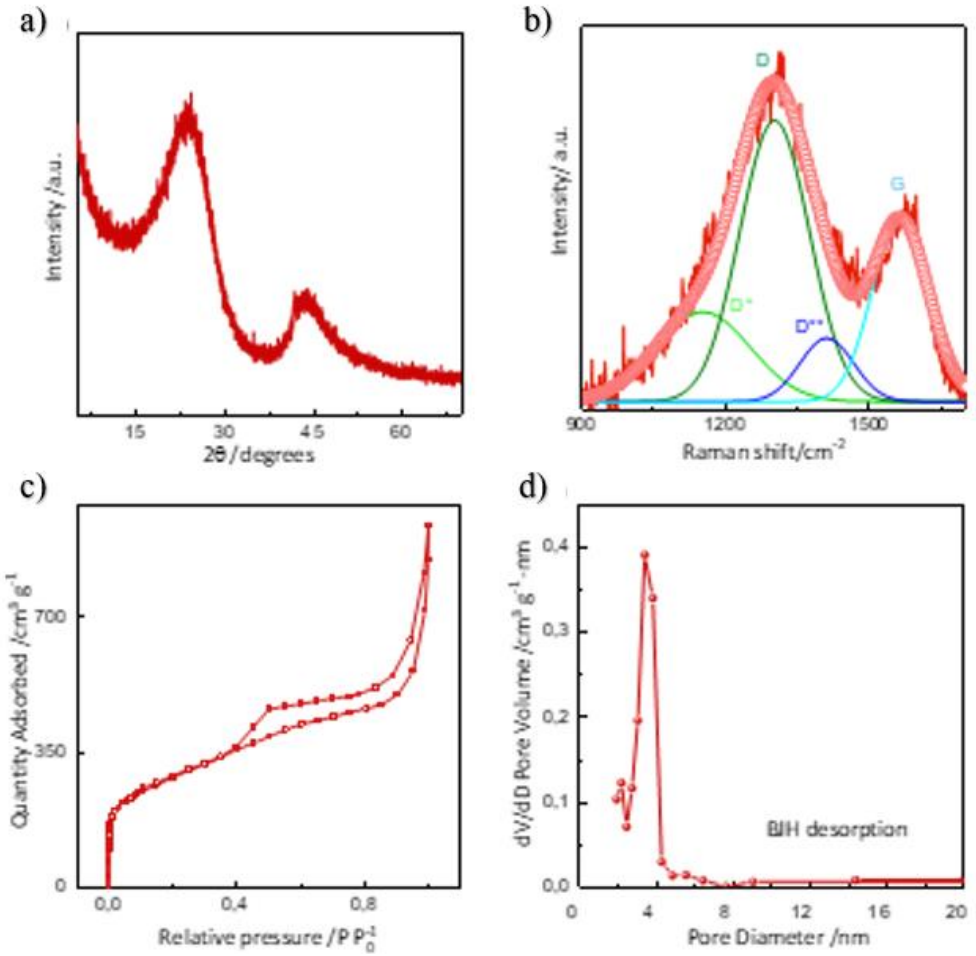

Fig. 4.3 (a) XRD pattern, (b) Raman spectra, (c) BET analysis and (d) BJH desorption analysis

4.2.2 Electrochemical characterization

The electrochemical characteristics of c-MOF electrodes were assessed using cyclic voltammetry (CV) and galvanostatic charge-discharge (GCD) tests, as depicted in Fig. 4.4. The quasi-rectangular CV curves devoid of redox peaks for all the current densities (Fig. 4.4a) and corroborate the electric double-layer capacitance behaviour of c-MOF electrodes. The figure clearly illustrates the reversible reactions taking place at the electrode/electrolyte interface, indicating that energy storage in the EDLC is predominantly driven by the accumulation of ions on the electrode surface[65,66,77]. The high-power density of an ideal supercapacitor is attributed to its low internal resistance. As shown in Fig. 4.4b, the c-MOF based electrode exhibits no evidence of IR drop, even at high current densities. All the charge curves are symmetric to their corresponding discharge curves in the GCD tests, indicating the c-MOF based electrodes exhibit excellent coulombic efficiency and superior capacitive performance. In Fig 4.4c the specific capacitance of c-MOF at

different current densities are reported. The specific capacitance values achieved are 241, 230, 220.1, 185.4, 168.6, 150.4 and 135.4 Fg^{-1} for 1, 2, 3, 6, 10, 12 and 15 Ag^{-1}, respectively.

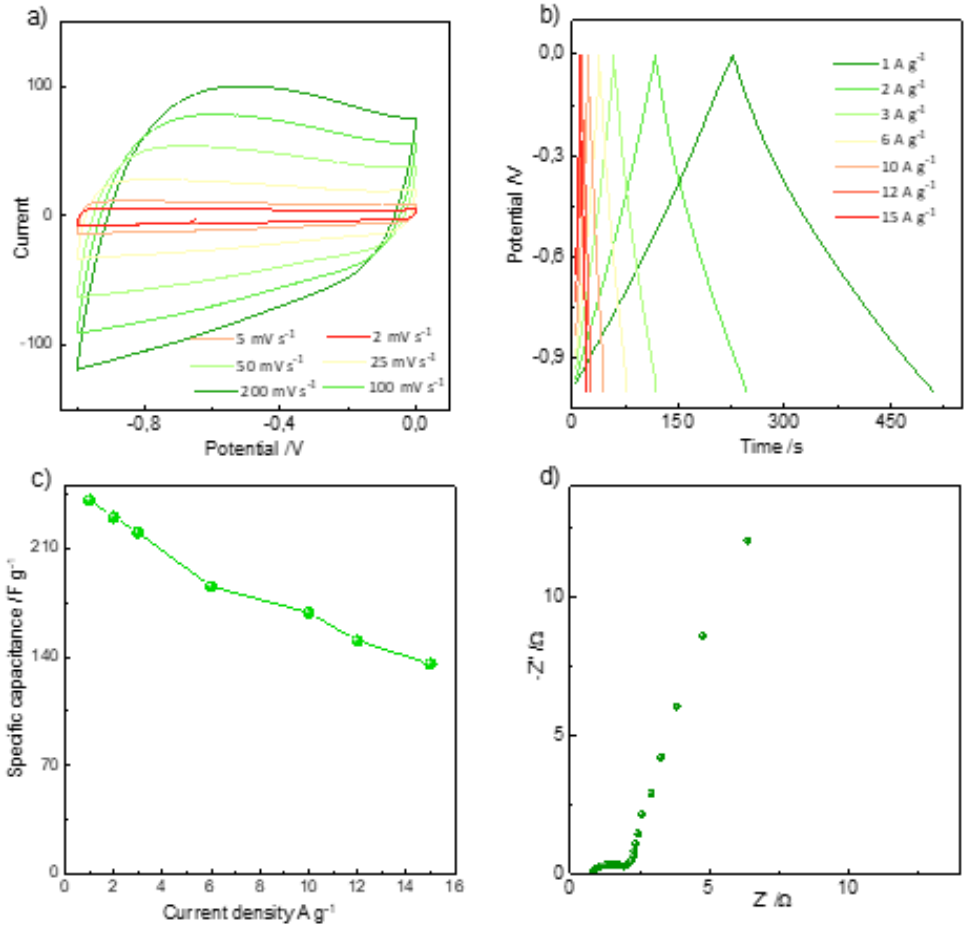

Fig. 4.4 Supercapacitor tests, (a) CV at different scan rates, (b) Galvanocyclic charge discharge, (c) Specific capacitance and (d) Nyquist plot

To elucidate the charge storage kinetics and electrolyte ion diffusion properties, EIS measurements were performed over a frequency range of 10 mHz to 100 kHz with an AC amplitude of 10 mV. The Nyquist plot (Fig. 4.34) reveals two distinct regions: a low-frequency straight line (W), representing ion diffusion limitations, and a high-frequency semicircle, corresponding to the charge-transfer resistance (Rct). The intercept of the semicircle on the Z' axis at high frequency reflects the bulk resistance of the electrolyte solution (Rs). The semicircle diameter indicates an Rct value below 0.35 Ω, suggesting minimal charge-transfer resistance. The semicircle's shape implies the presence of heteroatoms, which could exhibit surface redox activity with electrolyte ions. The low Rct and Rs values are consistent with other reported findings, confirming the material's low internal resistance, superior ionic conductivity, and efficient adsorption-desorption kinetics. Additionally, the steep slope of the low-frequency region indicates that the electric double layers are easily and rapidly established[78–80].

Long cycle life is essential for high-performance electrochemical capacitors. As shown in Fig. 4.5, the C-MOF electrode demonstrates exceptional cyclic stability at a current density of 10 A/g, retaining 91% of its initial capacitance after more than 36,000 cycles, with a coulombic efficiency of 99.7%. This remarkable capacity retention can be attributed to the material's well-structured microporosity, which provides efficient ion diffusion pathways, enabling rapid electrolyte ion transport and the swift formation of stable electric double layers.

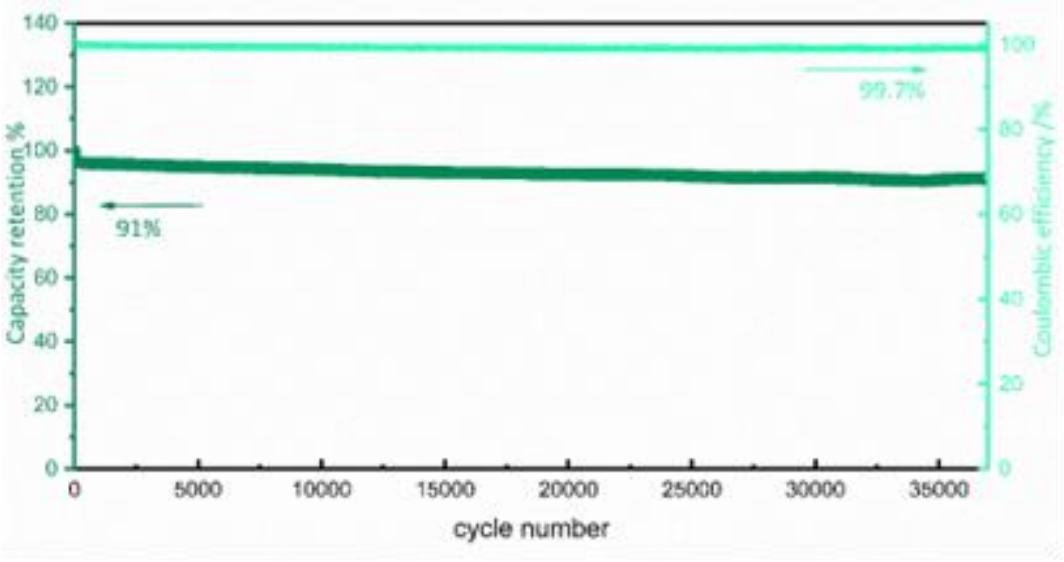

Fig. 4.5 Long cycling performance

To evaluate the suitability of c-MOF for supercapacitor applications, a symmetric cell test was performed. As shown in Fig. 4.6a, the cyclic voltammetry (CV) curves recorded across various voltage ranges exhibit a quasi-rectangular shape, characteristic of electric double-layer capacitor (EDLC) behaviour, indicating non-faradaic processes and efficient charge/discharge capability. However, at a higher cut-off potential of 1.4 V, notable polarization is observed, leading to minor electrolyte decomposition from the second cycle onward. To mitigate this effect and ensure long-term stability, subsequent tests were standardized at 1.2 V[78,81].

The galvanostatic charge/discharge (GCD) curves presented in Fig. 4.6b display a nearly symmetric triangular shape with minimal internal resistance (IR) drop, further confirming the EDLC characteristics of the c-MOF electrode. Long-term cycling performance, shown in Fig. 4.6c, reveals outstanding capacity retention of 92.24% after 5,000 cycles, highlighting the material's durability and stability for practical supercapacitor applications.

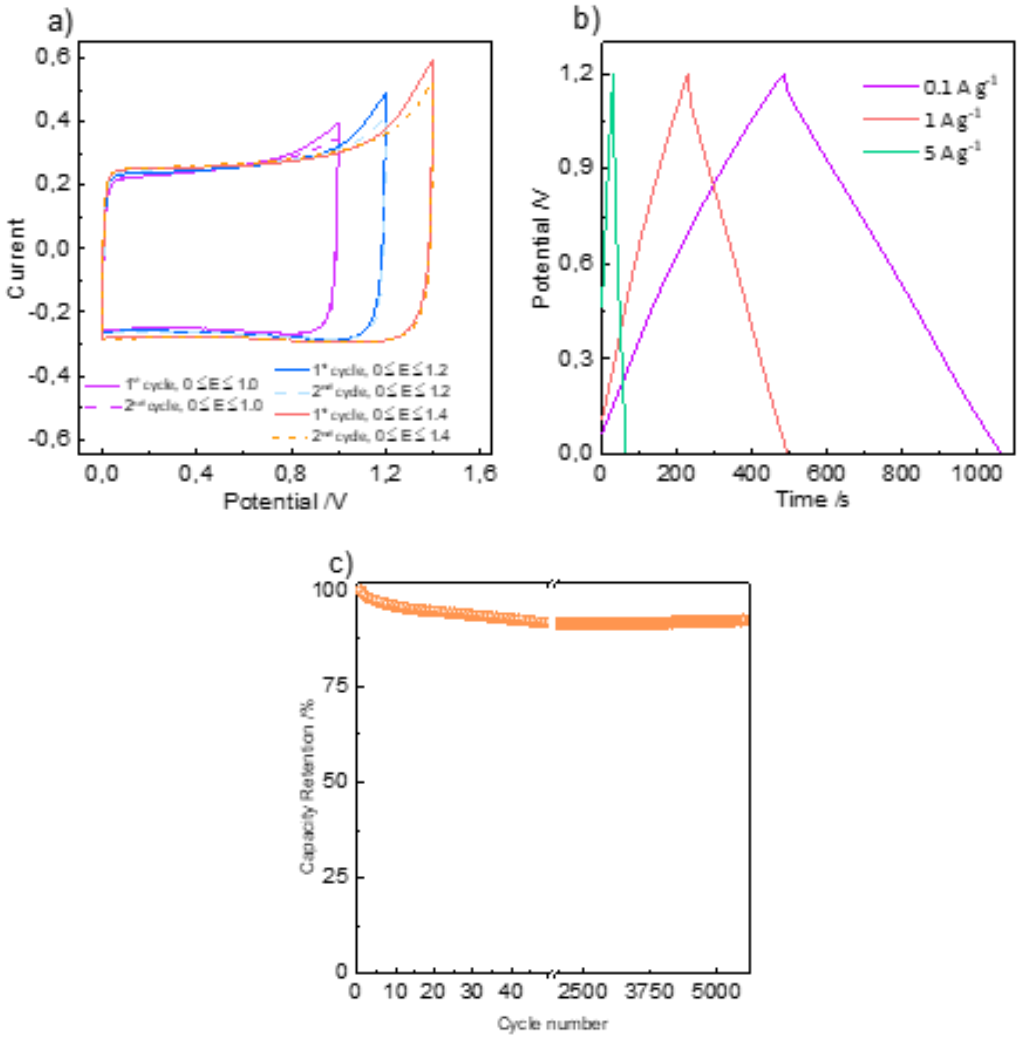

Fig. 4.6 Symmetric Cell test on c-MOF

The electrochemical performance of the c-MOF electrode was systematically evaluated using two electrolyte systems: $NaPF_6$ and $NaPF_6$ supplemented with fluoroethylene carbonate (FEC) as an additive. The C-rate capabilities were assessed through galvanostatic charge-discharge (GCD) tests across a range of current densities from 0.5 A/g to 10 A/g and subsequently back to 0.1 A/g, within a voltage window of 0.01–3 V vs. Na^+/Na (Fig. 4.7)[70,76,79].

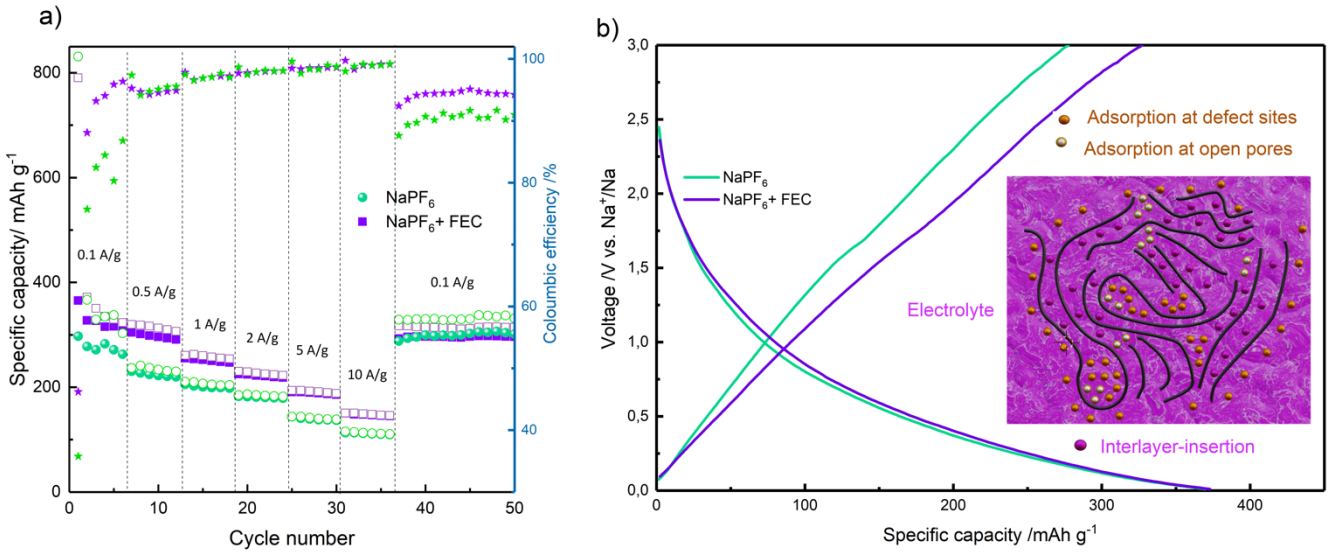

Fig. 4.7 Rate performance (a) and Voltage profile (b) for c-MOF with different electrolytes

Using $NaPF_6$ as the electrolyte, the electrode initially exhibited a high discharge capacity of 830.9 mAh g^{-1} with a coulombic efficiency (CE) of approximately 35.7% at 0.1 A/g. The significant irreversible capacity loss during the first cycle is attributed to the large specific surface area of the c-MOF, which accelerates electrolyte decomposition and the formation of the solid electrolyte interphase (SEI) layer. By the second cycle at 0.1 A/g, the discharge capacity stabilized at 366.8 mAh g^{-1} with an improved CE of 75.7%. At a higher current density of 10 A/g, the electrode maintained a reversible capacity of 115.4 mAh g^{-1} with a CE of 98.0%. However, the CE remained lower at 0.1 A/g compared to higher current rates, likely due to the sluggish kinetics of electrolyte decomposition at low current densities caused by the electrode's high surface reactivity[70,82].

In comparison, the introduction of FEC to the $NaPF_6$ electrolyte significantly enhanced the electrode's performance. The initial discharge capacity at 0.1 A/g was 790.1 mAh g^{-1} with a higher CE of 46.2%. In the second cycle, the capacity slightly increased to 371.6 mAh g^{-1}, and the CE improved markedly to 88.1%. At 10 A/g, the reversible capacity increased to 150.7 mAh g^{-1} with an excellent CE of 99.7%. These results clearly demonstrate that the FEC additive effectively stabilizes the SEI layer and suppresses electrolyte decomposition, leading to enhanced coulombic efficiency and higher reversible capacity, especially under high current densities[70,82,83].

These findings are consistent with our previous work on disordered carbon derived from olive leaves, where similar challenges with initial coulombic efficiency were observed due to the material's structural properties[84]. Given that c-MOF exhibits a higher surface area compared to the carbon material from the cited study, a low initial coulombic efficiency was anticipated. This expectation led to the decision to employ the modified electrolyte with FEC additive to mitigate

surface-related side reactions, promote stable SEI formation, and ultimately enhance the overall electrochemical performance of the electrode.

In Fig. 4.7b, the voltage profiles for the second cycle at 0.1 A/g of the c-MOF electrode with both $NaPF_6$ (green curve) and $NaPF_6$ + FEC (blue curve) electrolytes reveal two distinct features that illustrate the sodium storage mechanism. The prominent high-voltage sloping region from 3 V to 0.1 V is attributed to the physical adsorption of Na^+ ions onto the porous surface and defect sites of the c-MOF structure, facilitated by its high surface area and abundant structural defects, which contribute to the material's capacitive behaviour. Below 0.1 V, a subtle low-voltage plateau emerges, corresponding to the insertion of Na^+ ions into the carbon matrix. This behaviour aligns with the "adsorption-insertion" storage model, where the initial sloping region reflects surface-driven capacitive storage while the low-voltage plateau indicates bulk ion insertion. The presence of FEC in the electrolyte further smoothens and stabilizes the voltage profile, enhancing Na^+ ion transport and promoting the formation of a more stable solid electrolyte interphase (SEI), which ultimately improves cycling stability[82].

To further elucidate the transport behaviours and redox processes Electrochemical Impedance Spectroscopy have been performed. The EIS have been recorded every 10^{th} cycle at =25°C and 0.5 V. Fig.4.8 shows the Nyquist plots for the electrodes assembled with plot $NaPF_6$ (4.8a) and $NaPF_6$+ FEC (4.8b). The spectra display common features, namely in order of decreasing frequencies: (1) an offset to the Y-axis, (2) a 1^{st} semicircle in the high frequency, (3) a 2^{nd} semicircle in the mid-high frequency, (4) a straight vertical line.

Figure 4.8a exhibits an irregular pattern characterized by alternating trends. During the initial 20 cycles, there is a progressive rise in overall resistance. Subsequently, over the subsequent 60 cycles, there is a gradual decline in resistance until reaching a state of stability. In the final segment, there is a rapid surge in resistance, culminating in the 100th cycle where the maximum impedance is attained. The Nyquist plot for $NaPF_6$ + FEC (Fig. 4.8b) shows a completely opposite trend, a progressive decrease of the overall resistance occurs upon cycling, which is highlighted in the inset. These results suggest that the $NaPF_6$ + FEC electrolyte can help the formation of a more stable and thinner SEI, providing a more efficient space region within the electrode surface in which the charge transfers are not hindered by additional interfacial resistance. Meanwhile, the instability of the Nyquist plot for $NaPF_6$ can be ascribed to the formation of an unstable SEI growth upon cycling, which is the main responsible for the raise in the overall resistance[74,85–88].

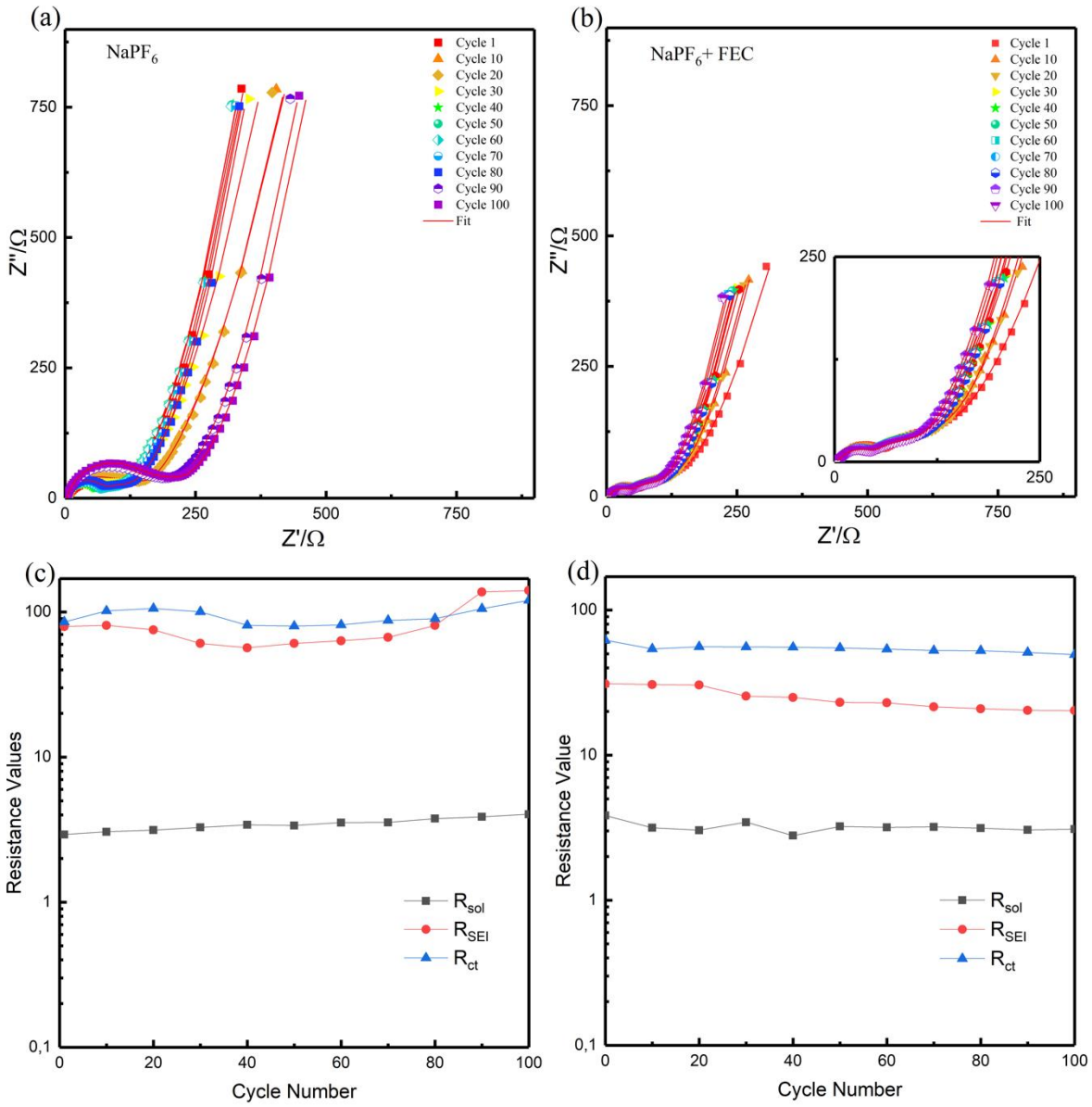

Fig. 4.8 Nyquist plot and fitted parameters for c-MOF for $NaPF_6$ (a, c) and $NaPF_6$ + FEC (b,d)

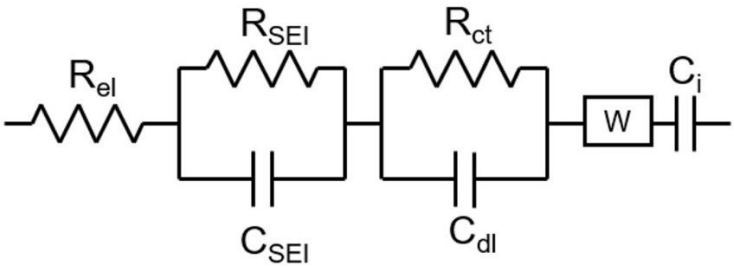

Fig. 4.9 Equivalent Circuit (EC)

The equivalent circuit (EC) shown in Fig. 4.9, which may be written as $R_{sol}(R_{SEI}C)(R_{ct}C)W$ in Boukamp's notation, has been used to simulate the electrochemical process occurring upon charge/discharge and fit all the impedance diagrams. Each part of the EC describes specific

electrochemical processes, namely: (i) Rsol ascribed to the electrolyte resistance; (ii) R_{SEI} and C_{SEI} indicating the resistance and capacitance related to the charge migration/accumulation across the interphase between the electrode and electrolyte;(iii) R_{ct} and C_{dl} related to the electrode/electrolyte interfacial charge-transfer resistance and double-layer capacitance; (v) W representing the Warburg diffusion resistance in the bulk of the electrode. Moreover, to reduce the eventual error due to electrode superficial inhomogeneity all the C elements have been substituted with constant-phase elements Q.

Figs. 4.8c and 4.8d present the fitted electrochemical impedance parameters for the two electrolytes, revealing distinct differences in their performance. By examining and comparing each parameter, it becomes evident that the solution resistance (R_{sol}) exhibits higher values and an increasing trend over cycling for the $NaPF_6$ electrolyte, indicating electrolyte deterioration within the cycling, whereas the $NaPF_6$ + FEC electrolyte maintains a more stable and lower R_{sol}. The solid electrolyte interphase resistance (R_{sei}) shows the most significant improvement with the addition of FEC, as the additive promotes the formation of a more uniform and less resistive SEI layer, thereby stabilizing the interfacial interaction between the electrode and electrolyte. This optimized SEI formation effectively minimizes parasitic reactions and reduces impedance growth over cycling. Similarly, the charge transfer resistance (Rct) mirrors the behavior of R_{sei}, with the $NaPF_6$ + FEC system demonstrating a consistently lower Rct and more stable performance compared to $NaPF_6$ alone. This reduction in Rct further highlights the beneficial impact of FEC in enhancing interfacial processes and allowing faster charge transfer kinetics, thus improving overall electrochemical performance.

This behaviour is reflected also in other studies in which the FEC additive can efficiently form a stable and thin SEI in Fig. 4.10 shows a simulation of the effect of this additive to the SEI compared with the electrode assembled with $NaPF_6$[82].

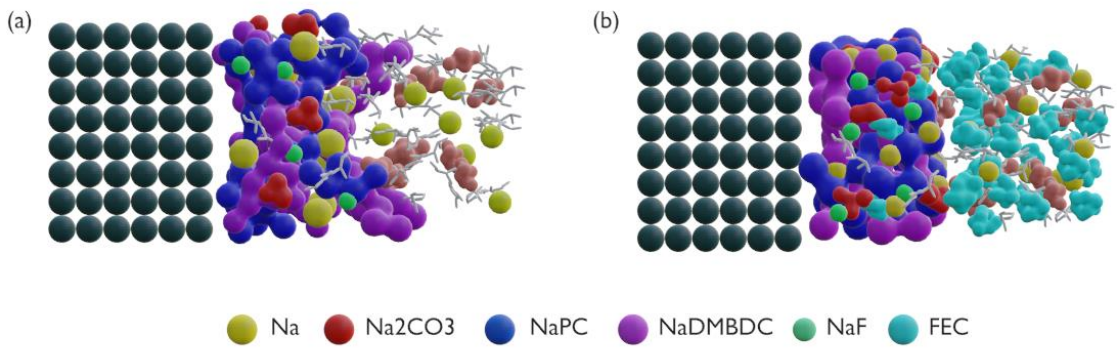

Fig.4.10 Illustration of the additive effects on the SEI formation (a) $NaPF_6$ and (b) $NaPF_6$ +FEC

4.4 Conclusion

In conclusion, a MOF-derived carbonaceous material for supercapacitor and sodium-ion battery (NIB) applications has been explored. Synthesized through the waste valorisation of aluminium waste and engineered as a sacrificial template to achieve a well-defined nanosphere-shaped disordered carbon, this material demonstrated remarkable performance. In supercapacitor applications, both half-cell and symmetric cell configurations exhibited outstanding capacity retention and high operating voltage. For NIBs, the c-MOF displayed excellent rate capability and high capacity, attributed to its absorption-insertion storage mechanism, which is facilitated by the material's exceptionally high surface area.

References

1. Qu, W. H., Xu, Y. Y., Lu, A. H., Zhang, X. Q. & Li, W. C. Converting biowaste corncob residue into high value added porous carbon for supercapacitor electrodes. *Bioresour Technol* 189, 285–291 (2015).
2. Usha Rani, M., Nanaji, K., Rao, T. N. & Deshpande, A. S. Corn husk derived activated carbon with enhanced electrochemical performance for high-voltage supercapacitors. *J Power Sources* 471, (2020).
3. Pokharel, J. *et al.* MOF-derived hierarchical carbon network as an extremely-high-performance supercapacitor electrode. *Electrochim Acta* 394, (2021).
4. Gerbaldi, C. *et al.* Innovative high performing metal organic framework (MOF)-laden nanocomposite polymer electrolytes for all-solid-state lithium batteries. *J Mater Chem A Mater* 2, 9948–9954 (2014).
5. Ren, J. *et al.* Recent progress on MOF-derived carbon materials for energy storage. *Carbon Energy* vol. 2 176–202 Preprint at https://doi.org/10.1002/cey2.44 (2020).
6. El-Sayed, E. S. M. & Yuan, D. Waste to MOFs: Sustainable linker, metal, and solvent sources for value-added MOF synthesis and applications. *Green Chemistry* vol. 22 4082–4104 Preprint at https://doi.org/10.1039/d0gc00353k (2020).
7. Vellingiri, K. *et al.* The utilization of zinc recovered from alkaline battery waste as metal precursor in the synthesis of metal-organic framework. *J Clean Prod* 199, 995–1006 (2018).
8. Cheng, D. *et al.* Electrochemical storage mechanism of sodium in carbon materials: A study from soft carbon to hard carbon. *Carbon N Y* 182, 758–769 (2021).
9. Liang, Y. *et al.* Disordered carbon structures enhance capacitive storage. *Green Carbon* (2024) doi:10.1016/j.greenca.2024.06.004.
10. Putman, K. J. *et al.* Defining graphenic crystallites in disordered carbon: Moving beyond the

platelet model. *Carbon N Y* 209, (2023).

11. Xie, F. *et al.* Disordered carbon anodes for Na-ion batteries—quo vadis? *Science China Chemistry* vol. 64 1679–1692 Preprint at https://doi.org/10.1007/s11426-021-1074-8 (2021).
12. Nepal, K., Ugwumadu, C., Gautam, A., Kappagantula, K. & Drabold, D. A. Electronic conductivity in metal-graphene composites: the role of disordered carbon structures, defects, and impurities. *JPhys Materials* 7, (2024).
13. Liang, Y. *et al.* Disordered carbon structures enhance capacitive storage. *Green Carbon* (2024) doi:10.1016/j.greenca.2024.06.004.
14. Zhao, L. *et al.* Defect Engineering of Disordered Carbon Anodes with Ultra-High Heteroatom Doping Through a Supermolecule-Mediated Strategy for Potassium-Ion Hybrid Capacitors. *Nanomicro Lett* 15, (2023).
15. wu, J. *et al.* Hierarchical porous carbon derived from wood tar using crab as the template: Performance on supercapacitor. *J Power Sources* 455, (2020).
16. Salunkhe, R. R. *et al.* Fabrication of symmetric supercapacitors based on MOF-derived nanoporous carbons. *J Mater Chem A Mater* 2, 19848–19854 (2014).
17. Liu, X. *et al.* Al-MOF-derived spindle-like hierarchical porous activated carbon for advanced supercapacitors. *Dalton Transactions* 51, 2538–2546 (2022).
18. Yu, J. *et al.* High Specific Capacitance Electrode Material for Supercapacitors Based on Resin-Derived Nitrogen-Doped Porous Carbons. *ACS Omega* 4, 15904–15911 (2019).
19. Ciszewski, M., Koszorek, A., Radko, T., Szatkowski, P. & Janas, D. Review of the Selected Carbon-Based Materials for Symmetric Supercapacitor Application. *Journal of Electronic Materials* vol. 48 717–744 Preprint at https://doi.org/10.1007/s11664-018-6811-7 (2019).
20. Bommier, C. & Ji, X. Electrolytes, SEI Formation, and Binders: A Review of Nonelectrode Factors for Sodium-Ion Battery Anodes. *Small* vol. 14 Preprint at https://doi.org/10.1002/smll.201703576 (2018).
21. Liu, M., Niu, J., Zhang, Z., Dou, M. & Wang, F. Potassium compound-assistant synthesis of multi-heteroatom doped ultrathin porous carbon nanosheets for high performance supercapacitors. *Nano Energy* 51, 366–372 (2018).
22. Darjazi, H. *et al.* From waste to resources: transforming olive leaves to hard carbon as sustainable and versatile electrode material for Li/Na-ion batteries and supercapacitors. *Materials Today Sustainability* 21, (2023).
23. Linsenmann, F., Pritzl, D. & Gasteiger, H. A. Comparing the Lithiation and Sodiation of a Hard Carbon Anode Using In Situ Impedance Spectroscopy. *J Electrochem Soc* 168, 010506 (2021).
24. Schutjajew, K. *et al.* Insights into the sodiation mechanism of hard carbon-like materials from

electrochemical impedance spectroscopy. *Physical Chemistry Chemical Physics* 23, 11488–11500 (2021).

25. Chen, X. *et al.* Understanding of the sodium storage mechanism in hard carbon anodes. *Carbon Energy* vol. 4 1133–1150 Preprint at https://doi.org/10.1002/cey2.196 (2022).
26. Sun, N., Qiu, J. & Xu, B. Understanding of Sodium Storage Mechanism in Hard Carbons: Ongoing Development under Debate. *Advanced Energy Materials* vol. 12 Preprint at https://doi.org/10.1002/aenm.202200715 (2022).

Chapter 5

5.1 Fe_2O_3@rGO doped by Mg and Ni as enhanced peroxide scavenger cocatalysts in oxygen reduction reaction

As discussed in the Chapter 1, nowadays the research about Oxygen Reduction Reaction (ORR) catalyst have been shifted to PGM-free catalysts.

Three primary pathways have been proposed to describe the mechanism of the oxygen reduction reaction (ORR) taking place at fuel cell cathodes. The first one is the two-electron partial reduction, which results in the formation of hydrogen peroxide (H_2O_2) or hydroperoxide (HO_2^-) intermediates[89,90]. The second one is the four-electron total reduction pathway, where oxygen is directly converted to water (H_2O) or hydroxide ions (OH^-). Lastly, there is the two-step mechanism, often referred to as the 2+2-electron pathway. This process involves an initial two-electron reduction to form H_2O_2 or HO_2^-, which is then further reduced to H_2O or OH^-, either on the same or a different active site[91,92].

The study of the different reaction pathways is a relevant research topic not only from the pure research point of view, but also in terms of impact toward consumer and industrial applications. In fact, properly understanding and steering the different pathways can selectively address ORR toward water or hydrogen peroxide production. For hydrogen peroxide electrosynthesis, the two-electron pathway is the preferred route. In contrast, the direct four-electron transfer pathway, yielding water, is highly desirable for energy conversion applications in fuel cells, as it offers greater efficiency.

In acidic electrolytes, these mechanisms can be described by specific reactions. The four-

electron pathway is represented by Equation 5.1[90,93,94]:

$$O_2 + 4H^+ + 4e^- \rightleftharpoons 2H_2O \quad (5.1)$$

$$O_2 + 2H^+ + 2e^- \rightleftharpoons H_2O_2 \quad (5.2)$$

$$H_2O_2 + 2H^+ + 2e^- \rightleftharpoons 2\,H_2O \quad (5.3)$$

In alkaline media, where hydroxide ion production is the goal, the favorable mechanism is the four-electron pathway, as described in Equation 5.4[94]:

$$O_2 + H_2O + 4e^- \rightleftharpoons 4\,HO^- \quad (5.4)$$

The two-step and intermediate mechanisms are described by Equations 5.5 and 5.6, respectively[93,94]:

$$O_2 + * + H_2O + 2e^- \rightleftharpoons HOO^- * + HO^- \quad (5.5)$$

$$HOO^- + H_2O + 2e^- \rightleftharpoons 3\,HO^- \quad (5.6)$$

A key challenge in optimizing ORR for fuel cells is overcoming the significant overpotential, which can reach up to 400 mV. This overpotential is a critical factor limiting the performance of ORR electrocatalysts.

Fuel cell electrocatalysts generally fall into three categories: Platinum Group Metal (PGM)-based materials, carbonaceous metal-free materials, and PGM-free materials.

Carbonaceous materials have gathered significant attention due to their high surface area, excellent electrical conductivity, corrosion resistance, and mechanical and thermal stability. Furthermore, these materials benefit from industrial production processes that enable large-scale availability[89,95–97]. However, carbon-based cathodes typically suffer from high overpotential and sluggish reaction kinetics, making them less suitable for fuel cell applications. Purely carbonaceous materials tend to favor the undesired two-electron ORR mechanism unless they contain transition metals, either dispersed or in nanoparticle form.

To address these issues, significant research has focused on PGM-free carbonaceous composites doped with transition metals. These materials have been shown promising in reducing overpotential and enhancing overall catalytic activity. Among them, iron-based electrocatalysts

stand out due to iron abundance and cost-effectiveness. Studies have demonstrated that Fe-based catalysts can rival Pt-based materials, particularly in neutral and alkaline environments[97–99].

Iron oxides, such as Fe_2O_3, have shown considerable potential as ORR electrocatalysts due to their mechanical and thermal stability, as well as their wettability. These oxides can be synthesized using various low-cost, scalable methods, making them attractive for industrial applications. Despite their advantages, commercialization has been limited by issues such as low selectivity and slow reaction kinetics[100–106].

To improve the performance of Fe-based catalysts, this study investigates the impact of doping Fe_2O_3 with magnesium (Mg) and nickel (Ni). The goal is to understand how varying dopant concentrations influence the structural and electrochemical properties of the catalysts. A one-pot solvothermal synthesis method was employed, offering advantages in terms of reproducibility, scalability, and yield. The structural analysis confirmed the incorporation of dopants and their effects on crystal morphology, while electrochemical performance was evaluated using rotating ring-disk electrode (RRDE) voltammetry. This comprehensive approach aims to establish a clear link between dopant composition and catalytic performance, paving the way for more efficient ORR electrocatalysts.

In addition, these catalysts were evaluated as composite materials composed of FePc600 and iron oxide to assess their peroxide scavenging properties. Two different configurations were investigated, featuring FePc600 to iron oxide ratios of 80:20 and 20:80. This comparative analysis aimed to determine the optimal balance between catalytic activity and peroxide decomposition efficiency. By adjusting the ratio of FePc600 to iron oxide, the study sought to enhance the overall oxygen reduction reaction (ORR) performance while minimizing peroxide formation, thereby improving catalyst durability and performance.

5.1 Experimental

5.1.1 Synthetic methodology

All the chemicals have been purchased from Merck and used without any further purification. The synthesis has been carried out following a method previously reported in literature [101]. In detail, 30 mg of Graphene Oxide (GO) in 30 ml of water have been ultrasonicated for 10 minutes. Subsequently, 31.09 mg of $(NH_4)_2Fe(SO_4)_2$ have been added to the suspension and ultrasonicated for a further 10 minutes. Finally, 30 µl of NH_4OH have been added and ultrasonicated for 2h at room temperature. The final dispersion was transferred to a 70 ml autoclave reactor and heated at 150 °C for 15h in an oven. To obtain the final product the suspension was centrifugated and the supernatant solution was removed, the collected powder was then redispersed in distilled water and centrifugated. This procedure was repeated other 2 times, to ensure the complete removal of the base, and then the collected wet powder was dried at 60 °C overnight. The same procedure was applied for the synthesis of the modified catalysts with the addition of different amounts of $MgNO_3$ and $NiNO_3$ at 6%, 12%, 18% Mg/Fe or Ni/Fe mass ratios, respectively, and the addition of a slight excess of the base was added (3/6/9 µl, respectively). All the catalysts are referred to in the following according to their concentration of dopant such as Mg6%, Mg12%, Mg18%, Ni6%, Ni12% and Ni18% (see Fig. 1)**.** In the following manuscript, the electro catalysts will be referred to either by their full nomenclature (e.g., $M_{X\%}Fe_2O_3$@rGO) or by a shortened form (e.g., $M_{X\%}$) for conciseness.

5.1.2 Chemical, structural, and morphological characterization

X-ray diffraction (XRD) and Raman spectroscopy have been used for the determination of the structures and phases present in the samples. Crystalline phases were identified through X-ray diffraction analysis (XRD) using a Panalytical Xpert3 MRD system. The analysis was conducted at room temperature with Cu Kα radiation, operating at a voltage of 40 kV and a current of 40 mA, over a 15–70° 2θ range. The Raman spectroscopy was performed with a Horiba IHR 320 (excitation wavelength 532 nm) from 100 to 3500 cm^{-1}. The Rietveld refinement of the XRD patterns was performed using the FullProf software. To correctly quantify the iron content and the Iron/C ratio, thermogravimetric analysis has been carried out by a Parkin Elmer STA 6000. The

investigation of the morphological features has been carried out with a FE-SEM Cambridge Stereoscan 360 electron microscope operating at 5 kV coupled with energy-dispersive X-ray spectrometer (EDX).

X-ray photoelectron spectroscopy (XPS) analyses were performed using a PHI 5000 Versa Probe instrument from ULVAC-PHI (Physical Electronics Inc., Kanagawa, Japan). The instrument employed monochromatic Al Kα radiation with an energy of 1486.6 eV as the X-ray source. Two different pass energy settings were used: 187.75 eV for the survey spectra and 23.5 eV for the high-resolution (HR) spectra. During the measurements, charge compensation was maintained using a combination of an electron beam and a low-energy Ar beam system.

5.1.3 Ink Preparation

The electrode ink has been prepared by a standardized procedure applied for each sample. In detail, the samples were mixed with KJB in the ratio electro catalysts:KJB 20:80 and ground for 20 minutes to ensure homogenization. After, 5mg of catalyst was dispersed in 985 µl of isopropanol and ultrasonicated for 3 minutes. Subsequently, 15 µl of Nafion was added to the solution and the ink was sonicated for another 20 minutes. Finally, 28.5 µl of the ink was deposited on the surface of the working electrodes with a final (doped)Fe_2O_3@rGO overall loading of 0.6 mg/cm^2.

To assess the effective peroxide scavenging proprieties, a composite material with Iron-Phthalocyanine (FePc600) was created with 2 different ratios $M_xFe_2O_3$@rGO/FePc600, 20:80 and 80:20. The synthesis of FePc600. These inks have been prepared with the same standardized procedure previously discussed[97].

5.1.4 Electrochemical characterization

The electrochemical activity of the synthesized species has been accomplished by Rotating Ring Disk Electrodes (RRDE) with a Pine Research (Durham, NC) cell setup. The electro catalysts were coated on the surface of a rotating-disk glassy carbon working electrode assembled with a Pt ring electrode, Pt wire was used as a counter electrode, and Ag/AgCl (3M KCl, E = 0.197V vs. RHE). The electrodes were immersed in an O_2-saturated 0.1 M KOH solution.

The characterization was conducted using a CHI832 bipotentiostat (CH Instruments, Austin TX) coupled with a Pine model 636 Rotator with a maximum rotating speed of 1600rpm. To investigate the performance of the electro catalyst, Linear Sweep Voltammetry (LSV) has been performed. The scans were carried out at disk potentials ranging from 0.150 V to -1.05 V vs Ag/AgCl, setting the ring potential at 0.150 V and at a scan rate of 5 mVs^{-1}. All the scans were performed at 1600 rpm and at room temperature. All the voltages are reported vs. Reference Hydrogen Electrode (RHE) potential.

5.2 Results and Discussion

5.2.1 Structural characterization

The structural phase and crystallinity of the synthesized materials were analyzed using X-ray diffraction (XRD). Figure 5.1 displays the diffraction patterns for all samples, including Fe_2O_3@rGO, $Mg_{6\%}Fe_2O_3$@rGO, $Mg_{12\%}Fe_2O_3$@rGO, $Mg_{18\%}Fe_2O_3$@rGO, $Ni_{6\%}Fe_2O_3$@rGO, $Ni_{12\%}Fe_2O_3$@rGO, and $Ni_{18\%}Fe_2O_3$@rGO. The observed diffraction peaks correspond to the (012), (104), (110), (113), (024), (116), (018), (214), and (300) planes, characteristic of the rhombohedral α-Fe_2O_3 (hematite) phase, with a space group of R-3c[101,102,107].

The absence of the (001) diffraction peak at 11.01°—typical of graphene oxide (GO)—and the presence of a broad (002) feature at 26.8°, characteristic of reduced graphene oxide (rGO), indicate that the hydrothermal synthesis effectively reduced GO to rGO. This reduction is advantageous as it improves the electron conductivity of the material.

No additional phases were detected in the Mg- and Ni-doped samples (up to Ni12%), suggesting that the doping process primarily affects the internal structure of the α-Fe_2O_3 without introducing new crystalline phases. However, the diffraction pattern of $Ni_{18\%}Fe_2O_3$@rGO displays a notable feature: the presence of maghemite (γ-Fe_2O_3) with a $P4_32_12$ space group. This reveals that higher nickel doping levels, in addition to potentially modify the structure, can lead to the

formation of secondary phases[106,108].

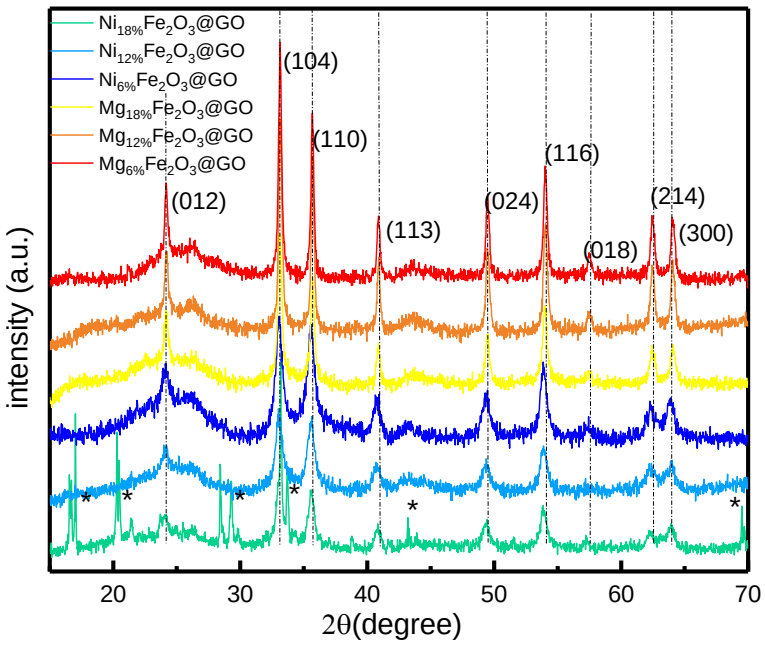

Fig. 5.1 XRD of all samples

To ensure precise structural characterization, Rietveld Refinement of the XRD patterns was performed using the profile matching method in the FullProf Suite. The refinement results, depicted in Fig. 5.2, confirm that all samples retain a rhombohedral hexagonal structure (due to overlapping of diffraction peaks of three different phases – amorphous rGO and crystalline $Ni_{18\%}Fe_2O_3$ and γ-Fe_2O_3, refinement of $Ni_{18\%}Fe_2O_3$ phase has not been possible). Minor variations in lattice parameters were observed, with the doped samples showing slightly smaller lattice parameters and reduced cell volumes compared to the pristine Fe_2O_3@rGO. Notably, the $Ni_{6\%}Fe_2O_3$@rGO sample exhibited the most significant reduction, with a cell volume of 302.1 Å^3, compared to 304.70 Å^3 for the undoped sample[101,102,104,106].

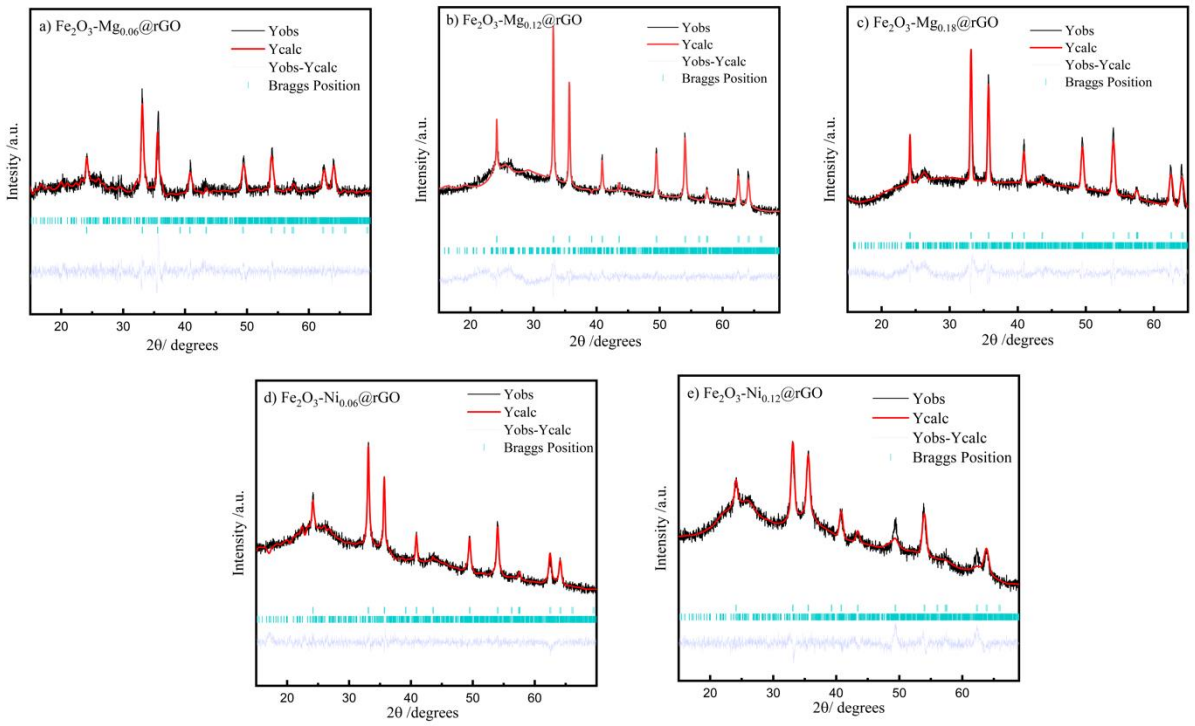

Fig. 5.2 Rietveld analysis for all samples

Table 5.1 Results for the Rietveld Refinement analysis

Catalyst	Lattice parameter (a,b) (Å)	Lattice parameter (c) (Å)	Cell Volume (Å^3)	R_w (%)
Fe_2O_3@rGO	5.09	13.79	304.70	1.89
$Mg_{6\%}Fe_2O_3$@rGO	5.05	13.78	304.66	1.79
$Mg_{12\%}Fe_2O_3$@rGO	5.04	13.78	303.46	2.46
$Mg_{18\%}Fe_2O_3$@rGO	5.05	13.79	304.67	2.84
$Ni_{6\%}Fe_2O_3$@rGO	5.03	13.79	302.10	3.01
$Ni_{12\%}Fe_2O_3$@GO	5.05	13.79	304.42	2.73

This reduction in lattice parameters can be attributed to two factors: (i) distortion of the rhombohedral lattice to accommodate dopant atoms and (ii) charge imbalances in the oxide structure induced by doping, potentially leading to the formation of oxygen vacancies to restore charge neutrality. These structural modifications, particularly the reduced cell volume and the presence of oxygen vacancies, are expected to enhance electron transfer kinetics, improve electron conduction across grain boundaries, and facilitate molecular oxygen transport. Collectively, these

factors could significantly boost the electrocatalytic performance, suggesting that $Ni_{6\%}Fe_2O_3$@rGO may exhibit superior activity among the synthesized catalysts.

In contrast, the $Ni_{18\%}Fe_2O_3$@rGO sample displayed the formation of an additional γ-Fe_2O_3 (maghemite) phase, as already indicated by its XRD pattern. Literature reports suggest that the emergence of secondary phases, often linked to excessive dopant concentrations or specific synthesis conditions, can compromise the efficiency of dopant incorporation into the oxide lattice and hinder catalytic activity[106–108].

The Raman spectra further validate the structural changes and provide insight into the reduction of GO to rGO as well as the extent of nanocomposite formation (Fig. 5.4). Two prominent bands were observed: the D band at 1358 cm^{-1}, corresponding to structural defects (A_1g mode), and the G band at 1597 cm^{-1}, associated with sp^2 carbon domains (E_9g mode). Additionally, Raman peaks characteristic of α-Fe_2O_3 were identified, consistent with pure α-Fe_2O_3 spectra (Fig. 5.3. These peaks include symmetric Fe–O stretching (A_1g modes) at 223 and 493 cm^{-1}, and Fe–O symmetric and asymmetric bending (E_9g modes) at 292, 412, and 604 cm^{-1} [109–113].

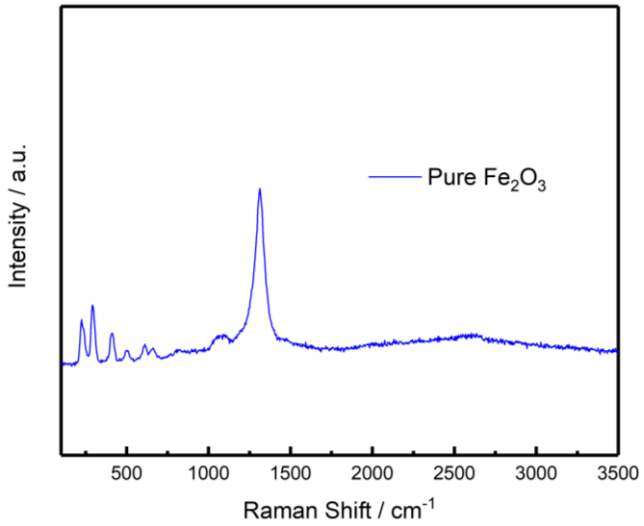

Fig 5.3 Raman spectra of pure α-Fe_2O_3

The $Ni_{18\%}Fe_2O_3$@rGO sample also exhibited a distinct peak at ~720 cm^{-1}, corresponding to the γ-Fe_2O_3 phase identified in the XRD analysis. This peak underscore the structural evolution at higher doping levels and supports the presence of additional phases detrimental to catalytic

performance.

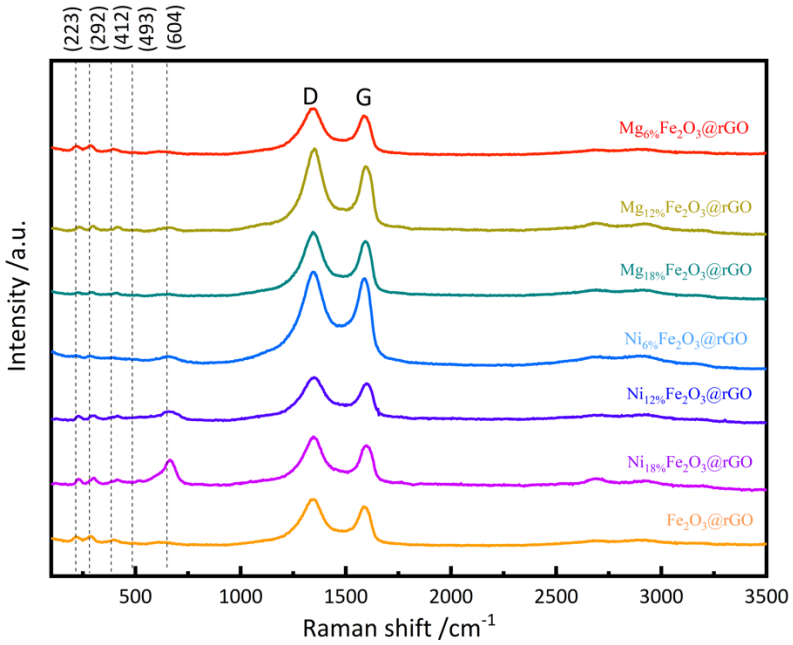

Fig. 5.4 Raman spectra on all samples

To assess the carbon content and determine the electrocatalyst-to-carbon ratio, thermogravimetric analysis (TGA) was performed, as shown in Fig. 5.5. All samples displayed comparable (doped) Fe_2O_3/C ratios, ranging from 36% to 39%, aligning well with values reported in the literature. Based on the electrode preparation method, these ratios correspond to an approximate (doped) Fe_2O_3 loading of 65–78 $\mu g \cdot cm^{-2}$, ensuring sufficient active material for efficient catalytic performance[101].

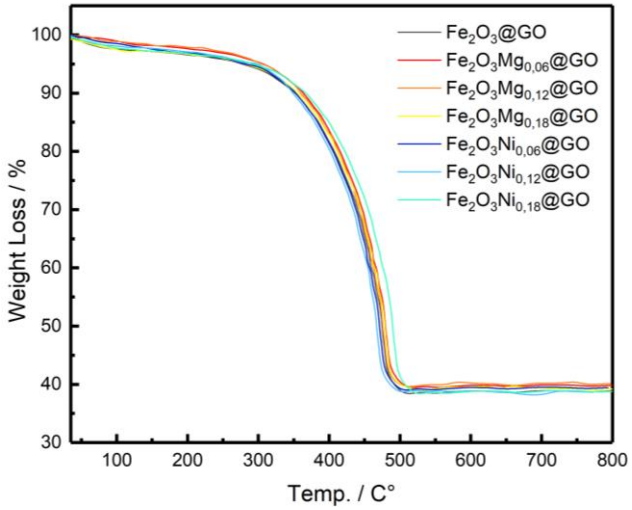

Fig. 5.5 TGA analysis on all samples

Scanning Electron Microscopy (SEM) was conducted for all the synthesized samples, and the resulting micrographs are presented in Fig. 5.6. The electrocatalysts exhibit nanoparticle dimensions ranging from 30 nm to 75 nm. The nanoparticles are uniformly distributed across the graphene oxide substrate with minimal agglomeration. This nanoscale distribution is crucial for optimizing electrocatalytic activity, as it provides a high surface-to-volume ratio, enhancing both Turn Over Number (TON) and Turn Over Frequencies (TOF). Among the samples, Mg6% and Ni6% demonstrated the smallest particle sizes, suggesting a potential correlation between particle size and catalytic efficiency.

Energy Dispersive X-ray (EDX) mapping confirmed a homogeneous distribution of all elements in the catalysts, indicating effective doping. Elemental analysis, summarized in Table 5.2, revealed that the dopant concentrations closely match the intended values, with only negligible variations.

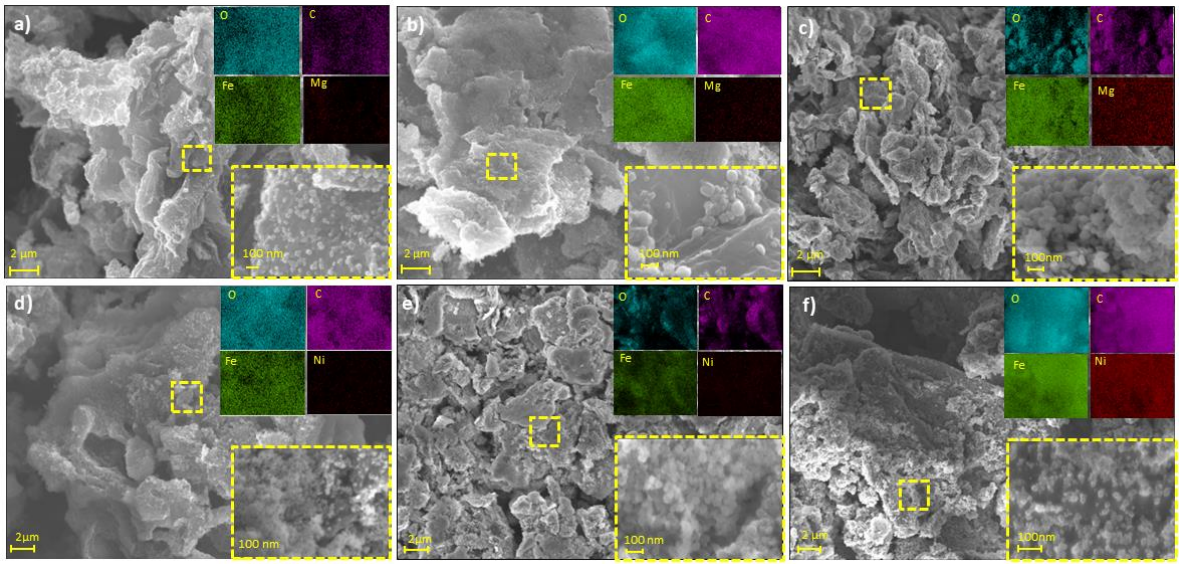

Fig 5.6 SEM, mapping and EDX on (a) $Mg_{6\%}Fe_2O_3$@rGO,(b) $Mg_{12\%}Fe_2O_3$@rGO, (c) $Mg_{18\%}Fe_2O_3$@rGO, (d) $Ni_{6\%}Fe_2O_3$@rGO, (e) $Ni_{12\%}Fe_2O_3$@rGO, and (f) $Ni_{18\%}Fe_2O_3$@rGO and relative mapping of Oxygen (blue), Carbon (violet), Iron (green) and Dopant (red).

Table 5.2 Results of EDX analysis

Catalyst Name	Wt% (Fe)	Wt% (Ni)	Calculated percentage of dopants (%)
$Mg_{6\%}Fe_2O_3$@rGO	40.16	1.99	≈ 5%
$Mg_{12\%}Fe_2O_3$@rGO	29.90	2.49	≈ 11%
$Mg_{18\%}Fe_2O_3$@rGO	41.76	7.50	≈ 17%
$Ni_{6\%}Fe_2O_3$@rGO	28.40	1.69	≈ 6%
$Ni_{12\%}Fe_2O_3$@rGO	31.13	4.17	≈ 12%
$Ni_{18\%}Fe_2O_3$@rGO	34.21	6,04	≈ 17%

To better understand the impact of doping and the chemical states of the electrocatalysts, X-ray Photoelectron Spectroscopy (XPS) analysis was performed. The results for $Mg_{6\%}Fe_2O_3$@rGO and $Ni_{6\%}Fe_2O_3$@rGO, the two most promising materials based on their morphological and structural properties, are shown in Fig. 5.7.

In the XPS profile of the Ni-doped sample, peaks corresponding to Fe 2p, O 1s, C 1s, N 1s, and Ni 2p are clearly visible, while the Mg-doped sample displays peaks for Fe 2p, O 1s, C 1s, N 1s, and Mg 2p (Fig. 5.7a). Due to the lower sensitivity of XPS to Mg (approximately half that of Fe) and its susceptibility to carbon contamination, along with the core-shell morphology of the Mg-doped sample, Mg detection was less pronounced. Conversely, Ni was detected prominently in the Ni-doped sample (Fig. 5.7b)[108].

The C 1s spectra (Figs. 5.6c, d) reveal peaks corresponding to sp^2-bonded carbon (C–C/C=C) at 284.8 eV, epoxy and alkoxy groups (C–O) at 286.2 eV, and carbonyl and carboxylic groups (O–C=O) at 287.6 eV, consistent with typical graphene-related functionalities.

The O 1s spectra (Figs. 5.7e, f) show three distinct peaks at 530.2 eV (Fe–O), 531.8 eV (C–O–Fe), and 533.4 eV (C–OH/C–O–C), confirming the interaction between Fe_2O_3 and graphene via C–O–Fe bonds in both Ni- and Mg-doped composites.

The Fe 2p spectra (Figs. 5.7g, h) feature two main peaks at 710.8 eV and 725.3 eV, corresponding to Fe $2p_{3/2}$ and Fe $2p_{1/2}$, respectively. Additionally, shake-up satellite peaks are visible, which are characteristic of Fe^{3+} in the hematite structure[100,114–116].

These findings support the successful incorporation of dopants and the establishment of strong chemical interactions between Fe_2O_3 and rGO, crucial for enhancing the electrocatalytic performance of the materials.

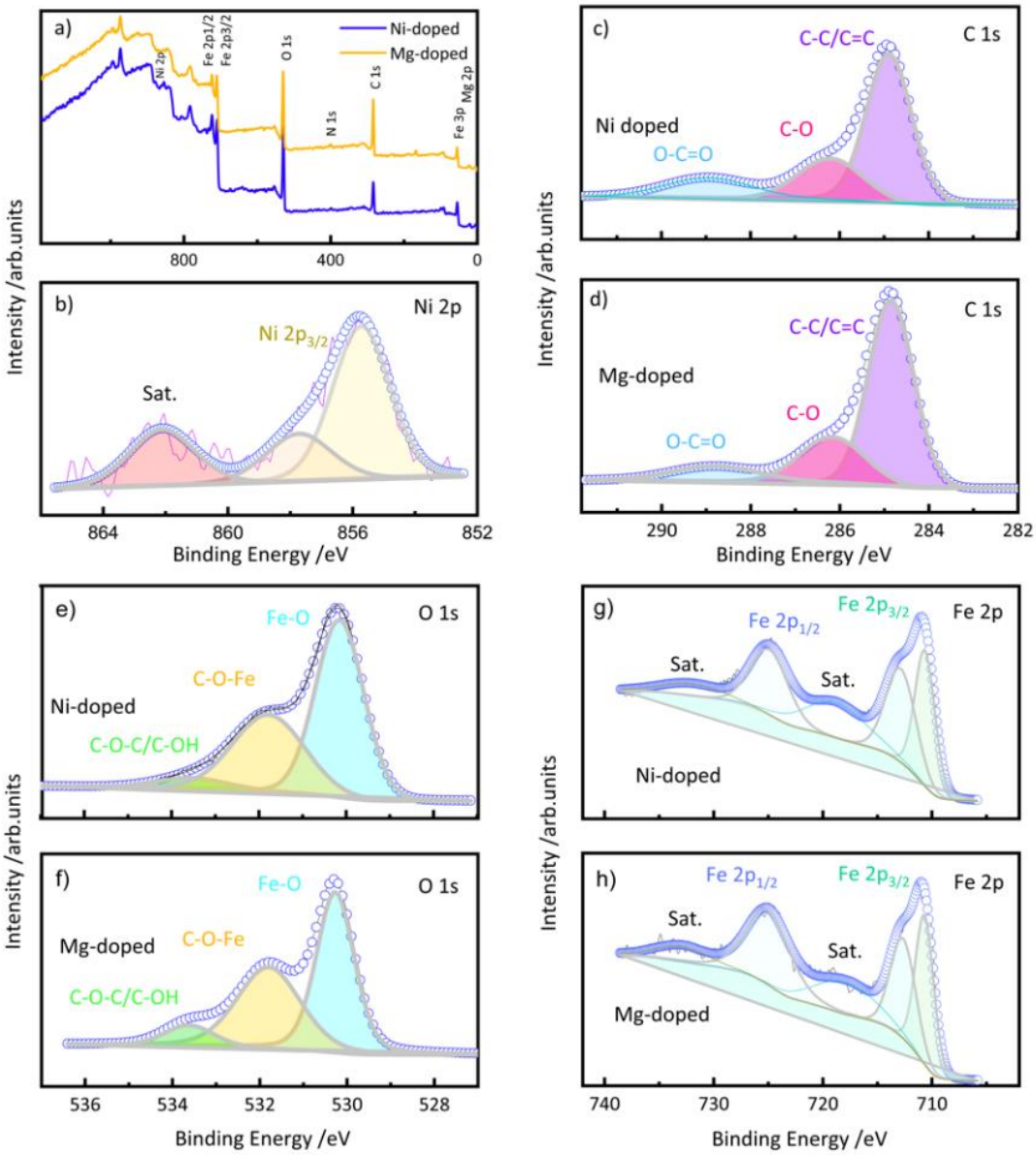

Fig. 5.7 XPS on the Mg and Ni 6% doped iron oxide

5.2.2 Electrochemical characterization

To evaluate the electrocatalytic activity of the synthesized materials, Rotating Ring Disk Electrode (RRDE) measurements were conducted. The ORR performance was analyzed using Linear Sweep Voltammetry (LSV) in an oxygen-saturated 0.1 M KOH alkaline electrolyte. For this

analysis, the electrocatalysts were ground and mixed with Ketjenblack (KJB) to improve conductivity and ensure a homogeneous electrode film.

The ORR activities of all electrocatalyst-KJB composites at a rotation speed of 1600 rpm are depicted in Fig. 5.8. This high rotation speed ensures efficient oxygen transport to the electrode surface, minimizing diffusion limitations and enabling a clearer assessment of intrinsic catalytic activity[95,117–119].

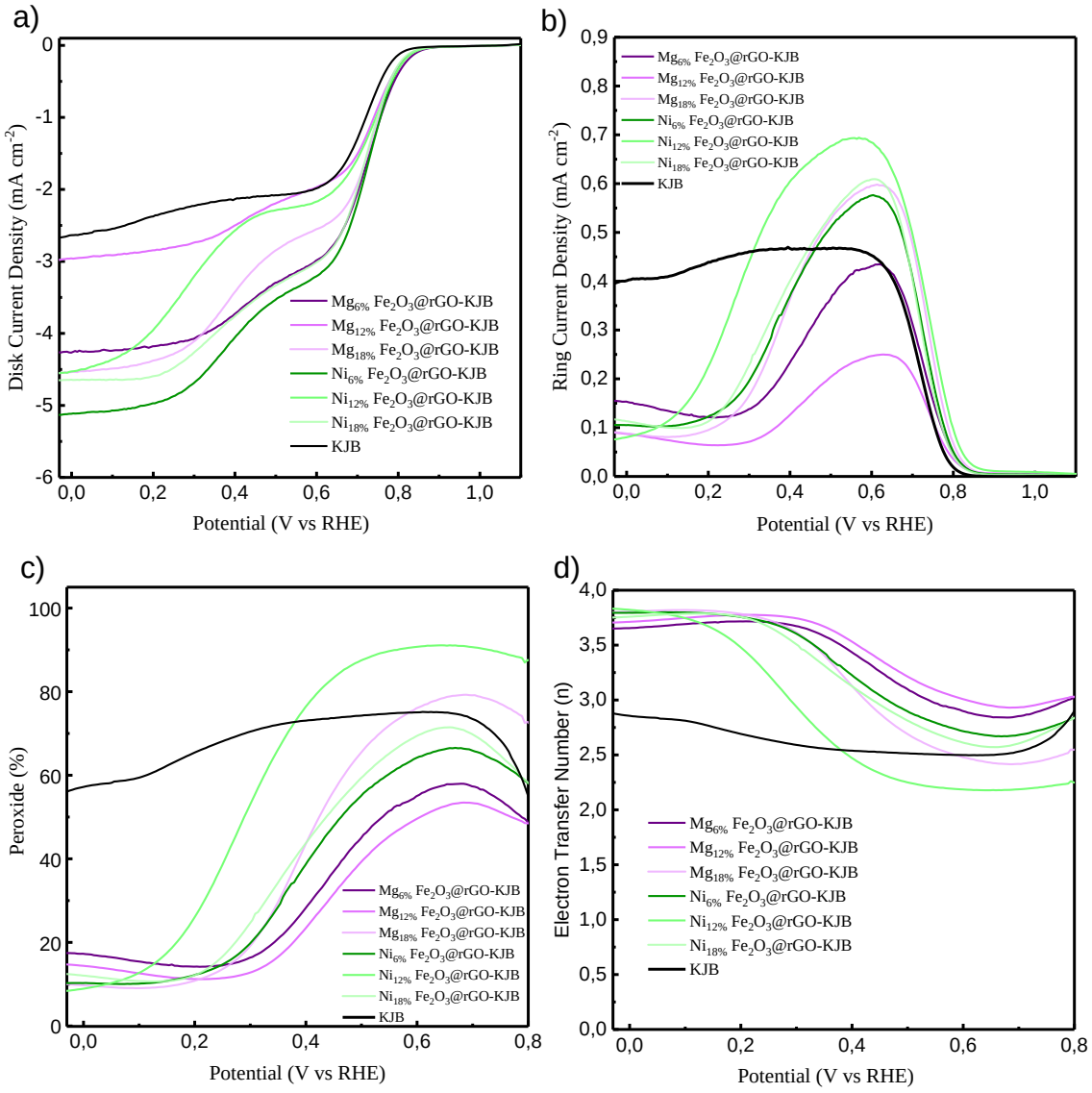

Fig. 5.8 Comparison of the iron oxide catalysts/ KJB composite at RRDE

As seen in Fig. 5.8a, the disk current densities of the various composites reveal a general trend where none of the systems fully reach a diffusion-limited regime. The onset potentials, which mark the initial reduction of oxygen, are consistent across the samples. $Mg_{6\%}$-, $Mg_{12\%}$-, and

$Ni_{18\%}Fe_2O_3$@rGO show an onset potential of 0.84 V (vs. RHE), while other samples slightly lag at 0.83 V (vs. RHE). The half-wave potentials, another key metric of ORR efficiency, are lowest for $Ni_{18\%}$-, $Ni_{6\%}$-, and $Mg_{6\%}Fe_2O_3$@rGO, registering at 0.72 V and 0.73 V (vs. RHE), respectively. This indicates slightly hindered kinetics for these systems compared to the others.

A notable decrease in ring current densities is observed for the electrocatalyst composites compared to pure KJB. This suggests a reduction in peroxide yield, indicating that these materials possess favorable peroxide scavenging properties. This characteristic is essential for enhancing the selectivity of the ORR toward the four-electron pathway, which is critical for energy applications like fuel cells.

To quantify the peroxide yield and assess the electrochemical selectivity of the materials, the following equation (Eq. 5.8) was employed[119,120]:

$$\%Peroxide = \frac{2*\frac{I_{ring}}{N}}{I_{disk}+\frac{I_{ring}}{N}} \tag{5.7}$$

Where I_{ring} and I_{disk} are the ring and disk currents, respectively, and N is the collection efficiency of the RRDE system. This equation enables a precise evaluation of the selectivity toward H_2O_2 production, further confirming the promising catalytic behavior of these materials.

Consistent with the trends observed in Figs. 5.7a and 5.7b, $Mg_{6\%}$- and $Ni_{6\%}Fe_2O_3$@rGO display the lowest peroxide production relative to their disk current densities, achieving peak peroxide yields of 57.9% and 66.5%, respectively. This suggests that these catalysts are effective in minimizing the formation of undesirable by-products, indicating enhanced stability and reaction efficiency.

The electron transfer number (n) a critical indicator of ORR pathway selectivity was derived from the disk and ring current data using the following equation[95,97,98,120]:

$$n = \frac{4*I_{disk}}{I_{disk}+\frac{I_{ring}}{N}} \tag{5.7}$$

Fig. 5.8d presents n as a function of the applied voltage. Across the voltage range, Mg6% and $Ni_{6\%}Fe_2O_3$@rGO demonstrate the highest electron transfer numbers, highlighting their superior catalytic performance and selectivity for the four-electron ORR pathway. $Mg_{12\%}Fe_2O_3$@rGO shows the lowest ring current densities and peroxide production, with the highest electron transfer number among all tested samples, nevertheless it was not selected for further analysis due to its lower disk current densities.

Building on these findings, $Mg_{6\%}$- and $Ni_{6\%}Fe_2O_3$@rGO were identified as the most promising candidates for peroxide scavenging. These catalysts were combined with a ORR catalyst synthesized by M. Muhyuddin et al.[97], FePc600, in two distinct ($(Mg/Ni)_{6\%}Fe_2O_3$@rGO to FePc600) ratios: 80:20 and 20:80 This experimental setup aimed to investigate the impact of different compositions on overall peroxide mitigation, offering valuable insights into optimal electrocatalyst blending strategies for enhanced performance in practical applications.

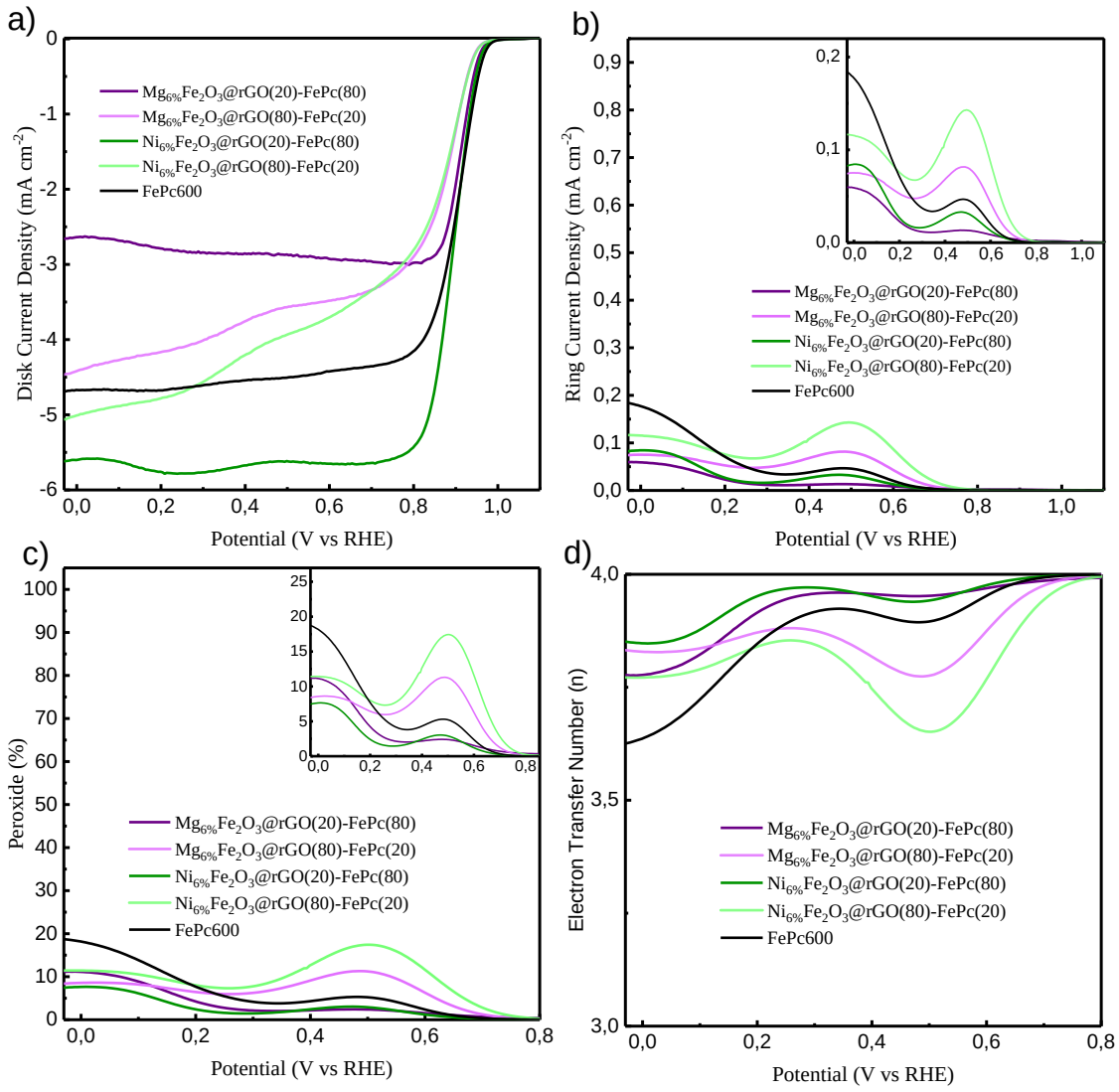

Fig. 5.9 illustrates a detailed comparison of the performance of two composite material configurations, emphasizing the impact of the electrocatalyst-to-FePc600 ratio.

The 80:20 (80% electrocatalyst and 20% FePc600) composites exhibit limited improvement, with performance metrics such as disk current density failing to reach the diffusion-limited regime (Fig. 5.8a). Furthermore, ring current and peroxide production metrics (Figs. 5.8b-d) suggest that these composites perform worse than pure FePc600, indicating a suboptimal electrocatalyst balance for this ratio.

In contrast, the 20:80 composites (20% electrocatalyst and 80% FePc600) display significant enhancements. Notably, the disk current densities for $Mg_{6\%}$- and $Ni_{6\%}Fe_2O_3$@rGO reach 2.6 mA cm^{-2} and 5.6 mA cm^{-2}, respectively, achieving a full diffusion-limited regime (Fig. 5.8a).

This enhancement is paired with lower ring current densities (Fig. 5.8b), which correspond to reduced peroxide production. As shown in Fig. 5.8d, $Mg_{6\%}$- and $Ni_{6\%}$-based composites exhibit peroxide production levels as low as 2.4% and 2.9%, respectively, at 0.5 V vs. RHE. This is a marked improvement compared to the 5.1% peroxide production of pure FePc600.

These findings suggest that the 20:80 composites provide a better electrocatalytic balance, improving both efficiency and selectivity. Specifically, the $Ni_{6\%}$Fe2O3@rGO/FePc600 composite emerges as the superior candidate, with its high disk current density, reduced peroxide production, and increased electron transfer number (Fig. 5.8c).

5.3 Conclusions

This study presents an effective strategy to enhance the electrocatalytic performance and selectivity of Fe_2O_3@rGO by incorporating Mg and Ni dopants via a cost-efficient synthesis. RRDE analysis confirmed improved electrochemical selectivity for all doped catalysts, with $Ni_{6\%}Fe_2O_3$@rGO showing superior peroxide scavenging, critical for protecting FC membranes. The enhanced performance is attributed to lattice contraction, as determined by XRD refinement, oxygen vacancies, partial GO reduction, and reduced grain size, which collectively improve electron conduction and charge transfer. The composite materials made with FePc600 also provided a further insight on the peroxide scavenging proprieties of $Ni_{6\%}Fe_2O_3$@rGO showing not only the decreased peroxide formation but also the improvement of disk current density up to 1 mA/cm^2 compared with the other compositions ($Mg_{6\%}Fe_2O_3$@rGO). This work provides valuable insights into doping strategies for iron oxide electrocatalysts, highlighting their potential as cocatalysts to enhance ORR efficiency.

References

1. Liu, Y. *et al.* PEM fuel cell electrocatalysts based on transition metal macrocyclic compounds. *Coordination Chemistry Reviews* vol. 315 153–177 Preprint at https://doi.org/10.1016/j.ccr.2016.02.002 (2016).
2. Nie, Y., Li, L. & Wei, Z. Recent advancements in Pt and Pt-free catalysts for oxygen reduction reaction. *Chemical Society Reviews* vol. 44 2168–2201 Preprint at https://doi.org/10.1039/c4cs00484a (2015).
3. Abbas, M. A. & Bang, J. H. Rising Again: Opportunities and Challenges for Platinum-Free Electrocatalysts. *Chemistry of Materials* **27**, 7218–7235 (2015).
4. Ren, X. *et al.* Current progress of Pt and Pt-based electrocatalysts used for fuel cells. *Sustain Energy Fuels* **4**, 15–30 (2019).
5. Rojas-Carbonell, S. *et al.* Effect of pH on the Activity of Platinum Group Metal-Free Catalysts in Oxygen Reduction Reaction. *ACS Catal* **8**, 3041–3053 (2018).
6. Ge, X. *et al.* Oxygen Reduction in Alkaline Media: From Mechanisms to Recent Advances of Catalysts. *ACS Catal* **5**, 4643–4667 (2015).
7. Artyushkova, K. *et al.* Correlations between Synthesis and Performance of Fe-Based PGM-Free Catalysts in Acidic and Alkaline Media: Evolution of Surface Chemistry and Morphology. *ACS Appl Energy Mater* **2**, 5406–5418 (2019).
8. Zhao, J. *et al.* Manipulating the oxygen reduction reaction pathway on Pt-coordinated motifs. *Nat Commun* **13**, (2022).
9. Muhyuddin, M. *et al.* Formation of the active site structures during pyrolysis transformation of Fe-phthalocyanine into Fe-Nx-C electrocatalysts for the oxygen reduction reaction. *Appl Catal B* **343**, (2024).
10. Santoro, C. *et al.* High catalytic activity and pollutants resistivity using Fe-AAPyr cathode catalyst for microbial fuel cell application. *Sci Rep* **5**, (2015).
11. Santoro, C. *et al.* A family of Fe-N-C oxygen reduction electrocatalysts for microbial fuel cell (MFC) application: Relationships between surface chemistry and performances. *Appl Catal B* **205**, 24–33 (2017).
12. Gan, R. *et al.* Fe2O3-encapsulated and Fe-Nx-containing hierarchical porous carbon spheres as efficient electrocatalyst for oxygen reduction reaction. *Int J Hydrogen Energy* **47**, 2103–2113 (2022).
13. Liu, X. & Hu, W. Iron oxide/oxyhydroxide decorated graphene oxides for oxygen reduction reaction catalysis: A comparison study. *RSC Adv* **6**, 29848–29854 (2016).

14. Benzigar, M. R. *et al.* Highly ordered iron oxide-mesoporous fullerene nanocomposites for oxygen reduction reaction and supercapacitor applications. *Microporous and Mesoporous Materials* **285**, 21–31 (2019).
15. Sim, W. J. *et al.* Efficient iron-cobalt oxide bifunctional electrode catalysts in rechargeable high current density zinc-air batteries. *Nanoscale* **14**, 8012–8022 (2022).
16. Lee, H. *et al.* Facile synthesis of iron oxide/graphene nanocomposites using liquid phase plasma method. *J Nanosci Nanotechnol* **16**, 4483–4486 (2016).
17. Kerli, S. & Soğuksu, A. K. Production of iron oxide and nickel oxide nanostructural particles, investigation of the supercapacitor and photocatalytic properties. *Z Kristallogr Cryst Mater* (2019) doi:10.1515/zkri-2019-0043.
18. Katikaneani, P., Vaddepally, A. K., Reddy Tippana, N., Banavath, R. & Kommu, S. Phase Transformation of Iron Oxide Nanoparticles from Hematite to Maghemite in Presence of Polyethylene Glycol: Application as Corrosion Resistant Nanoparticle Paints. *Journal of Nanoscience* **2016**, 1–6 (2016).
19. Ma, M. *et al.* Synthesis of iron oxide/partly graphitized carbon composites as a high-efficiency and low-cost cathode catalyst for microbial fuel cells. *ACS Appl Mater Interfaces* **6**, 13438–13447 (2014).
20. Abe, S. & Watanabe, M. Mg-induced phase transformation from hematite to maghemite. *Mater Res Express* **1**, (2014).
21. Vulcu, A., Radu, T., Turza, A. & Berghian-Grosan, C. Iron-based graphene composite for oxygen reduction reaction in alkaline media: Electrocatalytic activity and lifetime evaluation. *Applied Surface Science Advances* **21**, (2024).
22. Garino, N. *et al.* One-Pot Microwave-Assisted Synthesis of Reduced Graphene Oxide/Iron Oxide Nanocomposite Catalyst for the Oxygen Reduction Reaction. *ChemistrySelect* **1**, 3640–3646 (2016).
23. Ma, M. *et al.* Silver/iron oxide/graphitic carbon composites as bacteriostatic catalysts for enhancing oxygen reduction in microbial fuel cells. *J Power Sources* **283**, 74–83 (2015).
24. Santoro, C. *et al.* Design of Iron(II) Phthalocyanine-Derived Oxygen Reduction Electrocatalysts for High-Power-Density Microbial Fuel Cells. *ChemSusChem* **10**, 3243–3251 (2017).
25. Lassoued, A., Dkhil, B., Gadri, A. & Ammar, S. Control of the shape and size of iron oxide (α-Fe2O3) nanoparticles synthesized through the chemical precipitation method. *Results Phys* **7**, 3007–3015 (2017).
26. Ren, S., Ma, S., Yang, Y., Mao, Q. & Hao, C. Hydrothermal synthesis of Fe2O3/polypyrrole/graphene oxide composites as highly efficient electrocatalysts for oxygen

reduction reaction in alkaline electrolyte. *Electrochim Acta* **178**, 179–189 (2015).

27. Park, G. D., Cho, J. S., Lee, J. K. & Kang, Y. C. Na-ion Storage Performances of FeSex and Fe2O3 Hollow Nanoparticles-Decorated Reduced Graphene Oxide Balls prepared by Nanoscale Kirkendall Diffusion Process. *Sci Rep* **6**, (2016).
28. Liu, R., Xu, Y. & Chen, B. Self-Assembled Nano-FeO(OH)/Reduced Graphene Oxide Aerogel as a Reusable Catalyst for Photo-Fenton Degradation of Phenolic Organics. *Environ Sci Technol* **52**, 7043–7053 (2018).
29. Rojas-Carbonell, S., Santoro, C., Serov, A. & Atanassov, P. Transition metal-nitrogen-carbon catalysts for oxygen reduction reaction in neutral electrolyte. *Electrochem commun* **75**, 38–42 (2017).
30. Muhyuddin, M. *et al.* Valorization of the inedible pistachio shells into nanoscale transition metal and nitrogen codoped carbon-based electrocatalysts for hydrogen evolution reaction and oxygen reduction reaction. *Mater Renew Sustain Energy* **11**, 131–141 (2022).
31. Muhyuddin, M. *et al.* Waste Face Surgical Mask Transformation into Crude Oil and Nanostructured Electrocatalysts for Fuel Cells and Electrolyzers. *ChemSusChem* **15**, (2022).
32. Muhyuddin, M. *et al.* Iron-based electrocatalysts derived from scrap tires for oxygen reduction reaction: Evolution of synthesis-structure-performance relationship in acidic, neutral and alkaline media. *Electrochim Acta* **433**, (2022).

Chapter 6.

MEA and FCs Stack Test Bench

This chapter describes the results of my experience at LOCCIONI AEA company, which was part of my PhD activities under the framework of PON, EU Social Europe fund and Ministero dell'istruzione e della ricerca funding, governed by EU Regulation 1303/2013 and 1304/2013[1].

LOCCIONI AEA is a globally recognized Italian company specializing in the design and implementation of cutting-edge measurement and automation systems. Founded in 1968 and headquartered in the Marche region of Italy, the company integrates advanced technology and innovative solutions to serve a wide range of industries, including automotive, aerospace, energy, healthcare, and environmental monitoring.

LOCCIONI AEA focuses on precision engineering and technological excellence, with a mission to enhance efficiency, quality, and sustainability for its clients. The company work encompasses the entire lifecycle of projects, from research and development to installation and continuous support. Its solutions are tailored to optimize industrial processes, improve product performance, and ensure compliance with rigorous industry standards.

The company is particularly renowned for its expertise in developing customized test benches and automation systems. For instance, in the automotive sector, LOCCIONI AEA provides advanced testing technologies for electric and hybrid vehicles, battery systems, and powertrains. Its commitment to sustainability is reflected in initiatives such as the creation of smart grids and renewable energy solutions[2].

Fig. 6.1 Example of test bench

Through its dedication to innovation, LOCCIONI AEA has established itself as a leader in integrating Industry 4.0 principles, blending human creativity with machine intelligence. This forward-thinking approach has not only strengthened its position in the market but also solidified its role as a pioneer in fostering technological advancements for a better and more sustainable future.

6.1 The Hydrogen Technology

6.1.1 The Global State of Hydrogen Technology

Hydrogen technology is emerging as a cornerstone of the global transition toward cleaner and more sustainable energy systems. As a versatile energy carrier, hydrogen has the potential to decarbonize various sectors, including transportation, industry, and power generation. Its appeal lies in its ability to reduce greenhouse gas emissions, enhance energy security, and facilitate the integration of renewable energy sources.

Hydrogen can be produced through different methods, each with distinct environmental and economic implications. At present, most hydrogen is derived from natural gas via steam methane reforming (SMR), a process that generates significant carbon dioxide emissions. However, there is growing momentum toward "green hydrogen," produced by water electrolysis using renewable energy sources such as wind and solar. This method is considered carbon-neutral and crucial for achieving global climate targets. Another approach, known as "blue hydrogen," involves producing hydrogen from fossil fuels while capturing and storing the resulting carbon emissions. While less environmentally friendly than green hydrogen, blue hydrogen is seen as a transitional

solution on the path toward a low-carbon economy[121].

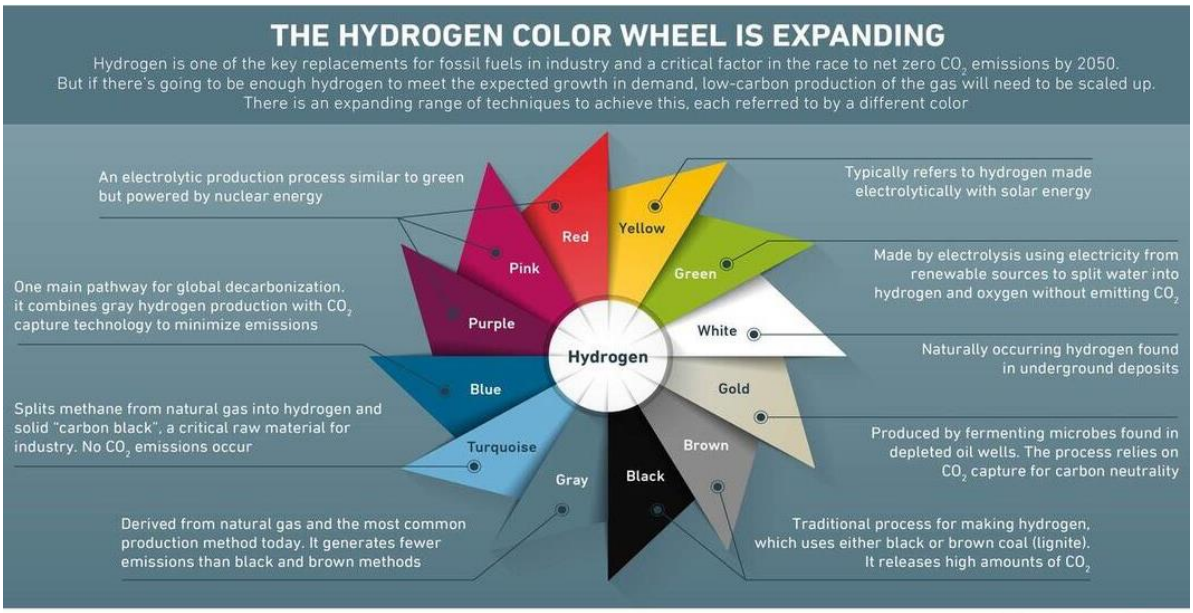

Fig. 6.2 The Hydrogen Color Wheel

Hydrogen applications span several critical areas of modern society. In transportation, hydrogen-powered fuel cell electric vehicles (FCEVs) present a viable alternative to traditional combustion engines, especially for heavy-duty transport where batteries may be less efficient due to their weight and range limitations. In industrial processes, hydrogen is increasingly being used to replace fossil fuels in high-temperature applications, such as steel production and chemical manufacturing, which are typically associated with significant carbon emissions. Moreover, hydrogen ability to store excess renewable energy makes it an effective tool for balancing supply and demand in electricity grids and providing backup power when renewable energy sources like wind or solar are unavailable. Some pilot projects are also exploring the use of hydrogen in residential and commercial heating systems, either by blending it with natural gas or employing it as a standalone energy source.

Several countries have prioritized hydrogen technology in their energy strategies:

- **Europe**: The European Union's Hydrogen Strategy aims to produce 10 million tons of renewable hydrogen annually by 2030, with substantial investment in infrastructure and research. Germany and the Netherlands are leading in policy development and industrial projects.
- **Asia**: Japan has been a pioneer in hydrogen technology, particularly in transportation and residential fuel cells. South Korea and China are also heavily investing in hydrogen vehicles and production facilities.
- **North America**: The United States is fostering hydrogen development through the

Department of Energy's "Hydrogen Shot" initiative, targeting a significant reduction in green hydrogen costs. Canada has also outlined a national hydrogen strategy focused on export and domestic use.

Despite its potential, hydrogen technology faces significant challenges. The high cost of production, especially for green hydrogen, limits its competitiveness compared to fossil fuels. Developing the necessary infrastructure, including pipelines, refueling stations, and storage facilities, presents additional obstacles. Technical issues related to low density and flammability of hydrogen further complicate its storage and transportation. Nevertheless, ongoing advancements in research and development are addressing these challenges, with innovations driving down production costs and improving efficiency.

Hydrogen technology holds immense promise for transforming global energy systems and fighting climate change. While achieving widespread adoption will require coordinated efforts across governments, industries, and academia, the momentum surrounding hydrogen continues to grow, confirming its pivotal role in building a cleaner, more sustainable future.

6.2 LOCCIONI and the Hydrogen Technology

6.2.1 LOCCIONI and Hydrogen Technology: Advancing Innovation in Test Bench Manufacturing

In recent years, LOCCIONI has embraced hydrogen technology, reaffirming its position as a leader in the field of test bench manufacturing. The company has undertaken several projects related to hydrogen production and utilization, with two of the most significant ongoing collaborations involving BOSCH and AUDI. These projects focus on the development of innovative, industrial-scale test benches for electrolyzes and membrane electrode assemblies (MEAs). The projects also underscore LOCCIONI's commitment to innovation and its role in advancing hydrogen technology by delivering state-of-the-art testing solutions tailored to the evolving needs of the industry.

The AUDI project represents a milestone in testing facility design, featuring a fully customized and advanced setup with three distinct operational areas:

1. **Test Bench Area**: This is where the MEA is placed within the press for testing. The area includes all gas piping, humidification lines, and heaters necessary for precise and controlled testing conditions.
2. **Robot and Electrolyzer Area**: Positioned near the test bench, this area houses a robotic system that automates the handling of MEAs, transferring them to the test bench for evaluation. The electrolyzer, used to supply hydrogen, is also located here. To ensure optimal

operating conditions, this area is enclosed within a dedicated dry room.

3. **Operator Area**: Designed with safety as a priority, this section is separated from the other two areas. Operators manage the entire testing process via computer systems, ensuring safe and efficient control of the equipment.

Fig. 6.3 Test Bench robot/electrolyser and testing area

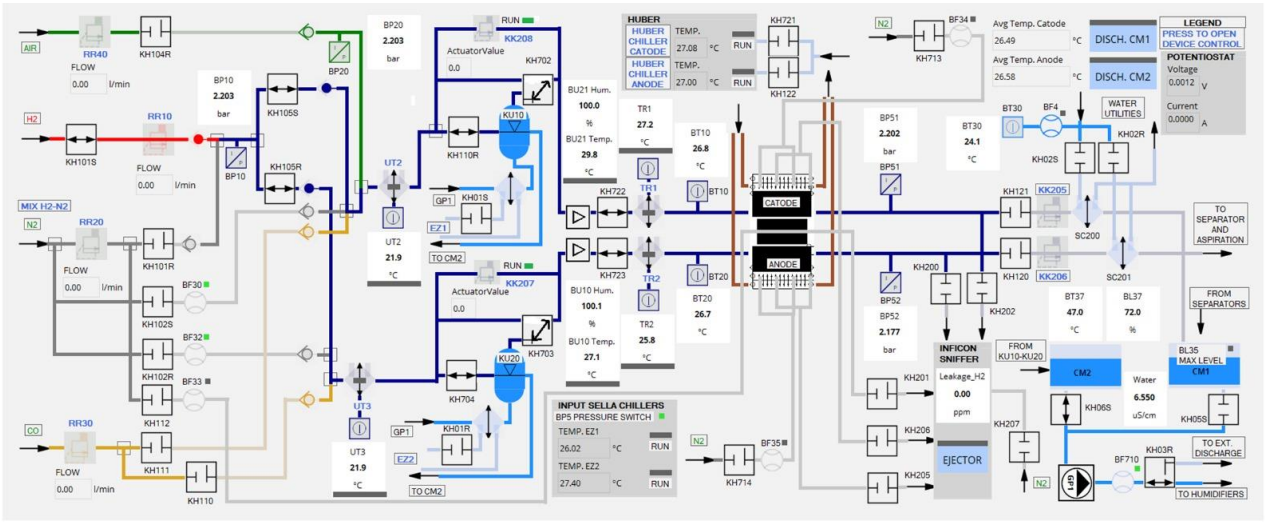

Fig. 6.4 Synoptic of the Audi test bench

6.3 The Bench Development

6.3.1 Development and Challenges in Test Bench Optimization

Over the years, the development of the test bench has undergone numerous iterations and refinements to address technical issues. During the first year after its creation, the bench underwent a pre-acceptance phase (June 2022), which included rigorous tests to meet standards such as

hydrogen leakage prevention, proper area construction, and device labelling verification.

One of the most persistent challenges was related to hydrogen leakage and performance inefficiencies during testing. The initial prototype of the bench failed to deliver any current due to inhomogeneous pressure applied to the membrane electrode assembly (MEA) by the press. This issue was traced back to the design of the gaskets. Using Fuji films for pressure mapping experiments, it was discovered that the original gaskets were absorbing most of the applied force, leaving the MEA insufficiently compressed (Fig. 6.3).

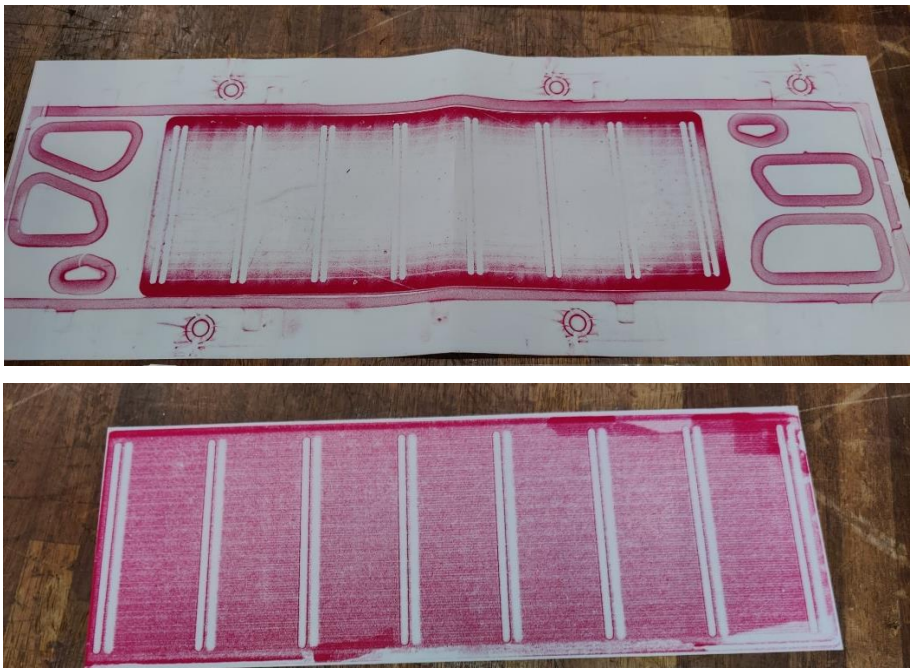

Fig. 6.5 Fuji film pressed with the gaskets and without gaskets

To resolve this, multiple gasket materials were tested. Switching to a soft gasket reduced the absorption issue but introduced significant leakage. When a hard plastic gasket was trialed, it failed to establish proper contact with the press, leaving the MEA unaffected. Ultimately, a hard neoprene gasket was deployed, which resolved the leakage issue. By carefully adjusting the gasket height, the press was finally able to apply uniform pressure across the MEA. This breakthrough allowed the bench to record a current of 30 A, confirming that pressure distribution was a critical factor. While this was a significant milestone, the achieved current remained far below the theoretical expectations. Further investigations were required to optimize the bench performance and address additional factors affecting its efficiency.

Another critical issue encountered during the development of the test bench was the

humidification control system, which raised customer concerns, particularly regarding its sluggish performance and the repeatability of tests. The problem was especially evident on the anode side when operating with low gas flow rates.

The initial prototype of the bench utilized Fumatech H02 (Fig. 6.4) humidifiers, which are industrial bubblers designed for high gas flow applications. However, these humidifiers proved inefficient for hydrogen humidification under various conditions due to hydrogen unique transport properties, which differ significantly from those of other gases. This inefficiency compromised the humidification process, especially at lower flow rates, negatively impacting the system performance.

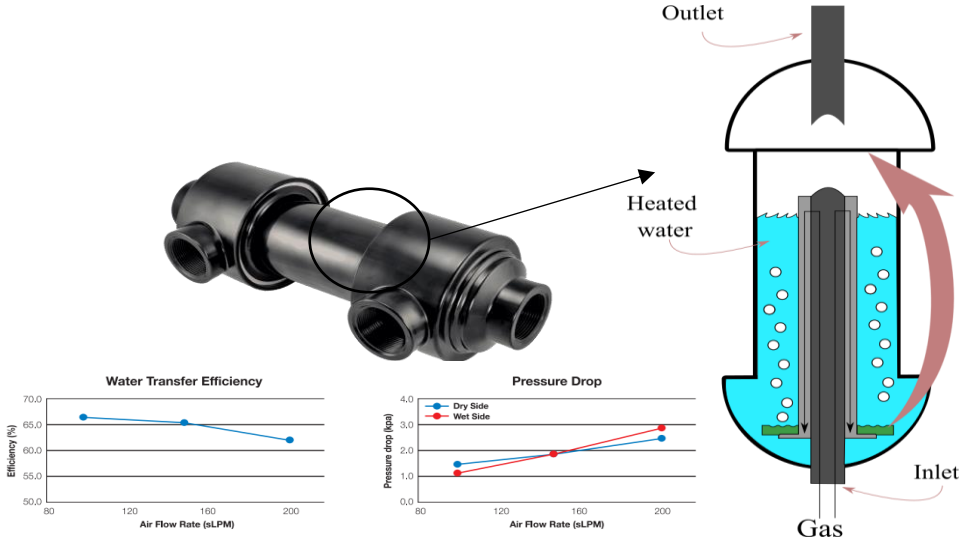

Fig. 6.6 Fumatech h02 type used in the first prototype of the bench and its specifics for air/oxygen humidification

Recognizing the limitations of the Fumatech system, alternative humidification technologies were evaluated and subsequently installed. Among the investigated humidifiers the Permapure seemed the most reliable device especially for the anode side.

The Permapure humidifiers (Fig. 6.5) have similar outside appearance but inside present much more intricated and complex design, indeed this humidifier is composed by a set of concentric small tubes in the inner one pass the gas that have to be humidified and in the outer one pass the ultrapure water, this 2 tubes are separated by a water permeable membrane which allows the passage of small droplet of water that then gets transported by the gas, becoming indeed humidified.

Fig. 6.7 Permapure humidifiers scheme

Thanks to this new device, the humidification system of the bench became more controllable and reproducible which was one of the targets of the June 2022 pre-acceptance.

To investigate the issue related to the low performances we developed tests capable of considering all the parameter related to the bench-MEA interaction area. By these tests was possible to understand that: i) the water-cooling flows and dimensioning were insufficient; ii) a relatively small part of the cell was producing current reaching high temperatures; iii) the press pressure still was not perfectly homogeneous.

Thanks to these new findings, a thorough investigation of different flow field shapes has been conducted to enhance fuel cell performance. Initially, the flow field design featured horizontal channels relative to the membrane electrode assembly (MEA), with a height of 8 mm and a width of 5 mm. This configuration proved suboptimal, as it limited effective gas permeation through the gas diffusion layer (GDL).

Subsequently, a new design was introduced, consisting of shallower channels arranged perpendicular to the MEA. This modification significantly improved gas distribution and led to enhanced performance. Thanks to these additional improvements a more homogeneous distribution of heat and current, indicating an overall improvement of bench-MEA interaction area.

This advanced design achieved remarkable performance gains, with current outputs reaching 220 to 250 A, demonstrating the importance of tailored flow field geometry in fuel cell efficiency.

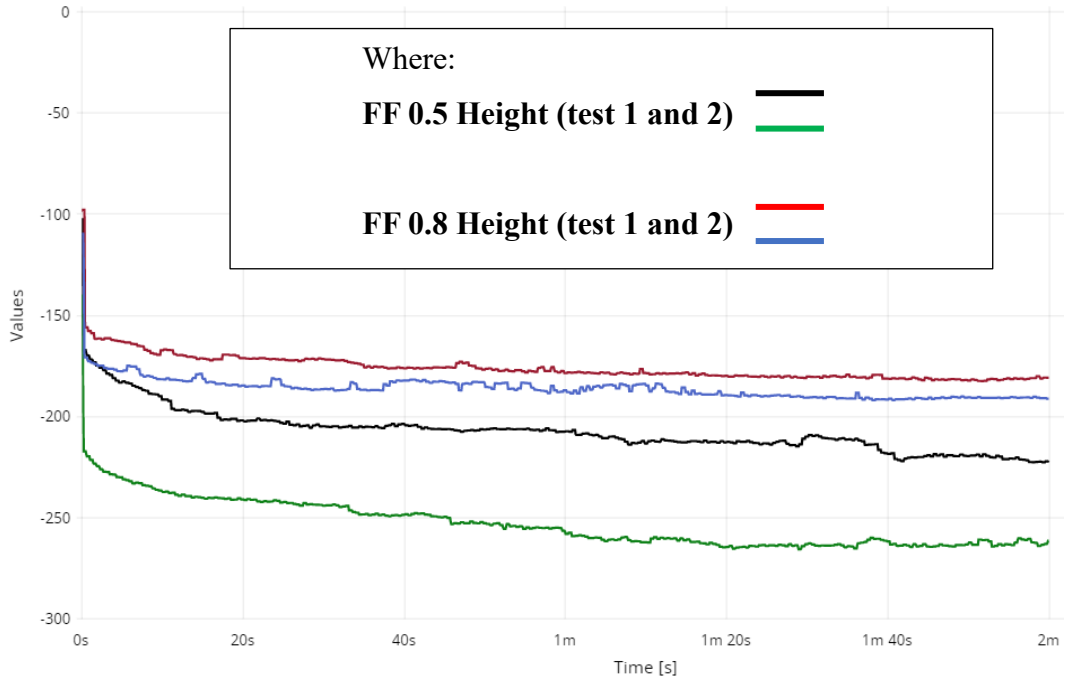

Fig. 6.8 Comparison between different flow field

Then, with the perfectioning of the bench press homogeneity and an improvement of the cooling systems we could obtain a better current and thermal distribution along with 270 A of recorded current.

In addition, an optimization of the potentiostat system allowed us to reach 270-300 A. this improvement included the increase of rack quantities and precision to increase the signal-to-noise ratios, improving the electrochemical sensing by the addition of sensing pin directly on the flow field and a tailored calibration with an impedance master.

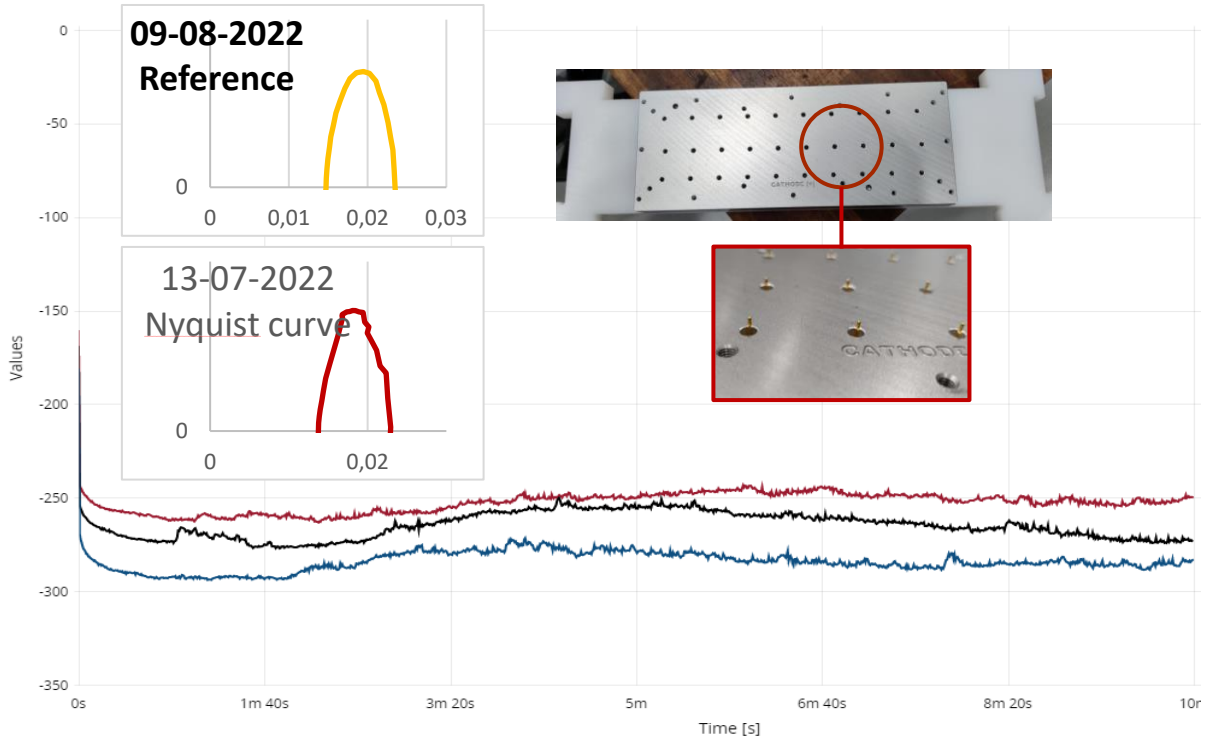

Fig. 6.9 Impedance master test and cycling test after potentiostat improvements

Finally, further improvements of the bench, such as addition of hydrogen mass spectroscopy to the line configuration for safety issue, waste-water management and refill system plus further research on flow field shape and design, allowed the reach of 320-360 A with full reactive control of the parameter in the test bench.

6.3.2 Analytical investigations

6.3.2.1 Investigation of Corrosion Event by Scanning Electron Microscopy

Visual investigation of the state of several bipolar plate (bpp), also supplied by Audi and in which the MEA had been inserted for the characterization after the electrochemical tests, revealed that some portions of the plate underwent a damage resulting in surface modifications, possibly ascribable to corrosion phenomena. This hypothesis was supported by the presence, over the plate, of a dark grey powder, probably coming from the Al current collector plates applied to the bpp/MEA assembly. Figures 6.10 report a picture of the overall bpp and a detail, recorded by an optical microscope image, of one of the damaged areas.

Sampled area #1.

The sampled area #1 contains both channels (marked by the blue square) and channel edges (marked by red square) of the bpp. The very bright areas are the edges of the channels correspond to steep surfaces normal to bpp plane. Damaged areas can be clearly recognized (dark

areas in the channels), while the edges appear quite homogeneous (the different grey intensity is only due to the fact that different surface portions are tilted at slightly different angles, and not to different compositions). The green box corresponds to the area sampled by EPMA, and over which elemental mapping has been carried out.

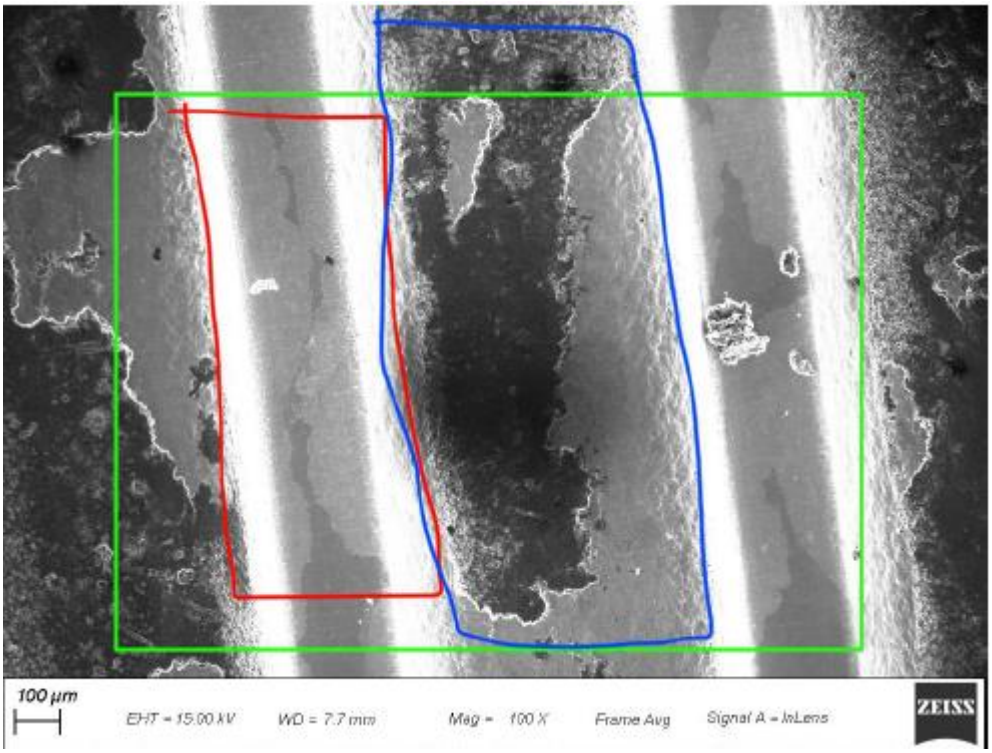

Fig. 6.10 Separation of first sampling areas

The average elemental composition of the surface (sampling depth is approximately few micrometers) is reported in Table 6.1.

Table 6.1 EPMA X-ray emission spectrum and elemental composition of sample area n°1

Elemento	At. No.	Netto	Mass [%]	Mass Norm. [%]	Atom [%]	abs. error [%] (1 sigma)	rel. error [%] (1 sigma)
Carbon	6	73370	50.61	50.55	78.41	5.81	11.48
Oxygen	8	6923	4.96	4.95	5.76	0.73	14.81
Sodium	11	361	0.09	0.09	0.07	0.01	9.81
Magnesium	12	617	0.13	0.13	0.10	0.01	7.77
Aluminium	13	7672	1.41	1.41	0.97	0.07	4.92
Silicon	14	1588	0.26	0.26	0.17	0.01	5.35
Sulfur	16	2463	0.37	0.37	0.22	0.02	4.36
Chlorine	17	1245	0.21	0.21	0.11	0.01	4.79
Potassium	19	1146	0.23	0.23	0.11	0.01	4.62
Chromium	24	19002	8.40	8.39	3.01	0.25	2.99
Iron	26	45128	28.96	28.93	9.65	0.86	2.97
Nickel	28	4068	4.48	4.48	1.42	0.16	3.58
Sum			100.11	100.00	100.00		

The main elements revealed are C (50.55% m/m), Fe (28.93% m/m), Cr (8.39% m/m), O (4.95% m/m), Ni (4.48% m/m), Al (1.41% m/m). The other elements (Na, Mg, Si, S, Cl, K) are

present in amounts lower than 1%. C and Fe are the main constituents, as it may be expected for a steel sample. Cr and Ni can be ascribed to steel as well. O is probably given to minor oxidation of metals (and possibly of C). Al comes from the current collector. It should be noted that some C powder had been applied over the Al current collector to enhance electrical contact between Al current collector and bpp, so part of the recorded C signal can be ascribed to this. To better investigate the damage, elemental mapping has been acquired.

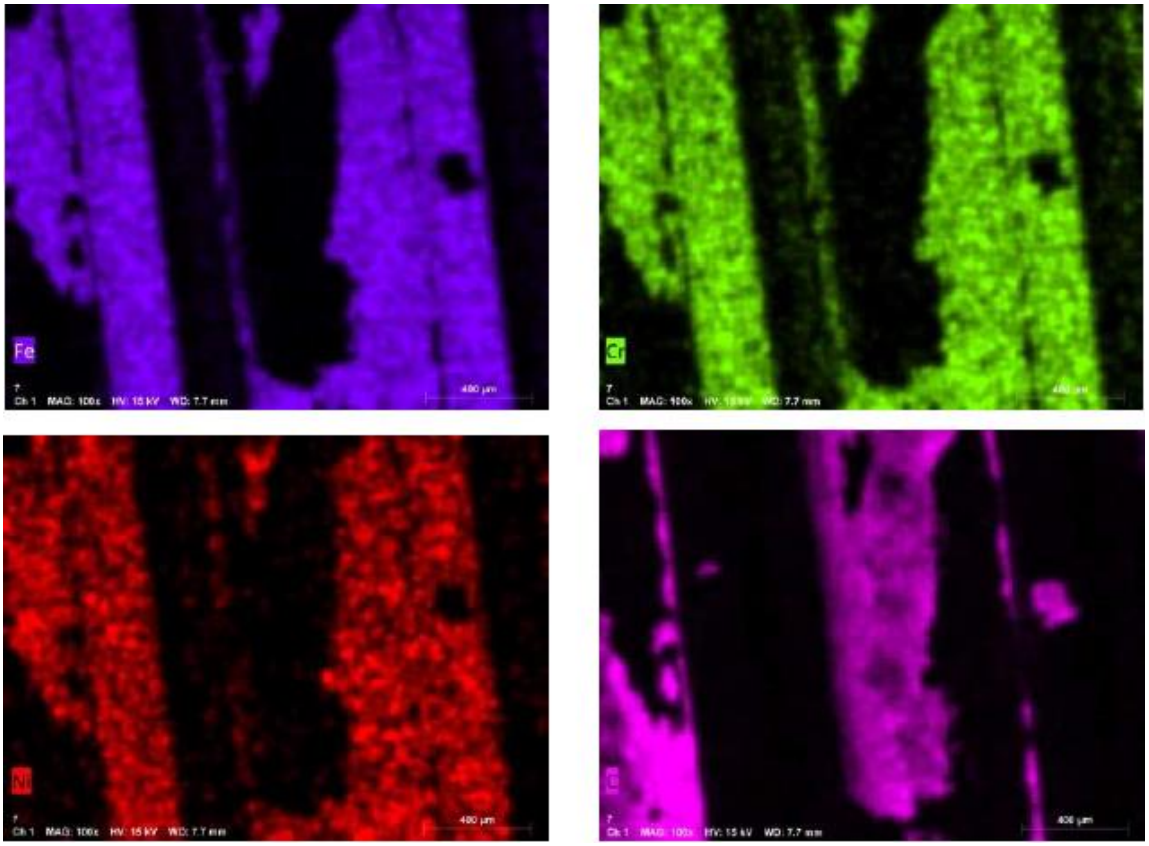

Fig. 6.11 Elemental distribution of Fe, Cr, Ni and C

It appears clearly that Fe, Cr, Ni (i.e. the main components of steel) are still present in the undamaged areas, while they are absent in the damaged areas of the channel, where C is the main component.

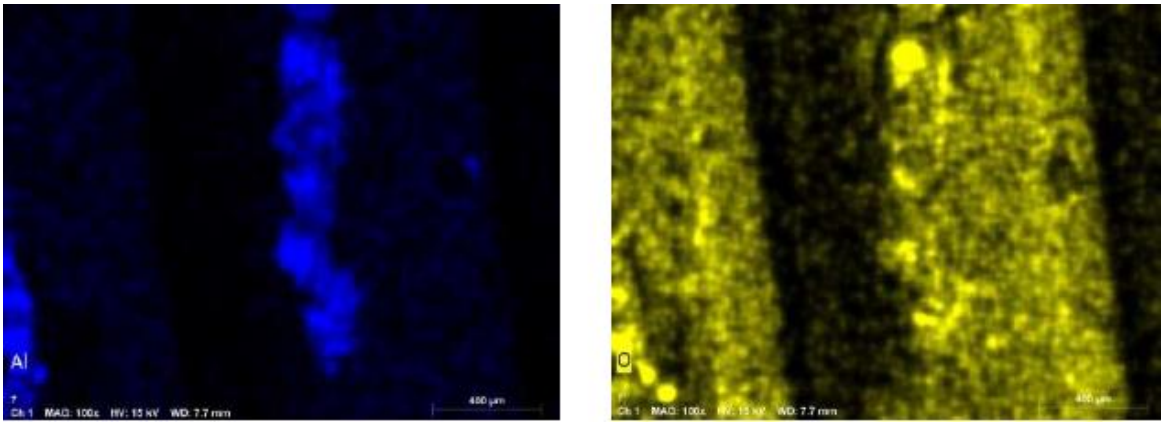

Fig. 6.12 elemental distribution of Al and O

Aluminum (Fig. 6.10) can be found in the damaged areas. This suggests that the contact between steel and Al may be one of the reasons of damage of the bpp. One of the possibilities is that the current drawn from the MEA in a potential range 0.7-0.9V at cathode side oxidizes Al. However, this oxidation, as well the damage of the bpp, appears localized only in specific areas of the surface, so that further investigations are needed to explain the behavior (for instance, the role of possible water droplets in the redox processes at intermetallic contact has to be well evaluated).

Part of the oxygen signal (Figure 6.10) clearly overlaps that of Al (confirming its oxidation); however, its presence is diffused all over the surface and lacking only from those areas that are not facing the X-ray detector because of the geometric beam-sample-detector arrangement.

Sampled area #2.

The sampled area #2 corresponds to two regions: (i) the region on the left, where the damage is clearly visible; (ii) the region on the right, where the surface in intact and appears smoother and more regular. The following analyses have been performed:

1) elemental analysis averaged all over the sampled area. Results are reported in Table 6.2;

2) elemental analysis of a point taken in the damaged area (marked as Corrosion 1 5029 in Fig. 6.13, red arrow). Results are reported in Table 6.3.

3) elemental analysis of a point taken in the intact area (marked as Corrosion 1 5028 in Fig. 6.13, blue arrow). Results are reported in Table 6.4.

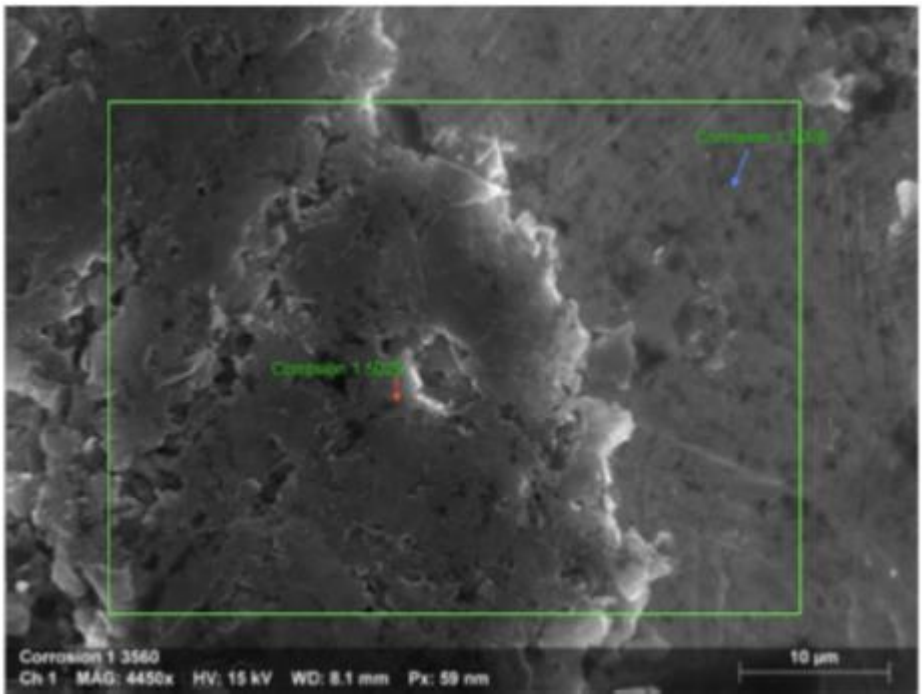

Fig. 6.13 SEM image of secondary sampling area

Table 6.2 (elemental analysis of the average area #2) show the presence of the already

observed elements: C and Fe as main components, O, Cr, Ni, Al and traces of Si, S, Na, K.

Table 6.2 EPMA X-ray emission and elemental composition for sample area #2

Elemento	At. No.	Netto	Mass [%]	Mass Norm. [%]	Atom [%]	abs. error [%] (1 sigma)	rel. error [%] (1 sigma)
Carbon	6	117363	59.20	55.07	82.13	6.81	11.17
Oxygen	8	6228	3.78	3.52	3.94	0.57	15.07
Sodium	11	794	0.16	0.15	0.12	0.01	8.27
Aluminium	13	6639	0.95	0.88	0.50	0.05	4.97
Silicon	14	1768	0.22	0.21	0.13	0.01	5.25
Sulfur	16	3046	0.35	0.32	0.18	0.01	4.22
Potassium	19	1530	0.21	0.20	0.09	0.01	4.29
Chromium	24	23776	7.86	7.12	2.45	0.23	2.97
Iron	26	58011	30.71	28.57	8.16	0.91	2.96
Nickel	28	5178	4.25	3.98	1.21	0.15	3.48
Sum			107.49	100.00	100.00		

Table 6.3 EPMA X-ray emission and elemental composition for corrosion spot 5029 (red arrow in Fig. 6.14)

Elemento	At. No.	Netto	Mass [%]	Mass Norm. [%]	Atom [%]	abs. error [%] (1 sigma)	rel. error [%] (1 sigma)
Carbon	6	228871	87.32	85.42	94.05	9.49	10.86
Nitrogen	7	0	0.00	0.00	0.00	0.00	10.00
Oxygen	8	3542	3.80	3.72	3.08	0.66	17.38
Sodium	11	1914	0.32	0.32	0.18	0.05	14.97
Aluminium	13	1559	0.18	0.17	0.09	0.04	19.90
Silicon	14	964	0.11	0.10	0.05	0.03	29.62
Sulfur	16	2143	0.25	0.24	0.10	0.04	14.55
Potassium	19	2789	0.46	0.45	0.15	0.04	9.18
Chromium	24	5130	1.99	1.95	0.50	0.09	4.56
Iron	26	10123	7.00	6.84	1.62	0.25	3.51
Nickel	28	689	0.80	0.78	0.18	0.07	8.48
Sum			102.23	100.00	100.00		

Table 6.4 EPMA X-ray emission and elemental composition for pristine spot 5028 (blue arrow in Fig. 6.14)

Elemento	At. No.	Netto	Mass [%]	Mass Norm. [%]	Atom [%]	abs. error [%] (1 sigma)	rel. error [%] (1 sigma)
Carbon	6	3193	2.85	3.32	13.21	0.49	17.08
Oxygen	8	3008	0.96	1.12	3.36	0.17	17.19
Silicon	14	2815	0.42	0.48	0.83	0.02	4.94
Sulfur	16	4303	0.59	0.69	1.03	0.02	4.04
Chromium	24	43367	14.86	17.05	15.70	0.43	2.82
Iron	26	110862	58.10	67.60	57.94	1.71	2.94
Nickel	28	10137	8.37	9.73	7.94	0.27	3.27
Sum			85.95	100.00	100.00		

Finally, elemental mapping of the sampled area #2 is reported in Figure 6.15.

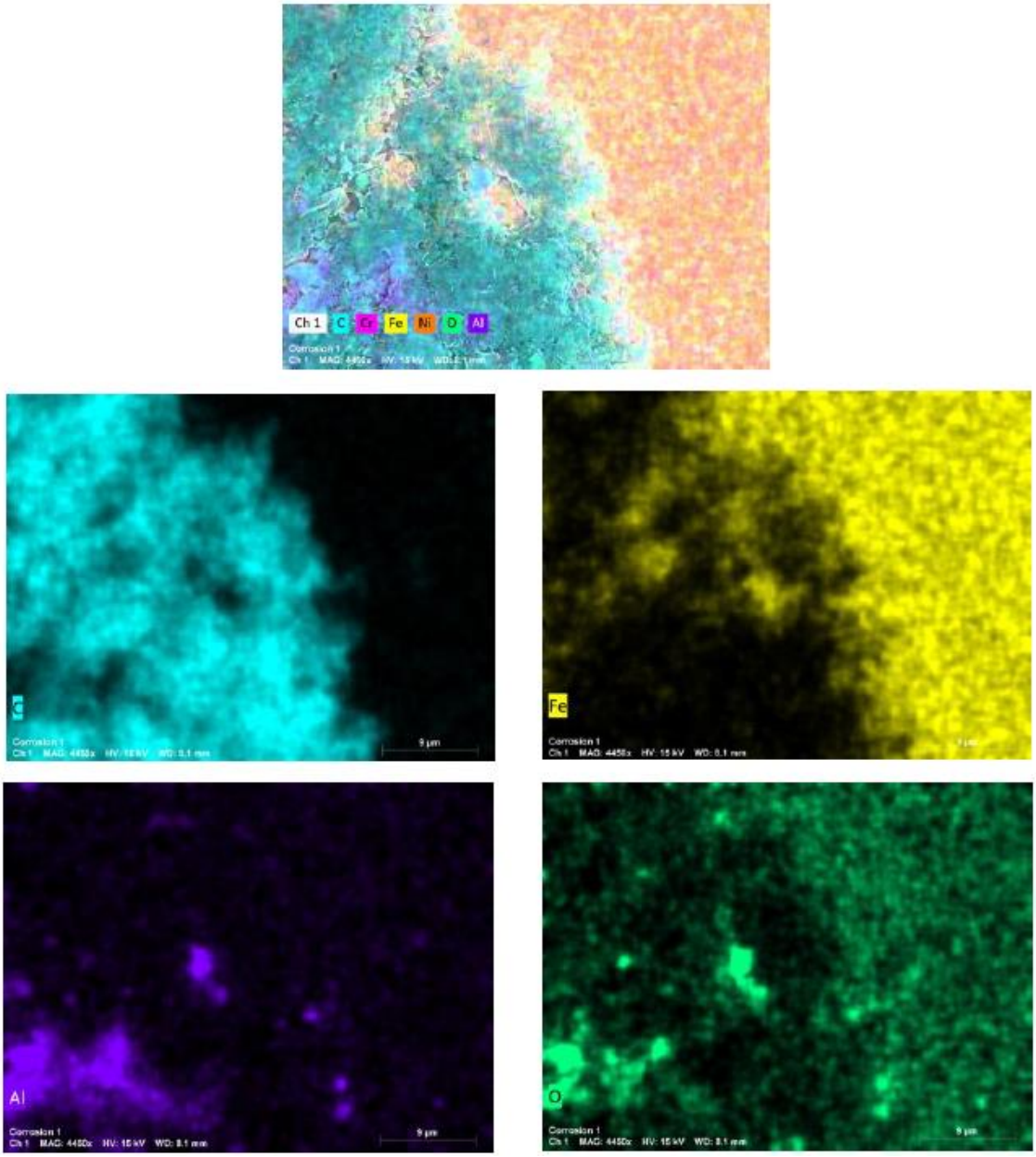

Fig. 6.14 Elemental mapping for sampled area n°2, with superimposition of C, Cr, Fe, Ni, O and Al, detailed signals for C, Fe, Al and O

The elemental mapping clearly confirms the segregation of elements in three different areas: (i) damaged area, where C is predominant; (ii) intact area, where Fe, Ni, Cr are the main signals (mappings of Ni and Cr are not reported here for sake of brevity but they are exactly overlapped to that of Fe); (iii) Al deposits onto part of the damaged area. Oxygen may be detected all over the surface, but the overlapping of part of its distribution with the signal of Al (bottom left in the figures) clearly suggests oxidation of the latter to alumina Al_2O_3. As for sample #1, interaction of O with other elements is suggested but its nature has to be further investigated.

Bipolar plate channel edges.

The SEM/EPMA analysis reveals that, even close to damaged areas in the channels, the

channel edges of the bpp are intact. The surface appears smooth and the elemental mapping (Fig. 6.12) on the edges are typical of intact bpp (Fe, Cr, Ni), while adjacent damaged channels reveal the presence of C. Elemental analysis is summarized in Table 6.5.

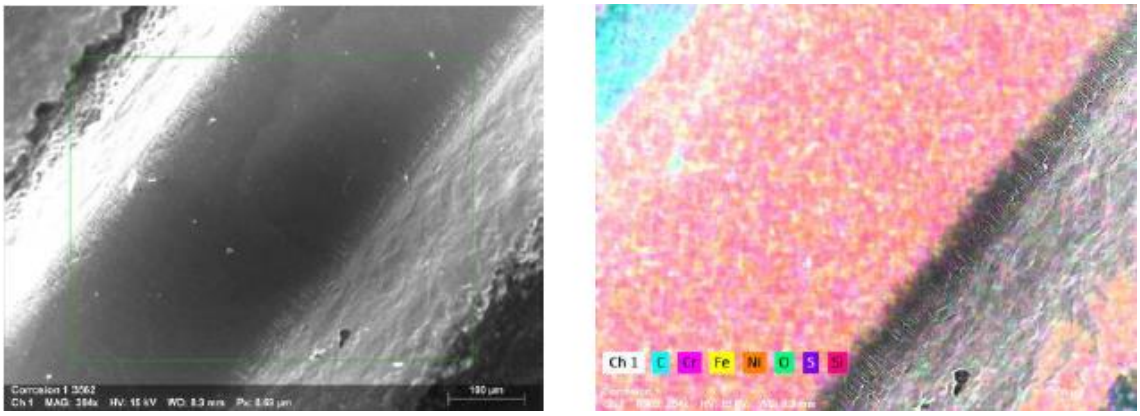

Fig. 6.15 SEM an EPMA of bipolar plater (bpp) channels edges

Table 6.5 EPMA X-ray emission and elemental composition bpp channels edges

Elemento	At. No.	Netto	Mass [%]	Mass Norm. [%]	Atom [%]	abs. error [%] (1 sigma)	rel. error [%] (1 sigma)
Carbon	6	25813	22.52	24.97	58.77	2.81	12.49
Oxygen	8	3566	1.81	2.00	3.54	0.30	16.70
Silicon	14	1667	0.32	0.36	0.36	0.02	5.31
Sulfur	16	2983	0.52	0.57	0.51	0.02	4.23
Chromium	24	30351	12.67	14.05	7.64	0.37	2.94
Iron	26	72478	45.46	50.41	25.51	1.34	2.95
Nickel	28	6640	6.89	7.64	3.68	0.23	3.39
Sum			90.18	100.00	100.00		

Powder detached from Al current collector plate.

As for the bbp samples, also the powder detached from Al current collector plate underwent SEM/EPMA characterization.

Fig. 6.16 reveals very bright areas and poor resolution, which is the signature of oxidized, poorly conductive sample (as for instance Al_2O_3). The elemental mapping reveals that some spots of Fe, Cr, Ni are incorporated in the powder, which is mainly made of Al. Elemental analysis (Table 6.6) confirms large amounts of C (as in damaged channels), which could also come from a pre-treatment of Al plated with C powder to enhance contact with bpp. Oxygen corresponds to 33% m/m amount. Some peaks in the EPMA spectrum also reveal the presence of traces of Na, Mg, K, Ca, with overall amounts below 3% m/m (Ca signal is not integrated in Table 6.6 probably because under quantification limit). The presence of these elements from I and II group, together with O, seem to confirm the hypothesis that some water droplets (coming from the cooling circuit and thus

not deionized) leaked from imperfect bpp sealing into the channels between the upper side of bpp (the side not exposed to MEA) and Al plates, causing local oxidation and resulting into local damage. Oxidation would then result into poor local conduction and eventually into poor MEA performance.

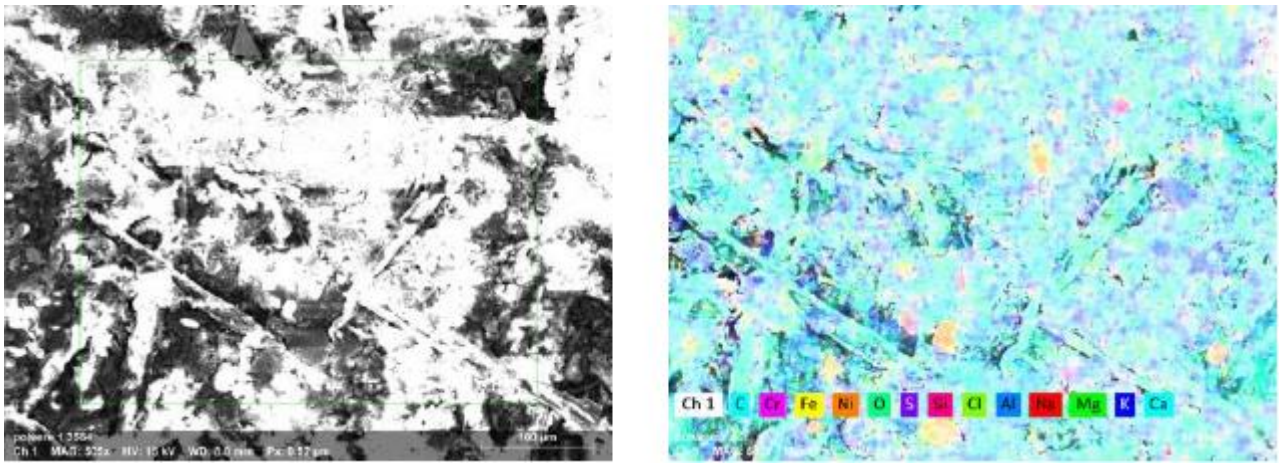

Fig. 6.16 SEM and EPMA for powder collected from Al current collector

Table 6.6 EPMA X-ray emission and elemental composition for powder collected from Al current collector

Element	At. No.	Netto [%]	Mass Norm. [%]	Atom [%]	abs. error [%] (1 sigma)	rel. error [%] (1 sigma)
Carbon	6	24.18	49.00	60.73	2.85	11.80
Oxygen	8	16.34	33.10	30.80	1.98	12.13
Sodium	11	0.40	0.82	0.53	0.03	6.66
Magnesium	12	0.00	0.00	0.00	0.00	3.27
Aluminium	13	5.20	10.54	5.82	0.24	4.65
Silicon	14	0.00	0.00	0.00	0.00	2.15
Phosphorus	15	0.00	0.00	0.00	0.00	1.79
Sulfur	16	0.00	0.00	0.00	0.00	1.52
Chlorine	17	0.53	1.07	0.45	0.02	3.67
Potassium	19	0.13	0.26	0.10	0.01	6.45
Calcium	20	0.82	1.65	0.61	0.04	4.52
Chromium	24	0.21	0.42	0.12	0.01	6.83
Iron	26	1.52	3.07	0.82	0.06	4.14

Nickel	28	0.03	0.06	0.01	0.01	23.76
Sum		49.35	100.00	100.00		

The main results of the analyses can be summarized into the following points:

1) some areas in bpp channels are damaged.

2) elemental mapping confirms segregation into two main compositions: Fe, Ni, Cr for intact areas, C, O, Al for damaged areas.

3) local damage on the bpp channels results into loss of Fe, Ni, Cr and presence of Al, O, C signals.

4) intact areas of the bpp show predominant Fe, Ni, Cr signals, very low C, O signals, and no Al.

5) Al in the bpp comes from current collector plates corrosion.

6) Al powder contains traces of Fe, Cr, Ni as a result of bpp damage, while Al signal is overlapped to O, suggesting Al_2O_3 formation (no direct information about Al bonds and oxidation state can be gained by SEM/EPMA analysis).

7) Na, K, Ca, Mg signals can be detected in traces in bpp damaged channels and. in higher amounts, in Al powder detached from current collector plates, suggesting possible infiltration, between bpp and Al plates, of water from the cooling circuit, which leads to Al oxidation and loss of intermetallic contact between current collector and bpp plate.

6.3.2.2 Investigation on contamination of humidification system

The humidification system (H.S.) of the fuel-cell test machine shows a problem of contamination that takes form of a brown, non-magnetic and insulator slush. In Figure 6.18 the brown substance is shown, that will be labeled as Sample CM1, together with two parts where this brown substance was found.

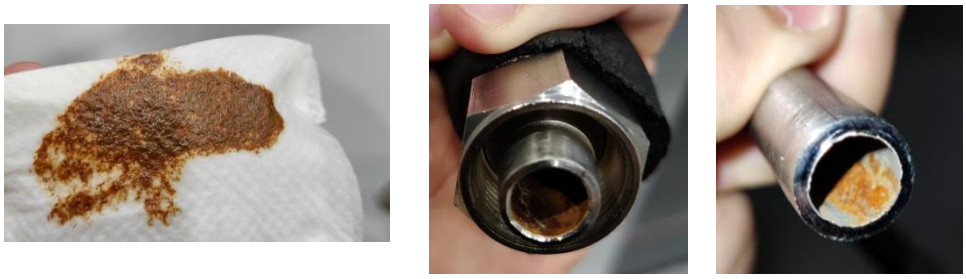

Fig. 6.20 Two different tubes showing the presence of CM1

The non-magnetic nature and the color of this substance suggest the presence of Iron

oxides that can be created by some redox reaction occurring in not specified parts of the humidification system; in addition conductivity test have been performed in situ from samples of brown water showing an increased conductivity in comparison with distilled water (60 μS/cm), the reason for this increased conductivity could be related to the presence of graphitic powder released in the system by the bipolar plate, used to prevent the redox process on the surface of these plates.

In order to investigate the composition of this mush and the possible reason for the contamination, the following tests have been performed including ICP, IR and Elemental Analysis.

Sampling Procedure

For the determination of the nature of this contamination 5 Samples have been collected from different places of the humidification system.

- Sample CM1: Water with a brown suspension found in the pipes before the cleaning procedure of the humidification system
- Sample CM2: A black oily substance from pump
- Sample CM3: A grey mush obtained after cleaning procedure of the humidification system
- Sample W1: Water used for the humidification system
- Sample WB: Pure water used as Blank

Samples CM1/CM2/CM3 were prepared for the analysis as it follows:

For Elemental Analysis:

1. Small amounts of the samples have been taken and evaporated to dryness at 110 °C.

For ICP:

1. Small amounts of the samples have been mineralized by using concentrated HNO_3 and stirring for one day.
2. After that, the samples have been filtered to remove the insolubilized parts.

IR Analysis

The IR analysis allows the identification of functional groups and structural parts of organic compounds such as oils, lubricants or fatty acids present in the samples and for a general identification of the quality of the water used for humidification. It is important to point out that, to increase the conductivity of the bipolar plates, some layers of graphite have been deposited but cannot be identified by IR analysis since it is an IR-inactive compound.

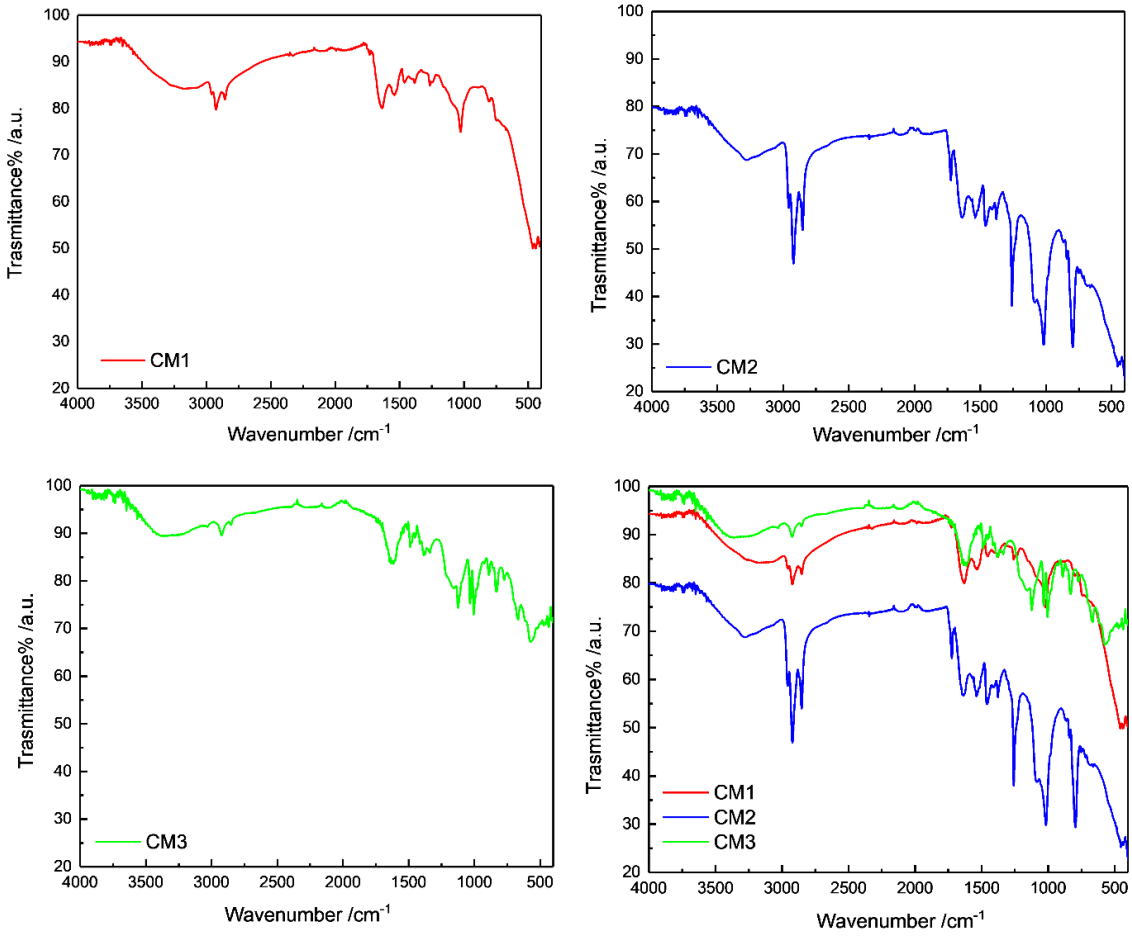

Fig. 6.21 IR comparison for different samples

According to the IR spectrum shown above, it is possible to observe some common peaks at 3400cm^{-1}, 2900-2700cm^{-1}. These peaks respectively can be related to H-O stretching, which can be provided by: (i) trapped water in the samples that did not evaporate during the sample preparation; (ii) hydroxyl of the sulfonate group Nafion; (iii) lubricant pump oil that can present Hydroxyl groups in its structure. The strong absorption peaks in the range of 2900-2700 cm^{-1} are related to the asymmetric and symmetric stretching of aliphatic C-H bond present in the structure of the organic lubricants used for the pump. The fingerprint zone of all the samples (from 1500 cm^{-1} up to 500 cm^{-1}) reveals interesting information toward the nature of the contamination, this zone shows peaks at 1370-1330 cm^{-1} due to Sulfonate stretching present in the Nafion, while 1100-800 cm^{-1} are C=C stretching peak related to the structure of the lubricant.

As it possible to understand the peaks of these samples are similar and comparable; this means that the contamination takes place in all the sampled parts of the humidification system, showing the presence of lubricant oil from the pump and Nafion.

Elemental analysis

According to the fact that ICP cannot identify non-metallic elements, CHNS elemental analysis by GC has been selected for the determination of the concentration of Carbon, Sulfur and eventually Nitrogen in the samples CM1, CM2 and CM3, providing useful information toward the nature of these contaminations. The results are shown in the following tables.

Table 6.7: Results of the E.A. performed on CM1 and the relative total % weight

Element Name	% of weight	Retention Time
Nitrogen	2.2311	48
Carbon	27.5175	74
Hydrogen	4.4194	210
Sulfur	0.1117	459
Total weight	34.2797	

Table 6.8: Results of the E.A. performed on CM2 and the relative total % weight

Element Name	% of weight	Retention Time
Nitrogen	1.5262	48
Carbon	54.4953	74
Hydrogen	8.1149	210
Total weight	64.1363	

Table 6.9: Results of the E.A. performed on CM3 and the relative total % weight

Element Name	% of weight	Retention Time
Nitrogen	2.3083	48
Carbon	55.6693	73
Hydrogen	7.1196	210
Sulfur	7.8526	459
Total weight	72.9498	

These results show the overall weight percentage of C, H, N, S which are present. According to the previous section, these results can be related to the presence of different possible compounds:

- Graphite: from the increased conductivity of the water and the high content of Carbon in elemental analysis.

- Nafion: for the presence of C, H, S in elemental analysis and of the IR peaks described in the previous section.
- Commercial Pump oil: according to the High content of C, H and the IR peaks described in the previous section.

From these data it is also possible to calculate the weight percentage of other elements (metals + O + F) in the samples and the results are shown in Table 6.10:

Table 6.10: Total concentration of metals + O + F

Sample	Metals + O + F
CM1	100-34.2797= 65.7203%
CM2	100-64.1363= 35.8637%
CM3	100-72.9498= 27.0502%

It should be recalled that sample CM1 represents the H.S. at time 0, which means when the contamination has been discovered, while the sample CM3 represents the H.S. after the cleaning procedure. Although the cleaning procedure helps to decrease the inorganic elements concentration, passing from 65.7203% to 27.0502%, it is possible to observe an increasing percentage of Sulfur from 0.1117% up to 7.8526%, which suggests that the Nafion residual is harder to clean.

Elemental analysis by inductively coupled plasma (ICP)

Elemental analysis by Inductively Coupled Plasma (ICP) technique is regarded as a useful tool for the quantification of metals concentration in samples. To understand the nature and the parts that are more subjected to the contamination, the ICP was performed leading to the results in Table 6.11:

Table 6.11: ICP analysis results in ppb (on mineralized samples)

Sample:	WB (Blank)	W1(HSw.)	CM1	CM2	CM3
Concentration:	ppb	ppb	ppb	ppb	ppb
Al	*0*	*63.4*	*48.19*	*60*	*38.45*
Cr	*0*	*0.6055*	*63.81*	*21.69*	*1.931*
Fe	*0.5162*	*50.7*	*1135*	*494*	*41.26*
Ni	*0.1944*	*567.6*	*15.21*	*69.13*	*25.36*
Pt	*0.02116*	*0.08607*	*0.04872*	*0.1176*	*3.834*

According to the ICP result showed above, the H.S. suffers of a major contamination of the following metals: Al, Cr, Fe, Ni, and Pt. Among these metals Al, Cr, Fe, Ni can be found in the

Fuel Cell stack under testing, Pt can be produced by the MEA itself during work caused by MEA cracking and prolonged use. It is important to point out that also the water used for the blank was provided by LOCCIONI

From the data of Table 6.11, by considering the dilutions of samples mineralized before ICP analysis, it is possible to calculate the concentration (mg/g) of the metal in the samples CM1/CM2/CM3 (Table 12):

Table 6.12: Concentration of the metals in the samples

Metals	CM1 (mg/g)	CM2 (mg/g)	CM3 (mg/g)
Al	1.6063	2.000	1.2816
Cr	2.1272	0.723	0.0643
Fe	37.800	16.460	1.375
Ni	0.5072	2.304	0.845
Pt	0.001624	0.00392	0.1278
Total metal content	42.042	21.490	3.694

After subtraction of the overall metal content from the data reported in Table 6.12, it is possible now to reveal the overall Fluorine + Oxygen concentration in the three samples, due to the different sources such as: (i) Nafion (F, O), (ii) Metal Oxides (O) (iii) lubricants structure (O) and (iv) graphite (O) (Table 7).

Table 6.13: Total O + F contents

Sample	Total O + F content
CM1	42.042mg/g, which correspond to 4,2 wt%
	65,7203 wt% - 4,2 wt% = 61.5203 wt%
CM2	21.490mg/g, which correspond to 2,15 wt%
	35,8637 wt% - 2.15 wt% =33,7137 wt%
CM3	3.6937 mg/g, which correspond to 0,37 wt%
	27,0502 wt% - 0,37 wt% = 26,6802 wt%

The Fuel Cells Testing Machine shows evidence of a contamination.

These contaminations are of multiple natures:

- Organic Contamination: from IR and E.A. it is possible to observe the presence the C-H vibration and Carbonyl vibration uniquely lead back to the lubricant oil of the pump while the high % of Sulfur plus the sulfonate stretching peaks is uniquely regarded to the presence of Nafion.

- Inorganic Contamination: From the ICP analysis it has been shown the presence in some cases at high concentration of the following metals: Al, Cr, Fe, Ni, and Pt. The reasons of the presence of Al, Cr, Fe, Ni are regarded to the redox reaction occurred between the bipolar plate and the Fuel Cells Stack. The presence of Pt is probably due to the high current applied during Constant Current analysis mode, which was found to decrease the performance of the MEA causing the loss of Pt by aggregation of nanoparticles.

The cleaning procedure performed on the H.S. seems to have a good effect on the removal of the metals while the organic contaminant seems to be unaffected.

As it can be understood these contaminants can lead to serious damage of the H.S. so counteractions have to be considered:

- Filtering the water with an ionic trap can represent a good solution for the removal of the metal ions.
- Filtering the water with active carbon can represent a good solution for the removal of organic contaminants.
- Implementation of automated cleaning cycles of the H.S. and the filters.

Resolving these problems can also lead to an improved performance for the fuel cells and improve its stability toward long cycling measurements.

6.4 Lab-Scale Fuel Cell station Development

As part of this project, another key objective was the development of a lab-scale test bench specifically designed for 5 cm² Fuel Cells. A miniaturized test bench was successfully developed, enabling precise electrochemical testing of MEAs. This compact system provides valuable insights into the performance and quality of MEAs at a smaller scale, facilitating rapid and efficient testing while supporting the broader objectives of the project.

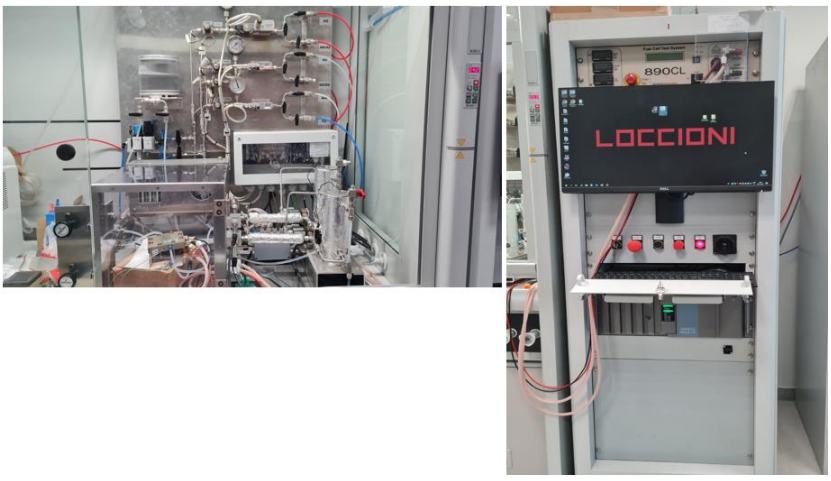

Fig. 6.22 Lab scale test bench hardwares

The synoptic highlights that the lab-scale test bench is simpler compared to the Audi test bench, as it does not include several advanced components such as mass spectroscopy systems, cooling systems, gas recirculation mechanisms, and waste-water management systems. This streamlined design focuses on essential functionalities, making it an efficient and cost-effective solution for smaller-scale MEA electrochemical testing while omitting the complexities required for industrial-scale setups.

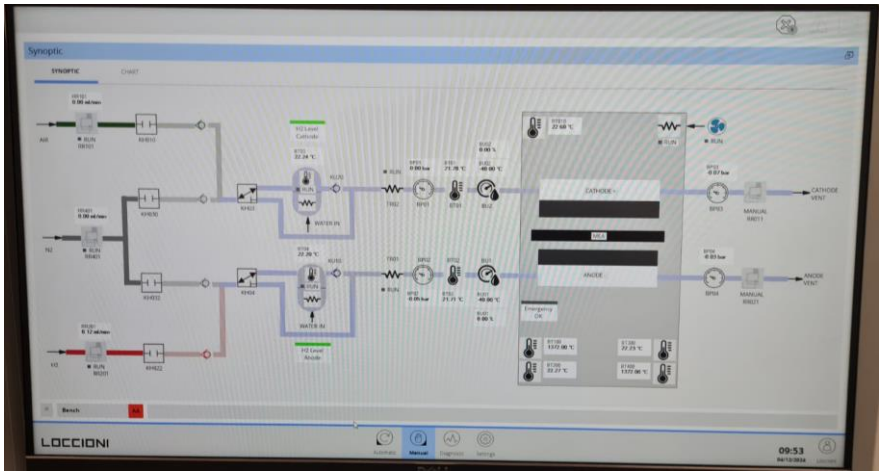

Fig. 6.23 Synoptic of the lab scale test bench

6.5 Conclusions

The first phase of the project with AUDI has been successfully completed, culminating in the installation of the final test bench at its designated location. Years of development and refinement have led to the creation of a highly precise and reproducible test bench, specifically designed for the quality control and performance evaluation of Membrane Electrode Assemblies (MEA) and Fuel Cell (FC) stacks. Continuous modifications and enhancements throughout the development process have significantly contributed to the superior performance of the final configuration.

References

1. Regulation (EU) No 1303/2013, Regulation (EU) No 1304/2013, and https://www.ponricerca.gov.it. Last Visit 19/01/2025

2 Loccioni. (n.d.). *Company website*. Retrieved January 19, 2025, from https://www.loccioni.com.

3. Arcos, J. M. M. & Santos, D. M. F. The Hydrogen Color Spectrum: Techno-Economic Analysis of the Available Technologies for Hydrogen Production. *Gases* 3, 25–46 (2023).

Chapter 7

General Conclusions

In conclusion, this work has focused on the development of green and sustainable materials for advancing the energy transition.

After presenting the history, development, and future perspectives of electrochemical energy storage and production devices, with a particular focus on LIBs, NIBs, supercapacitors, and fuel cells in **Chapter 1**, this thesis also introduces the experimental techniques employed for structural characterization and electrochemical investigations in the **Chapter 2**.

Chapter 3 proposed a Mg- and Zr-modified LNMO cathode material synthesized using a cost-effective and scalable sol-gel method with inexpensive precursors. Detailed structural analyses revealed the substitution of the synthesis-derived noxious LiNiO phase with an inactive $LiMnO_3$ phase after the first cycle. Morphological investigations indicated a transformation from micrometric particles to agglomerated nanometric particles. TEM and XPS analyses identified the dopants' positions and chemical environments, with Mg and partial Zr acting as internal structural dopants, while residual Zr formed ZrO_2 clusters dispersed throughout the material. Electrochemical tests demonstrated that b-LNMO exhibited capacity degradation over 150 cycles at both room temperature and 50°C. This degradation is a consequence of Mn dissolution during cycling, as well as the presence of multi-cubic phase transitions observed in SPEIS analysis during each charge and discharge cycle. In contrast, m-LNMO displayed significantly improved capacity retention, achieving 60.7% over 1000 cycles at 1C and room temperature, and 72.8% over 1000 cycles at 2C and 50°C. Structural rearrangement studies using SPEIS revealed improved charge transfer efficiency and a more stable CEI. Additionally, the material exhibited suppression of mid-voltage multiple cubic phase transitions and reduced rock salt phase formation at the end of the charging process.

Chapter 4 aligned with circular economy principles by valorising aluminium waste from fly ash to synthesize a green sacrificial MOF for producing disordered carbon nanospheres. Morphological and purity analyses using XRD, Raman, SEM, and BET confirmed the suitability of the disordered carbon for supercapacitor applications. Electrochemical tests demonstrated ideal EDLC behavior with no faradaic peaks, achieving exceptional capacity retention of 91.7% over 36,000 cycles and a coulombic efficiency of 99.7%. A symmetric supercapacitor configuration was further explored, showing high-capacity retention of 92.24% over 5000 cycles and good electrochemical stability. Additionally, the material's performance as an anode in NIBs highlighted

promising rate capabilities and sodium storage properties via absorption-insertion mechanisms.

Chapter 5 investigated the systematic doping effects of Mg and Ni on PGM-free materials, specifically Fe_2O_3@rGO as a potential electrocatalyst for ORR. Structural and compositional changes induced by doping were analyzed using XRD, Raman, SEM, TGA, and XPS, revealing significant lattice parameter shrinkage with 6% Mg and Ni. These materials demonstrated notable peroxide scavenging properties compared to pure KJB during standalone catalyst tests. Based on these findings, composite configurations with FePc600 (80:20 and 20:80 catalyst-to-FePc600 ratios) were tested. The 20:80 Ni6%-Fe2O3@rGO composite showed superior performance, achieving a current density of 5.56 mA/cm² and a peroxide production of 2.81%, outperforming pristine FePc600.

Sustainability and green principles are at the heart of innovation in modern science and engineering. By rethinking traditional processes and leveraging circular economy principles, we can create materials that align with environmental priorities without compromising performance. For instance, advances in cathode materials, such as Mg- and Zr-modified LNMO or Fe_2O_3 based catalysts, highlight how scalable and cost-effective methods can replace harmful phases with more stable, efficient alternatives. Similarly, the valorisation of aluminium waste into functional materials for supercapacitors exemplifies how waste can be transformed into high-performing energy solutions. These breakthroughs demonstrate that sustainable innovation is not only possible but essential for achieving long-term energy efficiency and ecological balance.

Chapter 6 marks a pivotal transition from a combustion engine-based transportation paradigm to a more sustainable future, integrating principles of circular economy and sustainability previously outlined. The development of the MEA and FCs Test Bench has been characterized by numerous challenges and setbacks, which have been systematically addressed and resolved over years of dedicated effort.

This transition reflects a collective commitment, from academic research to industrial applications, to tackle climate change through innovation and collaboration. However, achieving a successful and seamless energy transition requires more than technological advancements. It demands robust political frameworks and a capable, forward-thinking political class to navigate and drive these transformative changes effectively.

Each chapter of this thesis focused on the development of sustainable, cost-effective, and scalable synthesis methods for various materials intended for widespread electrochemical storage and energy production devices. Each system offers a distinct balance between energy density and power density:

- Battery systems provide a well-balanced approach between voltage and current, ensuring a trade-off between power density and energy density.
- Supercapacitor systems offer exceptionally high-power density but are limited by low energy density.
- Fuel cell systems exhibit high energy density but generally operate with lower power density.

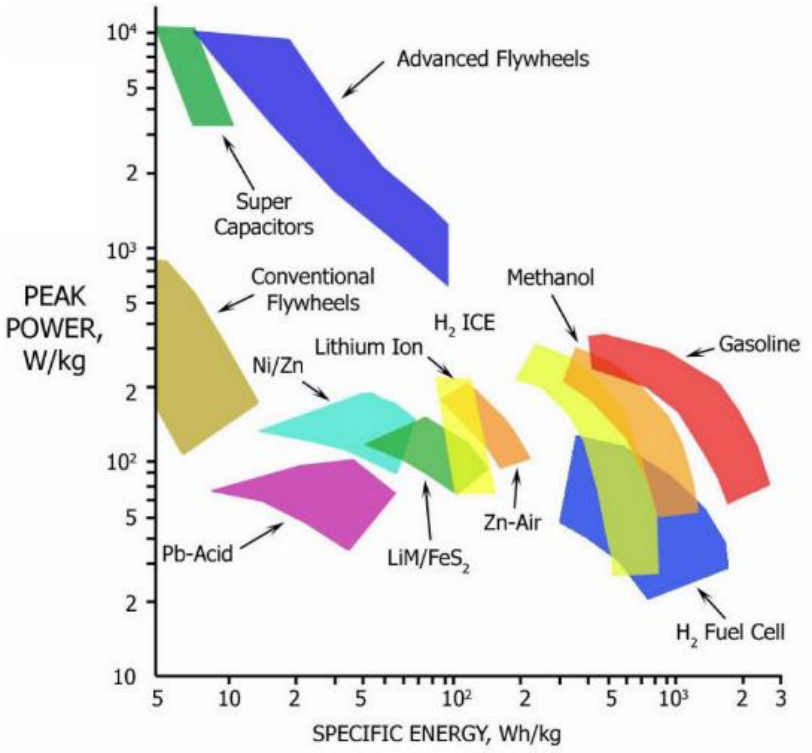

Fig 7.1 Ragone plot of different energy storage and production systems

The drive for developing new and more efficient materials for energy production and storage is now centred on the search for sustainable materials and modifications that can extend lifecycle performance, enable material reuse, and/or allow material preparation with lower energy consumption, such as at lower temperatures or under less demanding conditions, aligning with the principles of the circular economy.

List of Publications

Balducci Leonardo, Hamideh Darjazi, Elena Gonzalo, Rosalía Cid, Francisco Bonilla, and Francesco Nobili. 2023. "Evaluation of Electronic-Ionic Transport Properties of a Mg/Zr-Modified LiNi0.5Mn1.5O4 Cathode for Li-Ion Batteries." *ACS Applied Materials and Interfaces* 15(48):55620–32. doi: 10.1021/acsami.3c10480.

H. Darjazi, L. Bottoni, H. R. Moazami, S. J. Rezvani, L. Balducci, L. Sbrascini, A. Staffolani, A. Tombesi, and F. Nobili. 2023. "From Waste to Resources: Transforming Olive Leaves to Hard Carbon as Sustainable and Versatile Electrode Material for Li/Na-Ion Batteries and Supercapacitors." *Materials Today Sustainability* 21. doi: 10.1016/j.mtsust.2022.100313.

Darjazi Hamideh, Marisa Falco, Francesca Colò, Leonardo Balducci, Giulia Piana, Federico Bella, Giuseppina Meligrana, Francesco Nobili, Giuseppe A. Elia, and Claudio Gerbaldi. 2024. "Electrolytes for Sodium Ion Batteries: The Current Transition from Liquid to Solid and Hybrid Systems." *Advanced Materials* 36(35).

List of Submitted Publications

Leonardo Balducci, Mohsin Muhyuddin, Hamideh Darjazi, Giuseppina Meligrana, Carlo Santoro, Francesco Nobili "Fe_2O_3@rGO doped Mg and Ni as enhanced peroxide scavenger cocatalysts in oxygen reduction reaction"

La borsa di dottorato cofinanziata con risorse del
Programma Operativo Nazionale Ricerca e Innovazione 2014-2020 (CCI 2014IT16M2OP005),
risorse Fondo Sociale Europeo REACT-EU, Azione I.1 "Dottorati Innovativi con caratterizzazione industriale", Azione IV.4 "Dottorati e contratti di ricerca su tematiche dell'innovazione" e Azione IV.5 "Dottorati su tematiche Green"

UNIONE EUROPEA
Fondo Sociale Europeo